universität wien

DISSERTATION | DOCTORAL THESIS

Titel | Title

Low dissipation magnetic levitation of superconducting microspheres

verfasst von | submitted by

Joachim Hofer BSc BSc MSc

angestrebter akademischer Grad | in partial fulfilment of the requirements for the degree of

Doktor der Naturwissenschaften (Dr.rer.nat.)

Wien | Vienna, 2025

Studienkennzahl lt. Studienblatt | Degree programme code as it appears on the student record sheet:	UA 796 605 411
Dissertationsgebiet lt. Studienblatt | Field of study as it appears on the student record sheet:	Physik
Betreut von | Supervisor:	Univ.-Prof. Dr. Markus Aspelmeyer

Experiment is the sole judge of scientific truth. But what is the source of knowledge? Where do the laws that are to be tested come from? Experiment, itself, helps to produce these laws, in the sense that it gives us hints. But also needed is imagination to create from these hints the great generalizations to guess at the wonderful, simple, but very strange patterns beneath them all, and then to experiment to check again whether we have made the right guess. This imagining process is so difficult that there is a division of labor in physics: there are theoretical physicists who imagine, deduce, and guess at new laws, but do not experiment; and then there are experimental physicists who experiment, imagine, deduce, and guess.

Richard P. Feynman

Abstract

Developing a self-consistent theory incorporating both quantum mechanics and gravity has been a major objective in physics for almost a century. The gravitational force is weak compared to the other fundamental forces and can only be detected for macroscopic source masses. Probing the intersection of quantum physics and gravity experimentally with a table-top experiment thus requires the preparation of motional degrees of freedom of large masses in a quantum state. The current state-of-the-art allows us to measure the gravitational field of milligram masses, and the center-of-mass motion of optically levitated femtogram masses has been prepared in a quantum state.

The levitation of a superconducting particle inside a quasi-static magnetic field offers the tantalizing possibility of creating a levitated system in a harmonic potential with near-zero dissipation and possible particle sizes ranging from the sub-micrometer-scale up to the millimeter scale, such that the gravitational field of the oscillating particle is experimentally accessible. The motion of the levitated particle can be controlled by modulating the magnetic field, allowing for the possibility of preparing such a system in a quantum state.

In this thesis I have created a framework for the levitation of superconducting particles in magnetic fields at ultra-low temperatures. I have developed both numerical and analytical tools to evaluate and predict the behavior of a superconducting sphere in an applied magnetic field. Based on the results, I have designed and assembled a magnetic trap for superconductors inside a dilution refrigerator at 15 mK and used it to levitate a superconducting sphere with a diameter of 100 µm. The trapping frequencies can be adjusted between approximately 20 Hz and 240 Hz. The motion of the sphere is recorded with a superconducting quantum interference device and exhibits quality factors of up to 2.6×10^7. Real-time processing of the monitored signal and applying an appropriate feedback current through a coil located close to the particle enables three-dimensional feedback control of the center-of-mass motion. I have designed and implemented a novel cryogenic vibration isolation system to isolate the particle from external vibrations resulting in the suppression of external vibrations by seven orders of magnitude at 200 Hz. I also incorporated magnetic shielding to protect the particle from magnetic field fluctuations.

A thorough analysis of the results shows, that, with some improvements, this system has the potential to prepare quantum states of the center-of-mass motion of massive solid state objects in the micrometer regime. Such a system will be ideally suited as a quantum source of gravity for future table-top experiments aiming to probe quantum effects of gravity.

Zusammenfassung

Die Entwicklung einer einheitlichen Theorie für Quantenmechanik und Gravitation ist derzeitig eines der größten Ziele der Physik. Ein hohes Hindernis, dass es dabei zu überwinden gibt, ist der Mangel an Experimenten - um experimentelle Daten in diesem Bereich zu gewinnen, ist es nötig, die Bewegungsfreiheitsgrade eines massiven Teilchens in einen Quantenzustand zu versetzen. Der aktuelle Stand der Technik ermöglicht es, das Gravitationsfeld von Milligramm-Massen zu messen und optisch levitierte Teilchen mit Femtogramm-Massen in einen Quantenzustand zu versetzen.

Die magnetische Levitation von supraleitenden Teilchen in einem quasistatischen Feld kann nahezu dämpfungsfrei sein, und zwar selbst für massive Teilchen, deren Gravitationsfeld experimentell nachweisbar ist. Die Bewegung dieser Teilchen kann über das Magnetfeld beeinflusst und prinzipiell in einen Quantenzustand versetzt werden.

In dieser Arbeit habe ich das Fundament für Experimente mit levitierenden Supraleitern gelegt. Ich habe das Verhalten von supraleitenden Teilchen in einem Magnetfeld sowohl analytisch als auch numerisch berechnet und, basierend auf den Ergebnissen, eine magnetische Falle für Supraleiter entworfen. Ich habe die Falle in einen Entmischkryostaten bei 15 mK eingebaut und damit eine supraleitende Kugel mit einem Durchmesser von 100 µm levitiert. Ich konnte die Bewegung der Kugel mit einem supraleitenden Quanteninterferenzgerät auslesen und einen Gütefaktor von 2.6×10^7 nachweisen. Durch Echtzeitverarbeitung des gemessenen Signals und einer darauf basierenden Modifikation des Magnetfelds konnte ich die Bewegung des Teilchens in allen drei Dimensionen kontrollieren. Weiters habe ich noch ein neuartiges kryogenens Vibrationisolationssystem entworfen und eingebaut, sowie Magnetschilder zur Abschirmung vor externen Magnetfeldschwankungen.

Eine detaillierte Analyse der Ergebnisse zeigt, dass es mit weiteren Verbesserungen möglich ist, das levitierte Teilchen in einen Quantenzustand zu versetzen. Dadurch hat dieses System das Potential, Quantenphysik mit massiven, makroskopischen Teilchen zu betreiben und Gravitationseffekte in diesem Bereich zu testen.

Contents

1 Introduction **1**
1.1 Structure of this thesis . . . 2

2 Relevant theory **3**
2.1 The harmonic oscillator . . . 3
2.2 Measurements . . . 4
2.3 Sensing . . . 6
2.4 Coupled oscillators . . . 7
2.5 Vibrations . . . 8
2.6 Vibration isolation . . . 11

3 Magnetic levitation **14**
3.1 Superconductivity and the London theory . . . 15
3.2 Levitation of superconductors . . . 17
3.3 Trap configurations . . . 19
3.3.1 Anti-Helmholtz trap configuration . . . 19
3.3.2 Multi-potential trap configuration . . . 20
3.4 Coupling to an external circuit . . . 22
3.4.1 Coupling to a SQUID . . . 25
3.5 Dissipation due to induced currents . . . 25
3.5.1 Dissipation in a conducting ring . . . 25
3.5.2 Finite element method . . . 26
3.5.3 Limitations to the quality factor . . . 28

4 Analytic solutions to the Maxwell–London equations and levitation force for a superconducting sphere in a quadrupole field **30**
4.1 Introduction . . . 32
4.2 Magnetic field for $\lambda = 0$ . . . 33
4.3 Magnetic field for finite λ . . . 34
4.4 Levitation force and maximum field . . . 37
4.5 Summary and discussion . . . 38
4.6 References . . . 40
4.7 Appendix . . . 41

5 High-Q Magnetic Levitation and Control of Superconducting Microspheres at Millikelvin Temperatures **43**
5.1 Introduction . . . 45
5.2 Trapping . . . 46
5.3 Readout . . . 47
5.4 Mechanical frequencies . . . 48
5.5 Quality factor . . . 48
5.6 Sensing . . . 49
5.7 Cryogenic vibration isolation . . . 50
5.8 Prospects for ground state cooling . . . 50
5.9 Discussion and outlook . . . 52
5.10 References . . . 52
5.11 Derivation of the magnetic trap's properties . . . 58
5.11.1 Trapping field . . . 58
5.11.2 Mechanical frequencies . . . 58

5.11.3 Coupling strength . . . 60
5.11.4 Trap displacement due to gravity . . . 60
5.12 Current fluctuations . . . 60
5.13 Sensing . . . 62
5.14 Feedback . . . 64
5.15 Characterization of the vibration isolation system . . . 64
5.16 Quality factor . . . 67
5.17 Calibration . . . 67
5.18 Optimizations and ground state cooling . . . 68
5.18.1 Coupling strength . . . 68
5.18.2 The standard quantum limit . . . 70
5.18.3 Feedback cooling . . . 70
5.18.4 Heating . . . 71
5.19 References . . . 71

6 A numerical approach to levitated superconductors and its application to a superconducting cylinder in a quadrupole field 74
6.1 Introduction . . . 76
6.2 Model . . . 76
6.3 Equilibrium positions . . . 79
6.4 Trap frequencies . . . 81
6.5 Flux and coupling . . . 85
6.6 Maximum field . . . 85
6.7 Summary and discussion . . . 88
6.8 Acknowledgments . . . 91
6.9 References . . . 91
6.10 Convergence and comparison to the analytical solution . . . 92
6.11 Dependence of the solutions on the edge radius or penetration depth . . . 92

7 Measuring the gravitational field of small masses using levitated superconductors 95
7.1 Motivation . . . 95
7.2 A new trap . . . 95
7.3 Gravitational coupling . . . 97
7.4 Vibrational coupling . . . 100

8 Conclusion and Outlook 103

Bibliography 105

1 Introduction

Although several theories describing the interface between quantum mechanics and general relativity have been proposed, the predictions made by these theories cannot yet be verified - or falsified - by current state-of-the-art experiments [CST19]. The main hindrance to developing experiments aiming to probe the intersection of quantum mechanics and gravity is the weakness of the gravitational interaction compared to other forces and, therefore, only gravitational fields sourced by relatively large masses (milligram-scale objects at the time of writing [WHPA21]) can be measured. On the other hand, preparing the motional degrees of freedom of any object in a quantum state becomes more challenging as the size of the object increases. Currently optically levitated dielectric particles are the heaviest objects whose center-of-mass (c.o.m) motion has been prepared in a quantum state [MRB+21, RMZ+24], however, the masses of these particles are still only on the order of femtograms. The size of these particles is limited by the optical wavelength and cannot be increased much further [MGFM17].

Magnetic levitation has been proposed as an alternative to optical levitation in order to probe quantum mechanics with increasingly massive objects [RICN+12, PPCS+18]. In particular, levitation of a zero-field-cooled superconductor in a static magnetic field has the potential to avoid all but the most fundamental sources of dissipation and decoherence, such that the preparation of such an object in a quantum state of motion seems feasible. Regarding size, with such a trap architecture it is possible to levitate particles with masses ranging from femtograms to tens of milligrams [HA19], overcoming the main limitation of optical traps and potentially enabling us to probe the boundary between the microscopic and macroscopic domains of physics, between quantum mechanics and gravity.

Another feature of magnetic trapping is that the potential experienced by the levitated superconductor can easily be altered by additional currents. This is used to manipulate the particle motion by supplying an appropriate feedback current [HGH+23]. Furthermore, it also enables fast switching between harmonic, nonlinear and repulsive potentials [PPCS+18], or free evolution along one (or more) degree(s) of freedom. The ability to dynamically alter the potential is critical to prepare and manipulate non-trivial quantum states such as, for example, spatial quantum superpositions with a wide separation [NCRI+24, RLRCC+24].

The cryogenic environment necessary for such an experiment is both a boon and a curse. On the one hand, a complex setup is inherently much more difficult to develop and test at cryogenic temperatures, as each test requires a "cooling-down" and "warming-up" phase, with a combined turnaround time of more than a day in the dilution refrigerator that was used for most of the experimental work. On the other hand, the cryogenic temperatures offer many relevant benefits. Most fundamental sources of dissipation and decoherence, such as gas damping and black body radiation, can be kept extremely small [TH77, RICN+12]. Cryogenic temperatures allow access to the toolbox of superconducting circuits, which includes superconducting quantum interference devices (SQUIDs), microwave cavities, as well as superconducting qubits. SQUIDs are amongst the most sensitive flux sensors and I use them to measure the motion of the levitated particle and generate a feedback signal to control the particle motion. Microwave cavities could offer an alternative for quantum-limited position readout and feedback cooling of the levitated particle [SCH+24], while qubits and other non-linear superconducting circuits could be used to generate non-trivial quantum states [RICN+12], either as an alternative or in addition to the manipulation of the magnetic potential.

Apart from their potential for probing new parameter regimes of macroscopic quantum physics, magnetically levitated oscillators also exhibit extremely high force and acceleration sensitivities [HGH+23], that are otherwise only found for much smaller (force) or larger

(acceleration) particles [Goo99, HVT+17]. This opens up new possible fields of application, such as table-top dark matter sensors [HKL24].

In this thesis I present a setup for the levitation of superconducting particles in a magnetostatic trap as well as the theoretical framework necessary for its description. The levitated particles exhibit quality factors of up to 2.6×10^7, which, to the best of my knowledge, is the highest quality factor measured for a magnetically levitated particle at the present date. A novel cryogenic vibration isolation system and magnetic shielding isolate the levitated sphere extremely well from the environment. As a consequence, the equilibrium temperature corresponding to the particle's c.o.m. motion is below our displacement detection sensitivity ($< 2\,\mathrm{K}$). The motion of the particle is read-out by magnetomechanical coupling to a superconducting quantum interference device (SQUID). Real-time processing of the SQUID signal and applying an appropriate feedback current to a separate coil enables three-dimensional feedback control of the particle motion. Based on the obtained results I quantify the improvements that are necessary to prepare the levitated particle in its quantum ground state of motion.

This work establishes a comprehensive proof-of-concept for using levitated superconductors as oscillators in a new parameter regime of low dissipation and high mass, with the ultimate aim of testing physics at the (fluent) boundary between quantum mechanics and gravity.

1.1 Structure of this thesis

In chapter 2 and 3 I will introduce the theory that is necessary to understand the later chapters. The former will focus on the description of harmonically oscillating systems, while the latter will deal with magnetic levitation of superconductors.

In each of the chapters 4-6 I present one of the publications [HA19, HGH+23, Hof24] written in the course of the thesis, with a brief preamble providing the necessary context. In the publication presented in chapter 4 [HA19] I develop the theoretical framework to describe the magnetic levitation of a superconducting sphere in a quadrupole field, while the one presented in chapter 5 [HGH+23] provides a detailed description of the experiment and its results. The publication in chapter 6 [Hof24] describes numerical techniques to evaluate the behavior of arbitrarily shaped superconductors in arbitrary fields and presents some results for a superconducting cylinder in a quadrupole field.

In chapter 7 I propose a setup utilizing one magnetically levitated sphere to measure the gravitational field sourced by a second magnetically levitated sphere and show that such a setup could potentially enable gravitational measurements of microgram source masses.

Finally, in chapter 8 I summarize the results and share my conclusions. I also provide a brief outlook regarding future experiments.

2 Relevant theory

We now start with the relevant theory that is necessary to understand the contents of the thesis. I will assume that any reader has some background in physics and is familiar with common nomenclature and notations. In this first section, I will mainly present a summary of the properties of a harmonic oscillator. Although this is one of the most ubiquitous systems both in nature (at least to a good approximation) and in lecture halls, I find that some subtleties are often overlooked or quickly forgotten. When I started writing this thesis it wasn't my intention to dedicate an entire section to this, but I noticed that so much of the theory needed for the description of the experiment was based on this simple system that it happened almost naturally.

We will begin with the most fundamental equation used to model a harmonic oscillator and then look at some more involved phenomena associated with thermal forces, vibrations, measurements and coupled oscillators.

The theory behind magnetic levitation will be introduced in the next section.

2.1 The harmonic oscillator

A harmonic oscillator describes a system that, when displaced from its equilibrium, experiences a restoring force proportional to the displacement, leading to an oscillatory motion. For our purposes we consider mostly mechanical oscillators, where the displacement refers to the displacement of the c.o.m. of a massive object in space. In any physical system there will be dissipation, i.e. the oscillator will lose energy to its environment. The term environment refers to any physical systems that interact with the oscillator, but are not explicitly included in the model. While there are many coupling mechanisms by which energy transfer can occur, most of them can be modeled by viscous damping with a force that is proportional to the velocity (and pointing in the opposite direction) and the mass of the oscillator. Most commonly the model for a mechanical oscillator with a single degree of freedom (e.g. the position x) is thus expressed as

$$m\ddot{x} = -kx - m\gamma\dot{x} + F. \tag{1}$$

Here k is the spring constant, m is the mass and γ the damping coefficient, while F includes all other forces that might be acting on the oscillator. For a small damping coefficient $\left(\gamma \ll \sqrt{\frac{k}{m}}\right)$ this leads to an oscillatory motion with a frequency of approximately

$$f_0 = \frac{1}{2\pi}\sqrt{\frac{k}{m}} = \frac{\omega_0}{2\pi}.$$

One example of a force that will always act on the oscillator is the thermal force. The thermal force arises again from coupling to the environment, as this not only provides a dissipation channel, but also a route for energy to be transferred to the oscillator. An easy-to-understand example are gas molecules, where, loosely speaking, the oscillator loses energy by hitting the gas molecules and gains energy from gas molecules hitting the oscillator. This leads to a motion of the particle with a finite mean amplitude, at which the damping and the driving due to the thermal force balance out. We talk about a thermal force because it is assumed that the gas molecules are in thermal equilibrium and their movement is (statistically) determined by their temperature. Note that the environment does not necessarily refer to external physical systems, but could also refer to internal systems such as the (thermally excited) movement of the atoms of the oscillator itself, i.e. its internal vibrational modes.

As the thermal force acts randomly, we can only add it to the model by looking at its statistical, time-averaged effects. We already did this for the damping without explicitly

mentioning it - considering again the example of gas molecules, where the energy is transferred to the gas molecules in small steps each time the oscillator hits a molecule. Only if many molecules hit the oscillator in each mechanical period (and if we are not interested in timescales much shorter than the mechanical period) we can model this energy transfer with a continuous force as in Eq. 1; if there are very few molecules around we would generally have to choose a different model.

A useful tool for working with statistical properties of physical quantities is the power spectral density (PSD). The power spectral density of a signal $f(t)$ is denoted by $S_{ff}(\omega)$ and, loosely speaking, it provides a measure of the power of the signal at a certain frequency. Readers unfamiliar with power spectral densities can find a good introduction in the appendix of [CDG+10].

The thermal force is modeled as white Gaussian noise with zero mean and it follows from the equipartition theorem that the corresponding one-sided power spectral density has a value $S_{th} = 4k_BTm\gamma$ [UO30]. In the frequency domain and including the thermal force explicitly, Eq. 1 becomes

$$S_{xx}(\omega) = |\chi(\omega)|^2 \left(4k_BTm\gamma + S_{FF}(\omega)\right), \tag{2}$$

where

$$\chi(\omega) = \frac{1}{m\left(\omega_0^2 - \omega^2 - i\omega\gamma\right)}$$

is the mechanical susceptibility. Note that from now I will no longer explicitly highlight the frequency-dependence of the PSDs and generally omit the argument of functions for notational convenience (unless the context requires it).

I want to highlight that the statements of this paragraph apply to time-averaged properties of an oscillator in the steady state. Therefore, the measurement time has to be large compared to the relevant timescales - for a high-Q oscillator the relevant timescale is usually $\frac{1}{\gamma}$. In Fig. 1 I plot $x(t)$ for an oscillator driven by thermal noise (values are taken from a numerical simulation of Eq. 1) and the corresponding PSD.

2.2 Measurements

In the last section I introduced some properties of the mechanical oscillator without any consideration to how they could be measured. We will now consider a continuous position measurement of the oscillator. Although such a measurement can be implemented in different ways, we will see that there are some general statements that apply to any measurement of this type.

First, it is well established that, according to quantum mechanics, the c.o.m. position and momentum of a massive object cannot both be determined with arbitrary precision at the same time [Wei15]. A continuous[1] measurement of the position is inherently also a measurement of the velocity and thus the momentum (the mass can be determined in

[1] In the conventional presentation of non-relativistic quantum mechanics the quantum mechanical system undergoes unitary evolution governed by the system's Hamiltonian, and discrete measurements instantly reduce the state to an eigenstate of the measurement operator, i.e. in this framework there are no continuous measurements. The main part of this thesis deals with classical properties of a harmonic oscillator and I only introduce quantum mechanics here in order to show that there are some intrinsic, fundamental limits to any measurements one can make. I do not intend to delve deeper into the theory, note only that a weak, continuous measurement of the position is possible while the unitary quantum mechanical evolution still applies. For more details on the treatment of continuous measurements in quantum mechanics I refer the reader to the literature [CM87, BKT92, CDG+10].

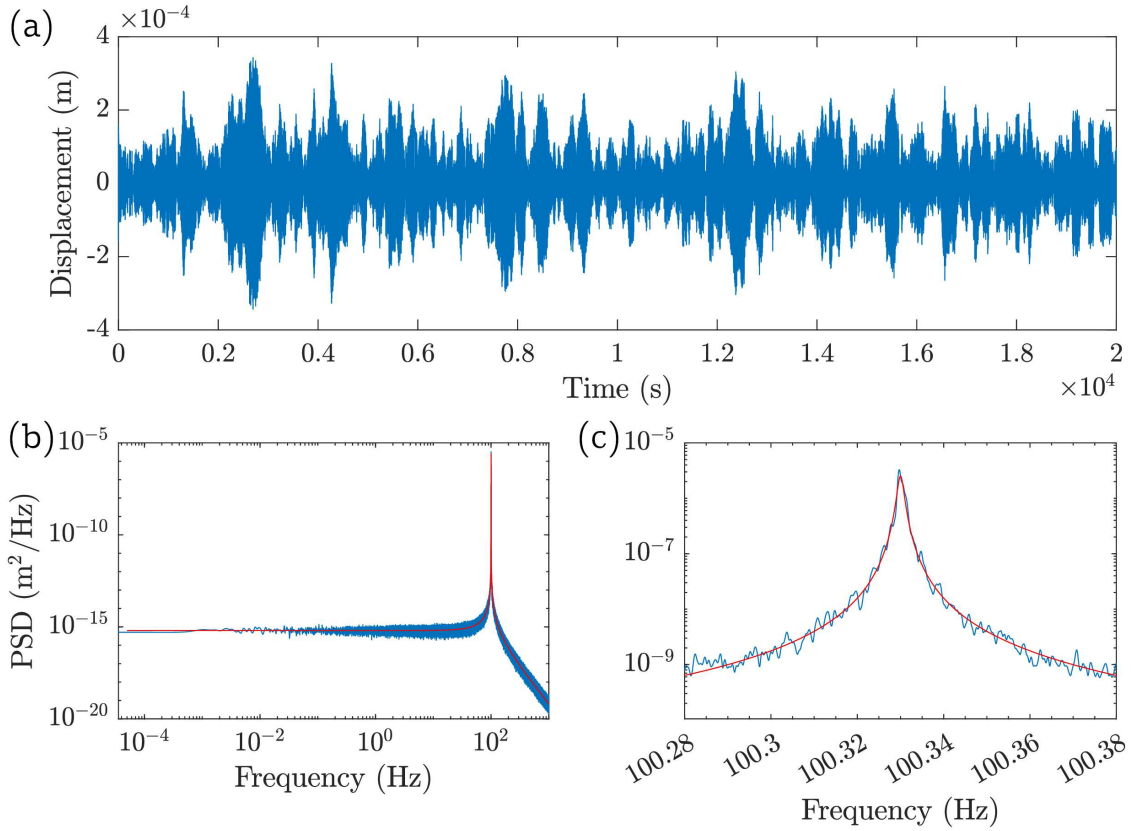


Figure 1: (a)Transient displacement of an oscillator driven by white Gaussian noise. Here $\gamma = 0.01\,\mathrm{s}^{-2}$, note that the amplitude can vary considerably on a timescale $\frac{1}{\gamma}$. (b)Numerical PSD of the transient signal shown in (a). The red solid line is the analytical result (Eq. 2). (c)Same as (b), but zoomed in on the resonance.

a separate measurement). This results in an intrinsic measurement uncertainty (quantum fluctuations) inherent to all continuous position measurements.

Second, apart from quantum fluctuations due to the intrinsic uncertainties of the quantum-mechanical state of the oscillator, measuring also necessitates, by definition, coupling the oscillator to some measurement device. By measurement device we mean a device that produces a macroscopic quantity related to the c.o.m. position (as we consider a position measurement) of the oscillator. In many common measurement devices the position and the macroscopic output quantity are linearly related, we then say the measurement device acts as a linear amplifier. We might allow for the possibility that the measurement is not perfect and introduce a measurement noise with power spectral density S_n. Note that here S_n refers only to the noise that is added by the measurement device and does not include the intrinsic uncertainty that is already present if the oscillator is in a quantum state. Further, as the oscillator is now coupled to the measurement device, we should also consider the possibility of the measurement device exerting a force on the oscillator, a so-called back action force with power spectral density S_{ba}. Assuming that S_n and S_{ba} are uncorrelated, the measured power spectral density corresponding to the position now reads

$$S_{xx}^{meas} = S_{xx} + |\chi|^2 S_{ba} + S_n.$$

Here S_{xx} refers to the PSD we would expect for the oscillator from Eq. 2, taking into account all applicable forces, but without coupling to a measurement device, i.e. it is the undisturbed state of the oscillator that we would like to measure - it could also correspond to the quantum ground state or some other quantum state. So, assuming that S_n and S_{ba} are non-zero, we

see that the measurement process not only is imperfect and obfuscates the state we want to measure with noise (S_n), it even changes the state itself (resulting in a change of its PSD from S_{xx} to $S_{xx} + |\chi|^2 S_{ba}$).

To determine S_n and S_{ba} one generally needs to know the details of the measurement process. Analyzing different measurement schemes (a prototypical example is Heisenberg's microscope [Hei27, BKT92]) typically results in the inequality

$$S_{ba} S_n \geq \hbar^2. \tag{3}$$

This inequality can be proven generally for measurement devices that act as linear amplifiers [Cav82, CDG+10].

From Eq. 3 we can now derive an inequality for the measurement uncertainty

$$S_{xx}^{meas} - S_{xx} = |\chi|^2 S_{ba} + S_n \geq |\chi|^2 S_{ba} + \frac{\hbar^2}{S_{ba}}.$$

The term on right-hand side is minimized when $S_{ba} = \frac{\hbar}{|\chi|}$, resulting in

$$S_{xx}^{meas} - S_{xx} \geq 2\hbar|\chi|,$$

or, in the optimal case $S_{ba} S_n = \hbar^2$,

$$S_{xx}^{meas} - S_{xx} = 2\hbar|\chi|. \tag{4}$$

Equation Eq. 4 is called the standard quantum limit[2] (SQL) [BKT92, CDG+10]. The SQL denotes the minimum amount of noise that is present (on top of the intrinsic uncertainty of the oscillators state) in a continuous position measurement. Note that for the SQL $S_n = |\chi|^2 S_{ba}$, so both the measurement noise and the back-action noise contribute equally to the total noise.

Finally, although we started this section by talking about quantum mechanics, no wave function or operator ever occurred in any of the equations. This is because the quantities of which we measure the PSDs with a device such as a spectrum analyzer are classical (the macroscopic outputs of the measurement device), and the effects of quantum mechanics are only implicit, namely by enforcing the limit on measurement noise and back-action. For a much more in-depth discussion including the derivation of these relations (and containing plenty of wave functions and operators), I highly recommend [BKT92, CDG+10]. As a last comment, Eq. 3 is often seen as $S_{ba} S_n \geq \frac{\hbar^2}{4}$ - the difference is simply a factor two in the definition of the PSD.

2.3 Sensing

A typical use-case for harmonic oscillators is as force or acceleration sensors. In the last section I covered measurements of the position of a harmonic oscillator, now I want to discuss how we can use the harmonic oscillator itself as a probe to measure a force acting on the oscillator. Let us consider again the PSD for the measured position of the harmonic oscillator, taking into account also the thermal force S_{th}, s.t.

$$S_{xx}^{meas} = |\chi|^2 (S_{sig} + S_{th} + S_{ba}) + S_n,$$

where S_{sig} denotes the power spectral density of the force which we want to measure. Note that other forces might be present, (e.g. due to vibrations of the oscillators support, which

[2] To be more precise, Eq. 4 is the standard quantum limit for a weak, continuous position measurement of a harmonic oscillator. Similar limits can be derived for other types of measurements.

we consider in a subsequent section), these can be absorbed in the thermal force term by introducing an effective (and usually frequency dependent) temperature T_{eff}. The following treatment is still valid in this case.

From the position measurement we can estimate the PSD of the total force (including thermal and back action forces) acting on the oscillator as

$$|\chi|^{-2} S_{xx}^{meas} = S_{sig} + S_{th} + S_{ba} + |\chi|^{-2} S_n$$

and the signal to noise ratio is

$$SNR = \sqrt{\frac{S_{sig}}{S_{th} + S_{ba} + |\chi|^{-2} S_n}}.$$

Note that the last term in the denominator is minimized on resonance. If this term as well as the back action are small compared to the thermal force, the SNR becomes approximately $\sqrt{\frac{S_{sig}}{S_{th}}}$ and $SNR = 1$ corresponds to

$$\sqrt{S_{sig}} = \sqrt{4 k_B T m \gamma},$$

which is often called the thermal force sensitivity.

More generally, we know from the last section (Eq. 4) that the combined effects of back-action and measurement noise are minimized when

$$|\chi|^2 S_{ba} + S_n = 2\hbar|\chi|,$$

in which case

$$SNR = \sqrt{\frac{S_{sig}}{S_{th} + 2\hbar|\chi|^{-1}}}.$$

Assuming now that the thermal noise is negligible compared to back-action and measurement noise we find that the weakest force that can be detected with $SNR = 1$ is

$$\sqrt{S_{sig}} = \sqrt{\frac{2\hbar}{|\chi|}}.$$

Analogous to the standard quantum limit for position sensing this is called the standard quantum limit for force sensing [BKT92].

As a final remark note that in principle arbitrary small forces with $SNR \ll 1$ can be detected, if all the assumptions that we've made about the stochastic behavior of the forces involved are correct and perfectly stable over long (measurement) durations - usually this is not the case. Although this is an arbitrary choice, the force sensitivity for $SNR = 1$ is conventionally used as a reference to compare different methods for force sensing [Con19].

2.4 Coupled oscillators

For two (or more) oscillators, if the force on one oscillator depends on the state of the other(s), we say that the oscillators are coupled. As an example we consider the system described by the equations

$$\begin{aligned} m_1 \ddot{x}_1 &= -k_1 x_1 - m_1 \gamma_1 \dot{x}_1 + F_1 + \sum_{i=2}^{N} k_{1,i} x_i \\ &\vdots \\ m_N \ddot{x}_N &= -k_N x_N - m_N \gamma_N \dot{x}_N + F_N + \sum_{i=1}^{N-1} k_{N,i} x_i. \end{aligned} \tag{5}$$

The force acting on each oscillator now contains additive terms depending linearly on the position of the other oscillators. The factor $k_{i,j}$ determines the magnitude of the force on the i-th oscillator for a given displacement of the j-th oscillator and thus the strength of the coupling. Analogous to the notation introduced for a single oscillator, F_i contains all other forces that might act on the i-th oscillator (such as thermal or back-action forces). I have again used the notation typically used for mechanical oscillators (m for the mass, x for the position, and so on), but the same equations might describe the coupling between electromagnetic oscillators such as LC circuits, or between mechanical and electromagnetic oscillators.

This system can be solved in analogy to a single harmonic oscillator by assuming that there are some (in general complex) values $\hat{x}_i$, λ such that all x_i are of the form $x_i(t) = \hat{x}_i e^{\lambda t}$. If we assume for now that no external forces are acting on the oscillators (all F_i are zero), using the system of equations 5 then leads to the eigenvalue equation

$$\begin{pmatrix} \lambda^2 + \gamma_1\lambda + \frac{k_1}{m_1} & \cdots & -\frac{k_{1,N}}{m_1} \\ \vdots & \ddots & \vdots \\ -\frac{k_{N,1}}{m_N} & \cdots & \lambda^2 + \gamma_N\lambda + \frac{k_N}{m_N} \end{pmatrix} \hat{\mathbf{x}} = 0, \tag{6}$$

with $\hat{\mathbf{x}} = (\hat{x}_1, ..., \hat{x}_N)^T$. The solutions for λ and $\hat{\mathbf{x}}$ determine the normal modes of the system. With respect to the normal modes the system behaves like N independent harmonic oscillators (as the matrix in Eq. 6 is diagonal if the eigenvectors $\hat{\mathbf{x}}$ are used as a basis). Note that the preceding statements assume that N independent (orthogonal) eigenvectors exist - this is always the case for a matrix that results from the system of equations 5, because it could be expressed as a symmetric matrix[3]. The angular resonance frequencies of the normal modes are given by the imaginary part of the eigenvalues λ, while the damping is given by the real part. We can directly apply the results for a single harmonic oscillator, introduced in the preceding sections, to each of the normal modes (we only have to be careful to work in the basis of eigenvectors).

I have plotted some interesting cases (avoided crossing, induced transparency) resulting from the coupling between two oscillators in Fig. 2.

2.5 Vibrations

We will now consider the effects of vibrations on the setup. To do this it is important to differentiate between forces acting on the oscillator and forces acting on the support of the oscillator. By support we mean the structure to which the oscillator is attached and relative to which the rest position of the oscillator is defined. In the case of a mass on a physical, elastic spring this would refer to the surface to which the spring is physically attached, in the case of an electromagnetic spring it might refer to the magnets or coils generating the fields and in the case of an optical spring it might refer to the laser. An acceleration and displacement of the support will also accelerate and displace the rest position of the oscillator. We consider a inertial reference frame and denote the positions of the oscillator and the support with respect to this frame by x and ϵ, respectively (cf. Fig. 3). We set $\delta' = x - \epsilon$ and then define $\delta = \delta' - \langle\delta'\rangle$, such that δ denotes the displacement of the oscillator from its rest position. Any force acting on the support is transferred to the oscillator only via the spring and the equation of motion for the oscillator now reads

$$F = m\ddot{x} = -m\gamma\dot{\delta} - k\delta$$

[3]Multiply Eq. 6 by $(m_1, ..., m_N)$ and note that $k_{i,j} = k_{j,i}$. Also, strictly speaking, the characteristic polynomial of this matrix is of order $2N$ in λ and thus $2N$ eigenvalues exist. For each eigenvalue its complex conjugate is also an eigenvalue (this follows from the complex conjugate root theorem) [Jef05].

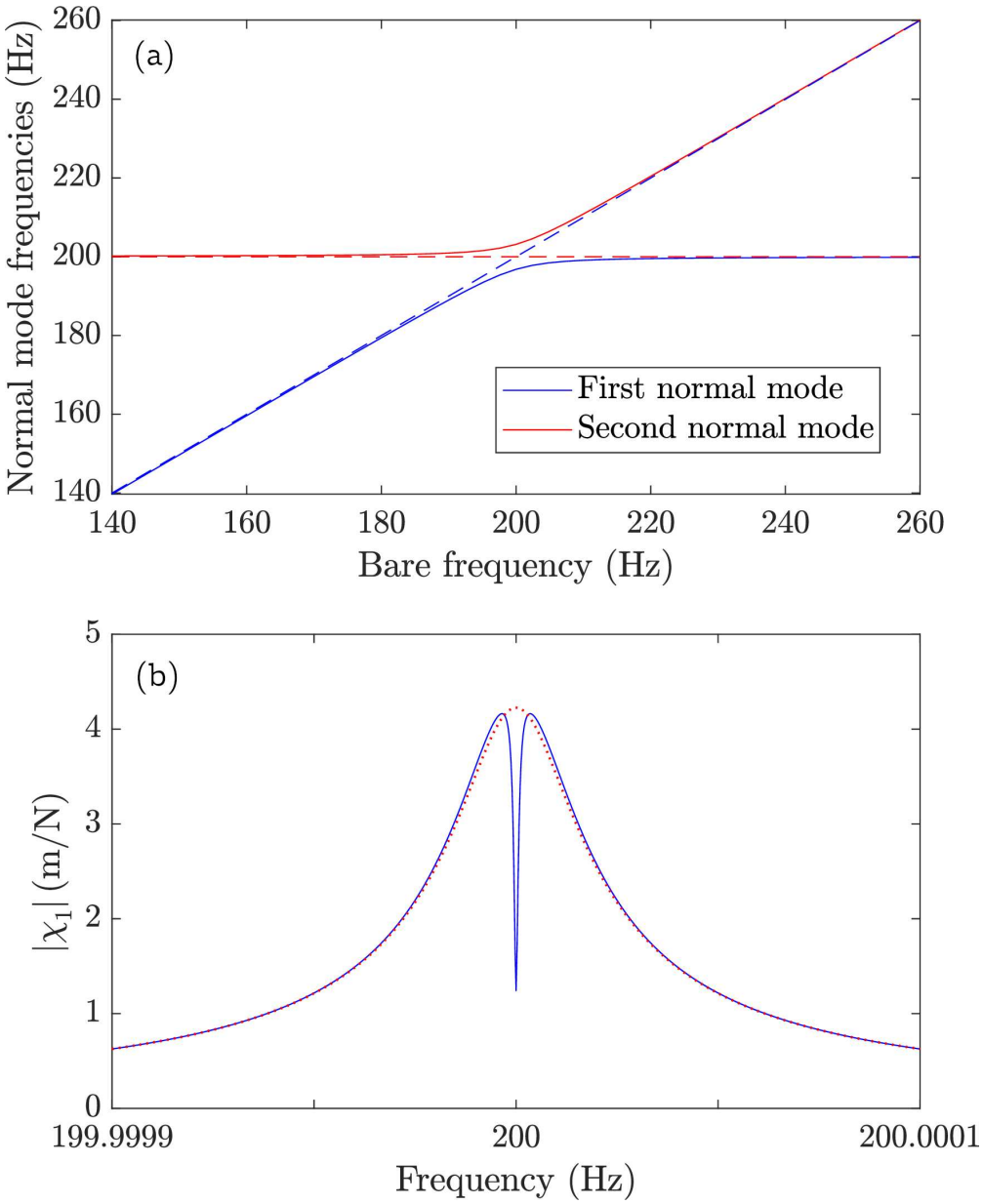


Figure 2: (a)The normal mode frequencies of a system of two coupled harmonic oscillators are plotted against the bare (uncoupled) resonance frequency of one of the oscillators, which is assumed to be tunable. The resonance frequency of the other oscillator and all other parameters are constant. When the resonance frequencies are close, the normal mode frequencies differ from the bare frequencies and both oscillators contribute to each mode. If the coupling rate is strong compared to the dissipation (for two identical oscillators the exact condition is $\frac{|k_{1,2}|}{m} > \gamma\omega_0$), the normal modes can be spectrally resolved. This is called an avoided crossing (as the normal mode frequencies never cross). The dashed lines correspond to the bare frequencies. (b)Even for fairly weak coupling, such that the normal modes cannot be resolved, the coupling can modify the response of the oscillators to a weak drive signal (i.e. their apparent susceptibility). Plotted is the apparent susceptibility of one oscillator (1) weakly coupled to a second oscillator (2) with $\omega_2 = \omega_1 = 2\pi \times 200\,\mathrm{Hz}$ and $\gamma_2 \ll \gamma_1$. The susceptibility of oscillator 1 shows a dip at the resonance frequency of the oscillator 2 (which does not necessarily have to be equal to ω_1), hence the name induced transparency. This can be viewed as the back action force from the second oscillator negatively interfering with the drive signal acting on the first oscillator. The red dotted line is the susceptibility for an uncoupled oscillator with otherwise identical parameters.

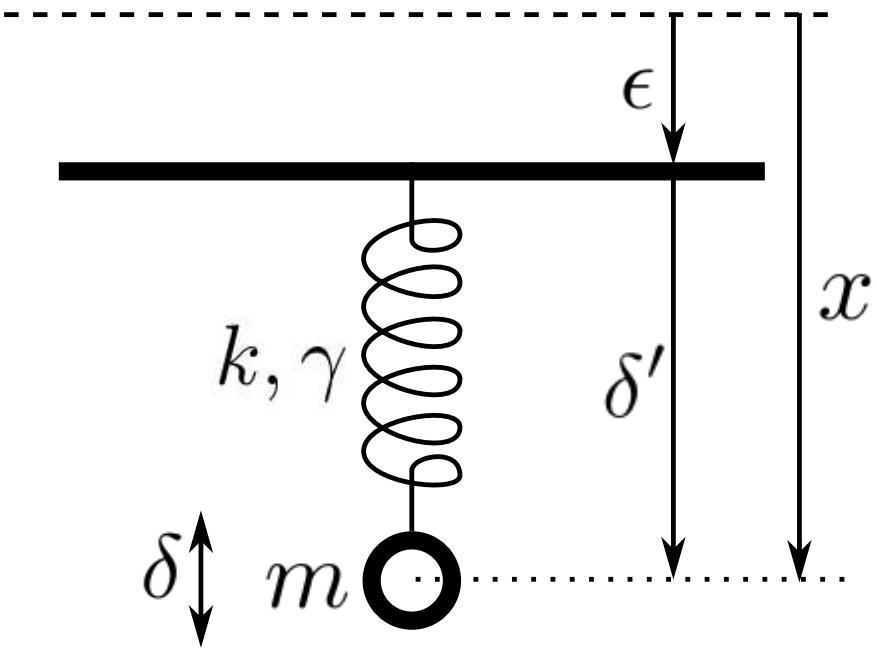


Figure 3: The oscillator is connected to its support via the spring, ϵ and x denote the position of the support w.r.t. an inertial system. δ' denotes the position of the oscillator relative to its support and $\delta = \delta' - \langle\delta'\rangle$ is the instantaneous displacement of the oscillator from its rest position.

or, rewriting this,

$$\ddot{\delta} + \gamma\dot{\delta} + \omega_0^2\delta = -\ddot{\epsilon}. \tag{7}$$

Note that we have made the assumption that the damping is associated with the spring, i.e. with the movement of the oscillator relative to its support. This is the relevant case for us, but it is not a general rule - depending on the damping mechanism the damping force might be proportional to $\dot{x}$ rather than $\dot{\delta}$ (e.g. if the dominant damping mechanism is gas damping and the gas is not affected by the movement of the support). We have also assumed that the support is a single, rigid component such that any displacement of the support transfers one-to-one into a displacement of the oscillator's rest position. We have written the equation in terms of δ because this is the quantity we intend to measure (in our case the measurement device is rigid and fixed to the same support) - again, this is something that is setup-dependent and not a general rule (a laser and photodiode at rest w.r.t. the inertial frame would measure x rather than δ).

Comparing equation 7 to equation 1 we see that the effect of the vibrations manifest as an additional force $m\ddot{\epsilon}$ acting on the oscillator (with the corresponding power spectral density $m^2\omega^4 S_{\epsilon\epsilon}$). Including the thermal force, this leads to (cf. Eq. 2)

$$S_{\delta\delta} = |\chi|^2 \left(m^2\omega^4 S_{\epsilon\epsilon} + 4k_B T m\gamma\right).$$

It is also interesting to note that environmental vibrations often decrease as $S_{\epsilon\epsilon} \propto \omega^{-4}$, so $\omega^4 S_{\epsilon\epsilon}$, which corresponds to the acceleration PSD, is approximately constant over wide frequency bands [Eva17], although there are exceptions for low frequencies where the vibrations are primarily caused by human activity [RG15, DRSPR17]. For high-Q oscillators it is thus often a good assumption that $\omega^4 S_{\epsilon\epsilon}$ does not change a lot around the resonance peak compared to the susceptibility and if we are interested only in the resonant motion we can replace it with $\omega_0^4 S_{\epsilon\epsilon}(\omega_0)$.

We can then define an effective temperature for the resonant motion,

$$T_{eff} = \frac{m\omega_0^4 S_{\epsilon\epsilon}(\omega_0)}{4k_B\gamma},$$

such that $S_{\delta\delta}(\omega) = |\chi(\omega)|^2 (4k_B T_{eff} m\gamma)$. For a low dissipation, this term can be much higher than the thermal noise term and limit e.g. the sensing capabilities of the oscillator.

2.6 Vibration isolation

We have introduced the effects of vibrations on a harmonic oscillator in the last section and found that vibrations of the trap drive the motion of the particle. This is usually unwanted in engineered oscillators, as most applications benefit from a low environmental excitation rate. We have already seen that vibrations limit the sensing capabilities of an oscillator, they also impede feedback cooling [HGH+23] and cause decoherence if the oscillator is in a quantum state [PPCS+18]. Fortunately it is possible to suppress vibrations by multiple means, including passive vibration isolation, active vibration isolation and quasi-zero-stiffness systems [MZY22]. I will focus here on a passive vibration isolation system that utilizes the frequency response characteristics of harmonic oscillators. This corresponds to the system that we used in [HGH+23]. The main principle is shown in Fig. 4a : The system to be shielded from environmental vibrations (the "Experiment") at a target frequency ω_t is suspended by a spring with an associated spring constant k and damping γ. As shown in the previous section, and using the same notation, the vibrations of the system are then related to the environmental vibrations by the mechanical susceptibility of the spring:

$$S_{xx}(\omega) = |\chi(\omega)|^2 m^2 (\omega_0^4 + \gamma^2\omega^2) S_{\epsilon\epsilon}(\omega) = \frac{\omega_0^4 + (\gamma\omega)^2}{(\omega_0^2 - \omega^2)^2 + (\gamma\omega)^2} S_{\epsilon\epsilon}(\omega).$$

Remember that x refers to the oscillator's position with respect to an inertial frame. For small γ the power spectral density S_{xx} drops as $\frac{1}{\omega^4}$ above the resonance frequency ω_0 (cf. Fig. 4b). Note that eventually, at typically very high frequencies on the order of $\frac{\omega_0^2}{\gamma}$, this changes to a $\frac{1}{\omega^2}$ behavior, but this frequency range usually is not of interest anymore (and, for these frequencies, other phenomena might dominate the behavior of the system, e.g. internal resonances of the spring). For frequencies below the resonance frequency S_{xx} is flat, meaning that the oscillator follows its support. So, for $\omega_t \gg \omega_0$ environmental vibrations are suppressed approximately by a factor $\frac{1}{\omega_t^4}$ in power, or by a factor $\frac{1}{\omega_t^2}$ in amplitude. This is the reason we can use a system that behaves like a harmonic oscillator for vibration isolation. From the preceding discussion it should be clear that vibration isolation does not necessarily mean a reduction in the overall magnitude of the vibration (i.e. $\langle x^2 \rangle$ is not necessarily smaller than $\langle \epsilon^2 \rangle$), since the vibrations are only reduced at higher frequencies but amplified on resonance (and approximately equal below resonance).

It is interesting to compare S_{xx} to $S_{\delta\delta}$, which is given by

$$S_{\delta\delta}(\omega) = |\chi(\omega)|^2 m^2 \omega^4 S_{\epsilon\epsilon}(\omega) = \left| \frac{\omega^2}{(\omega_s^2 - \omega^2 - i\omega\gamma_s)} \right|^2 S_{\epsilon\epsilon}(\omega).$$

We can see that here the asymptotic behavior for large frequencies is flat and the PSD decreases for decreasing frequencies (cf. Fig 4c). Again, this just states that the oscillator follows its support for low frequencies ($\delta \to 0$) and the oscillator's movement is suppressed for large frequencies ($x \to 0$ or $\delta \to \epsilon$, i.e. the support moves around the oscillator). The takeaway here is that this means that a measurement of δ cannot provide direct information about the vibration isolation characteristics at higher frequencies; for this one has to

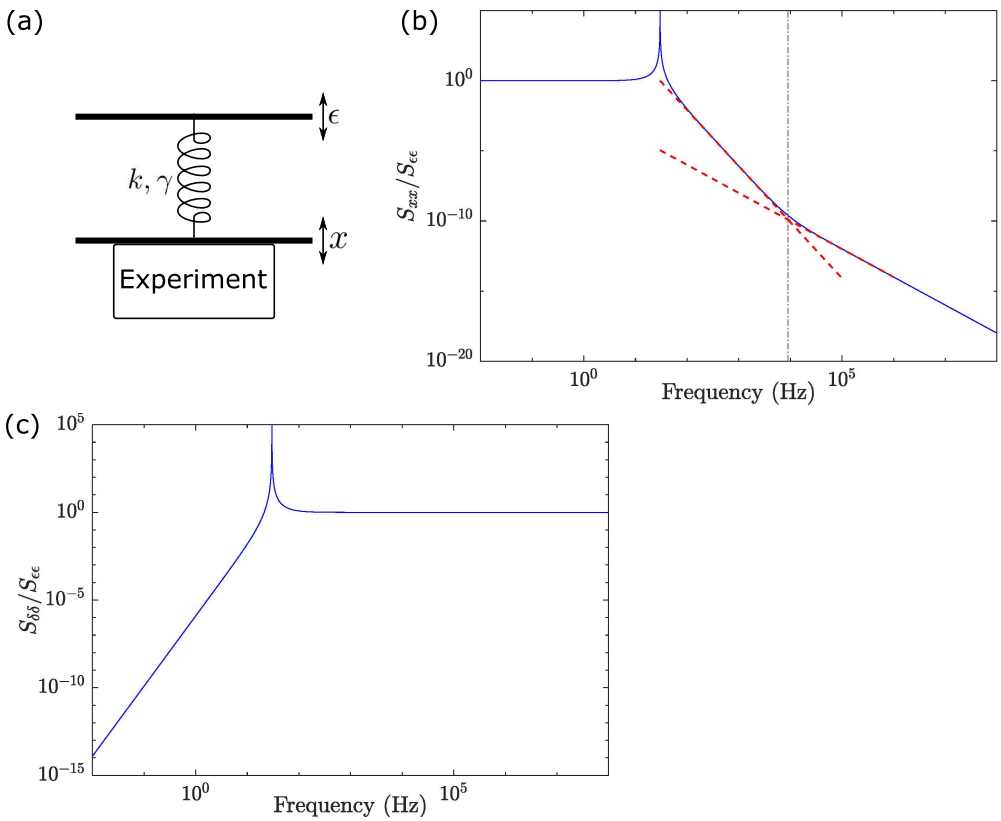


Figure 4: Principle of passive vibration isolation. (a)The experimental stage is connected to the support via a spring with spring constant k. (b)Above the resonance frequency $\omega_0 = \frac{1}{2\pi}\sqrt{\frac{k}{m}}$ the power spectral density of the experimental stage's motion x drops off as $\frac{1}{\omega^4}$ when compared to the motion of the support ϵ. The coordinates x and ϵ refer to an inertial system (in practice a valid approximation might be the coordinate system associated with the laboratory). The dashed red lines highlight the change of the $\frac{1}{\omega^4}$ behavior to a $\frac{1}{\omega^2}$ behavior at $\omega = \frac{\omega_0^2}{\gamma}$ (vertical line).(c)The transfer function for the relative distance between support and experimental stage, $\delta = x - \epsilon$. Note that $x \to 0$ means $\delta \to \epsilon$, i.e. at high frequencies the support moves around the experiment (as seen from the inertial system).

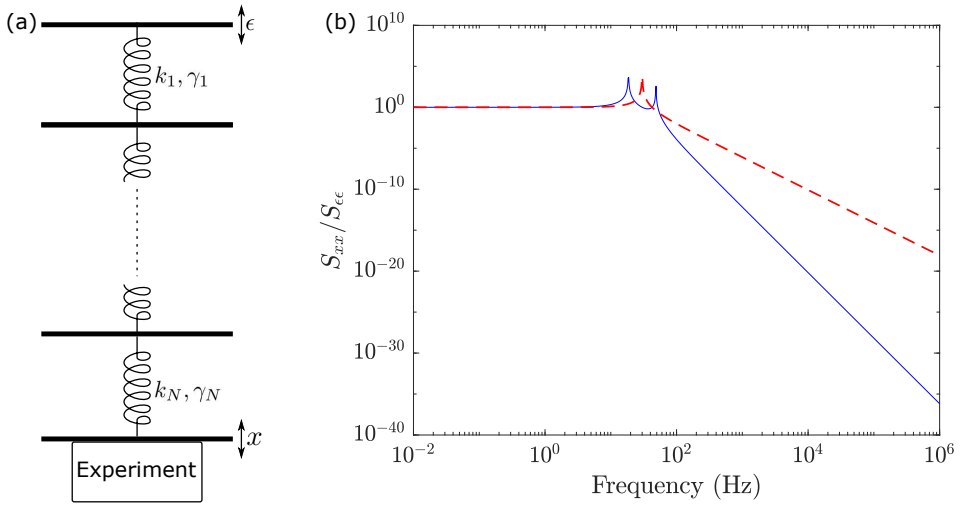


Figure 5: (a)Multiple vibration isolation stages can be constructed in series, this leads to a steeper drop-off of the transfer function above the normal mode frequencies. (b)Comparison of a two-stage system (solid blue line) with a one-stage system (dashed red line).

measure x (or $\ddot{x}$ - in practice, usually an accelerometer is used, as it is easier to measure the acceleration than the position).

The degree of vibration isolation at a target frequency $\omega_t \gg \omega_0$ with a single stage system (stage refers to the combination of the spring and the attached platform) as discussed above is thus determined solely by the resonance frequency of the spring ω_0 (assuming $\gamma \ll \omega_0$). If one needs a very good isolation, one option is to make the resonance frequency very small. However, depending on the implementation of the spring there is usually a lower limit to its resonance frequency which directly translates into a limit for the vibration suppression. Another option that is available to us is to modify the scaling by adding more springs in series, as depicted in Fig. 5a. Solving the system of equations for the coupled oscillators, as outlined in section 2.4 (cf. Eq. 6), and assuming negligible damping, leads to the simple transfer function

$$\frac{S_{xx}}{S_{\epsilon\epsilon}} = \left(\prod_{i=1}^{N} \frac{\omega_i^2}{\omega_{n,i}^2 - \omega^2} \right)^2 ,$$

where N is the number of springs, $\omega_i = \sqrt{\frac{k_i}{m_i}}$ refers to the uncoupled resonance frequencies and $\omega_{n,i}$ denotes the normal mode frequencies. The asymptotic behavior above the highest normal mode resonance frequency thus scales as $\frac{1}{\omega^{4N}}$ (cf. Fig. 5b), or $\frac{1}{\omega^{2N}}$ for the amplitudes.

A practical intricacy in the design of a vibration isolation system is that each spring has multiple degrees of freedom, which might be coupled to each other. This leads to more, and in general more complex, equations, but the procedure for finding the solution stays the same (as long as the system behavior is harmonic for each degree of freedom). Instead of setting up the analytical equations and solving them one can also use numerical simulations to find the solution. For more complex system this is usually the simpler approach, as one only has to input the geometry and the material parameters.

In [HGH+23] I present a practical 3-stage vibration isolation for all degrees of freedom.

3 Magnetic levitation

Magnetic levitation is a term enveloping many different methods, with the common property that magnetic forces are used to hold the levitated object (levitator) without any mechanical contact to its surroundings. Broadly speaking, most methods can be characterized either as dynamic levitation (the magnetic field that supports the levitator is generated by a time-dependent current) or static levitation[4] (the field is generated by a direct current or permanent magnet). The levitator could be a conductor [MDB+23], a permanent magnet [Ark47], a diamagnet [BG97], a type-II superconductor [Bra88] or a type-I superconductor [HGH+23]. The working mechanisms of all of these types of magnetic levitation are different, and each one comes with its advantages and disadvantages. For us, because the ultimate motivation for the experiment is the preparation and manipulation of a quantum state, the most important factor when we decided on a specific platform for magnetic levitation was the level of dissipation and decoherence that could, in principle, be achieved. In this respect the decision to use passive levitation of a type-I superconductor was relatively clear, as this avoids dissipation due to hysteresis and eddy currents, which is unavoidable for the other levitation schemes. In this chapter I introduce the theory governing the levitation of zero-field-cooled superconductors. After a brief overview of the phenomenological London theory I show that a superconducting sphere in an external magnetic quadrupole field experiences a force proportional to the gradient of the magnetic field strength and in the opposite direction. As a direct consequence it follows that the superconducting sphere can be stably levitated in the minimum of the magnetic field (more details on this, including for non-spherical geometries, are given in the subsequent chapters describing the publications [HA19, HGH+23]). Following that I present some configurations of current-carrying coils and wires that are capable of generating suitable trapping potentials. I show how several trap potentials (harmonic, quartic, repulsive) can be realized by simply changing the current through one or more wires. I also calculate the coupling strengths relating the motion of the sphere to the currents induced in a superconducting loop placed in the vicinity of the sphere. Finally I discuss some subtleties that can arise in practical experiments, as well as dissipation due to eddy currents and how to avoid it. I will use the following notation: $\mathbf{E}$ stands for the electric field, $\mathbf{B}$ for the magnetic field, $\mathbf{j}$ for the current density and μ_0 is the vacuum permeability. It should be noted that throughout the derivations I assume that a quasi-static approximation is valid, i.e. I assume that the field distribution, the currents, as well as the forces around the superconductors are well described by the Maxwell equations in the form

$$\nabla \times \mathbf{E} = -\partial_t \mathbf{B},$$

$$\nabla \mathbf{B} = 0$$

and

$$\nabla \times \mathbf{B} = \mu_0 \mathbf{j}, \tag{8}$$

as well as the London equation (introduced below) inside the superconductor. This is a reasonable assumption, given that the expected frequencies are on the order of hundreds of Hertz[5]. In addition, it is validated by the excellent agreement of the experimental results with the theory [HGH+23].

[4]Note that static levitation, as we use the term here, does not necessarily mean that the field is time-independent. As an example, a permanent magnet can be stably levitated above a superconducting surface. When it oscillates around its rest position the field changes accordingly (and the currents induced in the superconductor result in the restoring force enabling levitation).

[5]In order for these equations to approximate the actual field distribution around the superconductor and therefore provide the correct dynamics of the superconductor inside the fields, the finite propagation

3.1 Superconductivity and the London theory

The defining characteristic of superconductors is their perfect conductivity. Other than that, they are broadly divided into two classes called type-I and type-II, both of which possess distinct properties. Common to both types is that superconductivity occurs only below a certain temperature (the transition temperature) and below a certain magnetic field strength (the critical field). The critical field depends on the temperature of the superconductor and increases with decreasing temperature.

Type-I superconductors are characterized by the expulsion of magnetic fields from the interior of a bulk superconductor (in addition to the vanishing electrical resistance). This is known as the Meissner effect and can be viewed as near-perfect diamagnetism. The magnetic field decreases exponentially with the distance from the surface, the characteristic length of this decrease is called the London penetration depth and usually denoted by λ. An example of this behavior is shown in Fig. 6, where we plot the magnetic field distribution for a superconducting sphere in a homogenous magnetic field. Both phenomena (perfect conductivity and flux exclusion) occurring in type-I superconductors can be described by the London equation

$$\Delta \mathbf{A} = \frac{1}{\lambda^2}\mathbf{A}, \tag{9}$$

where $\mathbf{A}$ is the vector potential in the London gauge [Tin96]. If the dimensions of the superconductor are very large compared to the penetration depth, $\lambda \to 0$ is usually a good approximation. In this case $\mathbf{j} = 0$ inside the superconductor and the current can only flow on the boundary, which implies $\mathbf{B} \cdot \mathbf{n} = 0$ on the boundary, $\mathbf{B}$ denoting the magnetic field outside the superconductor and $\mathbf{n}$ the surface normal vector on the boundary.

Type-II superconductors do not fully expel the magnetic field. As a consequence, if such a superconductor is cooled through its transition temperature while a magnetic field is applied, the field will be frozen-in and the superconductor becomes magnetized. If the superconductor is cooled through its transition temperature without an applied magnetic field, however, due to the perfect conductivity it will then react to later changes of the field like a type-I superconductor: The induced surface currents act to keep the interior field-free and the zero-field-cooled superconductor behaves again like a near-perfect diamagnet. However, this description is correct only for low magnetic fields. Above a certain cutoff value some of the field will enter the superconductor. This cutoff value is commonly called the lower critical field (because it is lower than the cutoff value for perfect conductivity, at which the material stops being superconducting). We will from now on assume that we are in one of the following regimes: (i)Type-I superconductor below the critical field or (ii)Zero-field cooled type-II superconductor below the lower critical field.

Finally, we should note that the behavior described above becomes more complex if the superconductor contains holes. In that case, the flux through the hole is conserved since any

speed of the fields has to be negligible, i.e. $\omega l \ll c$. In our case ω is the oscillation frequency of the trapped superconductor, l the length scale corresponding to the size of the superconductor and c the speed of light. Typical values for our experiments put $\frac{c}{l}$ in the high-frequency microwave regime. In addition, if the frequency is higher than the superconducting energy gap of the material of the levitator, it will no longer behave like a superconductor [Tin96]. For typical materials the energy gap lies also in the high-frequency microwave regime [Tin96]. Other effects could become relevant at lower frequencies: The movement of the superconductor around the trap center results in an oscillating field and therefore radiates energy [Jac99]. Further, even far below the superconducting energy gap, for finite frequencies the superconductor is not completely loss-less anymore but exhibits a finite frequency-dependent resistance [Tin96]. The dissipation due to these effects could, in principle, be observed at any frequency, if the dissipation from other sources is sufficiently small. However, it is currently still several orders of magnitude below the observed experimental dissipation [HGH+23].

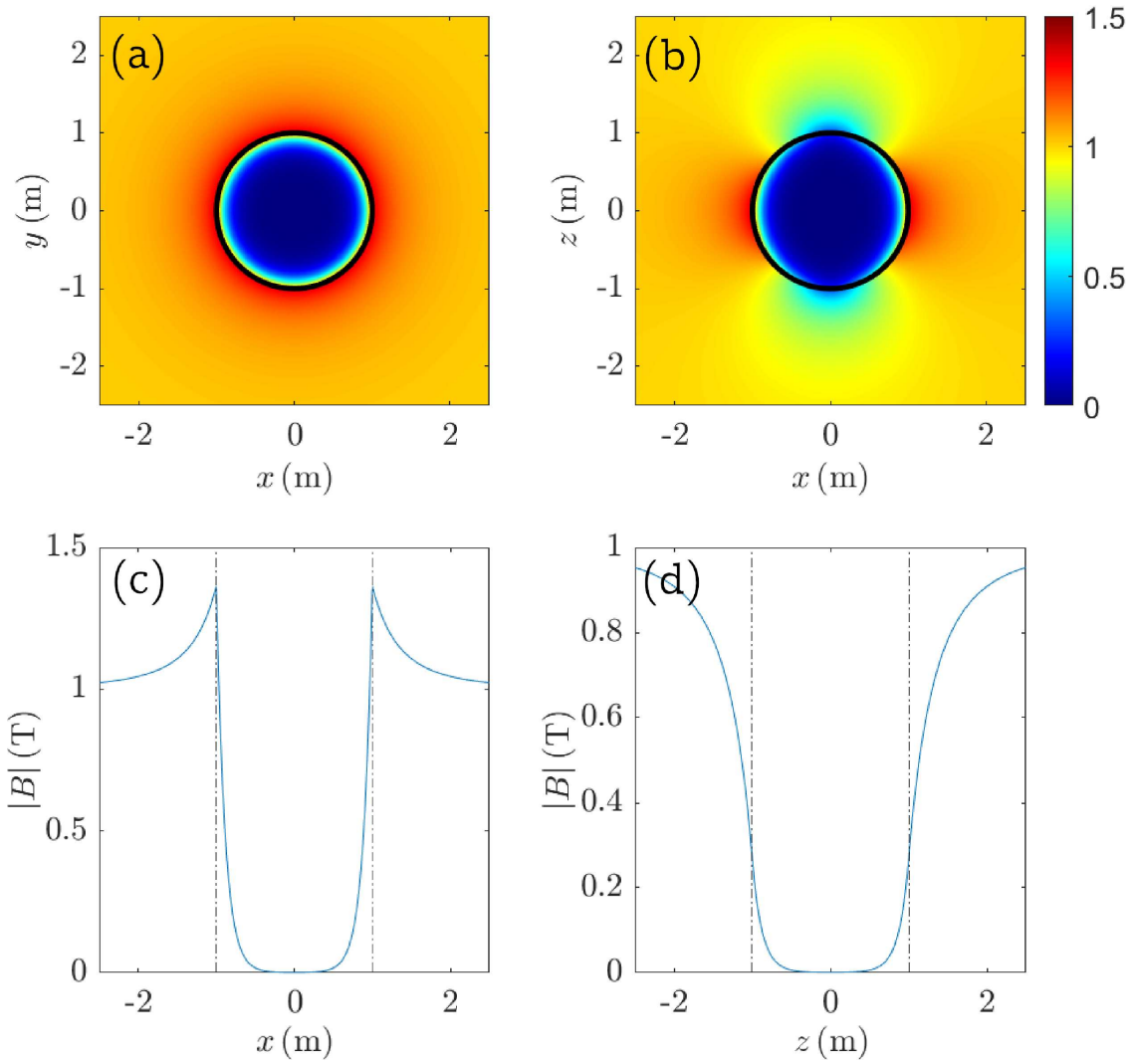


Figure 6: Field distribution in and around a superconducting sphere of radius $R = 1\,\mathrm{m}$ and London penetration depth $\lambda = \frac{R}{10}$ in a homogenous field with field strength 1 T oriented along the z-axis. Displayed is the field norm $|B|$ in the xy-plane (a), in the xz-plane (b), along the x-axis (c) and along the z-axis (d).

change in the flux due to the applied magnetic field is counteracted by the induced currents running around the hole [Tin96]. For a zero-field-cooled superconductor with dimensions well above the London penetration depth we therefore get the relation

$$\phi = LI + \phi_{ext} = 0,$$

where ϕ_{ext} is the external flux due to the applied field, L is the inductance and I the induced current.

3.2 Levitation of superconductors

When evaluating the force on a diamagnetic body in an external magnetic field $\mathbf{B_0}$ one usually assumes the magnetic susceptibility to be small, such that the induced field is negligible [BG97]. It is then straightforward to show that the magnetic energy of an isotropic diamagnet in the external field is proportional to $\int dV \left|\mathbf{B_0}\right|^2$, where the integration runs over the volume V of the diamagnet. Often $\int dV \left|\mathbf{B_0}\right|^2 \approx V \left|\mathbf{B_0}\left(\mathbf{x_0}\right)\right|^2$, where the field on the right-hand-side is evaluated at the geometric center $\mathbf{x_0}$ of the diamagnet, and the potential energy is thus minimized if the diamagnet is in zero field or in a local minimum of the applied field. Any displacement from such a minimum will then lead to an opposing force, such that the diamagnet can be stably confined. Assuming that the potential well is deep enough, inclusion of the gravitational energy will simply shift the minimum and stable levitation is possible.

For a superconductor, however, the induced field cannot be neglected. To derive an explicit expression for the force acting on the superconductor, i.e. to calculate the induced currents, one has to know the geometry of the superconductor and the form of the applied field. Even then an analytical solution need not necessarily exist. These calculations, both analytical and numerical, are presented in the manuscripts [HA19, Hof24] for an applied quadrupole field and spherical resp. cylindrical superconductors. The results show that magnetic levitation of spherical and cylindrical superconductors in a field minimum is possible and that the quadrupole field corresponds to a harmonic potential. Similar results have been found for superconducting rings [NMTS21] and perfectly diamagnetic ellipsoids, cylinders and cuboids [BSCSDV+24] (as discussed in the previous section, results for perfect diamagnets apply to superconductors when the penetration depth is negligible).

In the remainder of this section I derive the force on a superconducting sphere in an external field of the form

$$\mathbf{B_0}\left(\mathbf{x}\right) = \left(b_x(x+x_0), b_y(y+y_0), b_z(z+z_0)\right),$$

with $\sum_i b_i = 0$ and $\mathbf{x} = (x, y, z)$ (we will also use the corresponding spherical coordinates (r, Θ, ϕ) below), and show that the sphere can be levitated in the field minimum. Such a field can be generated by a simple arrangement of coils (examples are given in the next section). The calculation is a generalization of the calculation that I present in [HA19], where I derive the field distribution for the special case $b_x = b_y = -\frac{1}{2}b_z$. We work in a coordinate system with the superconducting sphere at its center, i.e. $\mathbf{x_0} = (x_0, y_0, z_0)$ is the displacement of the sphere from the minimum of the quadrupole field, a schematic drawing is shown in Fig. 7. We denote the field inside the sphere as $\mathbf{B_{in}}$ and the field outside as $\mathbf{B_{out}}$. As there are no currents outside the sphere, we can define a scalar potential Φ such that $\mathbf{B_{out}} = \mathbf{B_0} - \nabla\Phi$ and $\Delta\Phi = 0$ [Jac99]. The field inside the superconductor obeys the London equations, i.e. $\mathbf{B_{in}} = \nabla \times \mathbf{A_{in}}$ and $\Delta\mathbf{A_{in}} = \frac{1}{\lambda^2}\mathbf{A}$. In the general case the boundary condition on the surface of the superconductor is simply $\mathbf{B_{in}} = \mathbf{B_{out}}$ (as discussed above, in the case $\lambda = 0$ the boundary condition is $\mathbf{B_{in}} = 0$ and $\mathbf{n}\mathbf{B_{out}} = 0$ with $\mathbf{n}$ being the boundary normal vector). We note that physical solutions to the Maxwell-London-equations require

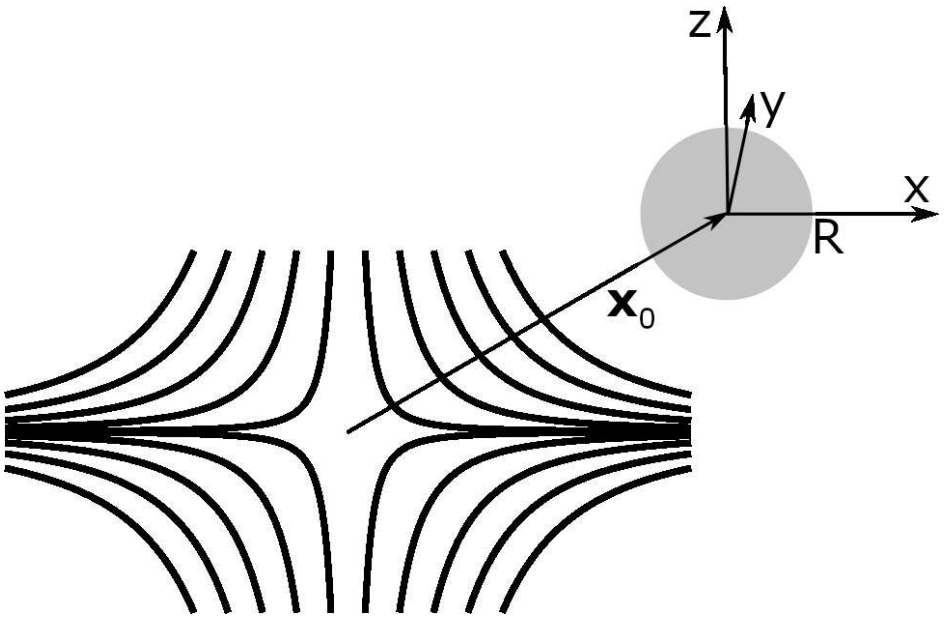


Figure 7: (a)The superconducting sphere is displaced by $\mathbf{x_0}$ from the center of the quadrupole field, which is represented by its field lines in the xz-plane.

the field to be finite inside the superconductor and $\mathbf{B_{out}} \to \mathbf{B_0}$ for $|\mathbf{x}| \to \infty$. In this case the unique solutions for the fields, expressed as an expansion in vector spherical harmonics $\mathbf{Y}_n^m$,$\mathbf{\Psi}_n^m$,$\mathbf{\Phi}_n^m$, are [HA19]

$$\mathbf{B_{in}} = -\frac{1}{r}\sum_{n=0}^{\infty}\sum_{m=-n}^{n} c_{n,m}\left[n(n+1)\, i_n\left(\frac{r}{\lambda}\right)\, \mathbf{Y}_n^m + \partial_r\left(r\, i_n\left(\frac{r}{\lambda}\right)\right)\, \mathbf{\Psi}_n^m\right]$$

and

$$\mathbf{B_{out}} = \mathbf{B}_0 + \sum_{n=0}^{\infty} r^{-(n+2)} \sum_{m=-n}^{n} a_{n,m}\left((n+1)\,\mathbf{Y}_n^m - \mathbf{\Psi}_n^m\right), \tag{10}$$

Here i_n denotes the modified spherical Bessel functions [AS64]. The coefficients $a_{n,m}, c_{n,m}$ can now be determined from the boundary condition as

$$\begin{aligned}
a_{1,0} &= -\, f_1\left(\frac{\lambda}{R}\right)\, \sqrt{\pi/3}\; R^3 b_z z_0,\\
a_{1,-1} &= -\, f_1\left(\frac{\lambda}{R}\right)\, \sqrt{\pi/6}\; R^3 (b_x x_0 + i b_y y_0),\\
a_{1,1} &= \quad f_1\left(\frac{\lambda}{R}\right)\, \sqrt{\pi/6}\; R^3 (b_x x_0 - i b_y y_0),\\
a_{2,0} &= -\, f_2\left(\frac{\lambda}{R}\right)\, \sqrt{4\pi/45}\; R^5 b_z,\\
a_{2,-2} = a_{2,2} &= \quad f_2\left(\frac{\lambda}{R}\right)\, \sqrt{2\pi/135}\; R^5 (b_y - b_x)
\end{aligned}$$

and

$$\begin{aligned}
c_{1,m} &= \frac{3\lambda}{R^3\, i_2\left(\frac{R}{\lambda}\right)} a_{1,m},\\
c_{2,m} &= \frac{5\lambda}{2R^4\, i_3\left(\frac{R}{\lambda}\right)} a_{2,m}
\end{aligned}$$

with

$$f_1\left(\frac{\lambda}{R}\right) = 1 - 3\,\frac{\lambda}{R}\left(\coth\frac{R}{\lambda} - \frac{\lambda}{R}\right),$$
$$f_2\left(\frac{\lambda}{R}\right) = 1 - 5\,\frac{\lambda}{R}\left(\left(\coth\frac{R}{\lambda} - \frac{\lambda}{R}\right)^{-1} - 3\,\frac{\lambda}{R}\right).$$

Knowing the field distribution in and around the sphere, we can calculate the force exerted on the sphere as

$$\mathbf{F} = \frac{1}{\mu_0}\oiint dS\,\left[(\mathbf{nB})\mathbf{B} - \frac{1}{2}\mathbf{nB}^2\right], \tag{11}$$

where the surface integral is performed over the surface of the sphere and $\mathbf{B}$ can be either the inner or outer field distribution, as these coincide on the surface. This leads to

$$\mathbf{F} = -f_1\left(\frac{\lambda}{R}\right)\,\frac{3V}{2\mu_0}\left(b_x^2 x_0, b_y^2 y_0, b_z^2 z_0\right) \tag{12}$$

and corresponds to a harmonic potential with trapping frequencies

$$\omega_i = \sqrt{f_1\left(\frac{\lambda}{R}\right)\,\frac{3}{2\mu_0\rho}}\,|b_i|\,,$$

where ρ denotes the density of the sphere. For $\frac{\lambda}{R} \to 0$ we get $f_1, f_2 \to 1$, so these prefactors can be ignored when the size of the sphere is much larger than the London penetration depth of the superconductor. For most low temperature superconductors λ is on the order of tens of nanometers [Tin96].

This method for calculating the magnetic field distribution around a superconducting sphere is powerful, because it can easily be generalized to different external fields, as long as they can be expanded in vector spherical harmonics. Furthermore, in [HGH+23] I introduce a numerical model for solving this boundary value problem that also works with non-spherical superconductors and present some details for a cylindrical superconductor.

3.3 Trap configurations

We have seen in the last section that a zero-field-cooled superconducting sphere can be levitated in a magnetic field minimum. In this section we will look at how such a minimum can be produced. As we aim for zero-field cooling the particle in a cryostat and only turning on the magnetic field after the cryostat is cold, we will look exclusively at current-carrying wires and coils as field sources. Many suitable arrangements of wires and coils are already known from atom traps [FZ07], which also require a minimum in the magnetic field strength. I will now briefly introduce the Anti-Helmholtz trap, which leads to a harmonic potential for spherical (and cylindrical) superconductors, and then present a slight modification that enables switching between harmonic, quartic and multi-well potentials by simply changing the currents.

3.3.1 Anti-Helmholtz trap configuration

The original Anti-Helmholtz configuration is depicted in Fig. 8. It consists of two coaxial

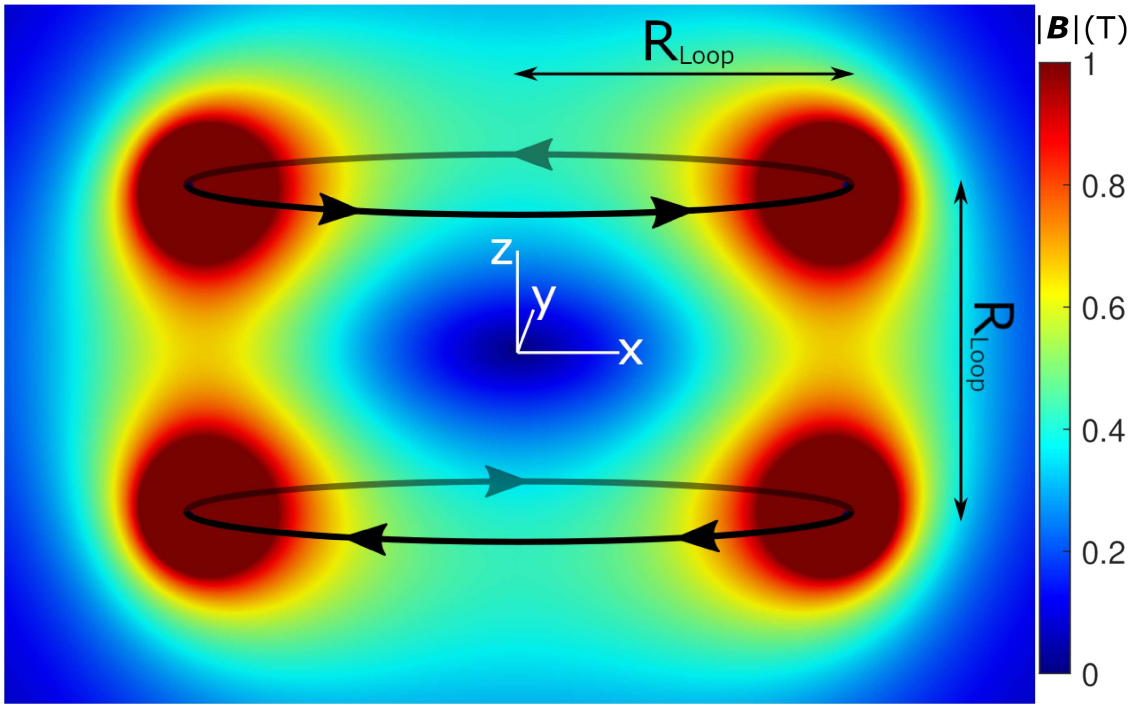


Figure 8: Schematic of an Anti-Helmholtz coil and the corresponding field strength in the xz-plane. The coils are coaxial and separated by a distance corresponding to their radius. The arrows depict the direction of the counter-propagating currents, which have the same magnitude for both coils.

current loops of radius R_{Loop} separated by a distance equal to the radius, and with counter-propagating currents of magnitude I. In this case the magnetic field near the center between the two loops is, to a good approximation, given by [RICN+12]

$$\mathbf{B}(\mathbf{x}) = \frac{1}{2} b_z \left(x, y, -2z\right) \tag{13}$$

with $b_z = \frac{24}{25\sqrt{5}} \frac{\mu_0 I}{R_{Loop}^2}$. This field has a minimum $|\mathbf{B}| = 0$ at the center and, as we have seen in the previous section, leads to a harmonic trapping potential for a spherical superconductor. Equation 13 remains correct even if the distance between the coils is not equal to the radius (but with a different expression for b_z). Also, since the field of multiple loops is simply the superposition of the individual fields, it remains correct when considering coils with multiple windings. A useful modification to this configuration is the use of elliptical coils to break the axial symmetry, as otherwise the frequencies of the c.o.m. modes of the trapped superconductor are degenerate along the x- and y-directions. We calculate the magnetic field produced by such a configuration numerically in [HGH+23] and find that

$$\mathbf{B}(\mathbf{x}) = \left(b_x x, b_y y, b_z z\right) \tag{14}$$

near the center, with $\sum b_i = 0$ and $b_i \propto I$.

3.3.2 Multi-potential trap configuration

We now consider a very simple alteration to the Anti-Helmholtz configuration as depicted in Fig. 9a. We add four wires parallel to the symmetry axis of the coils, each with a current of magnitude I_{Wire} and displaced by a distance d from the center (symmetrically, such that the intersection points of the wires with the xy-plane are the corners of a square). The field

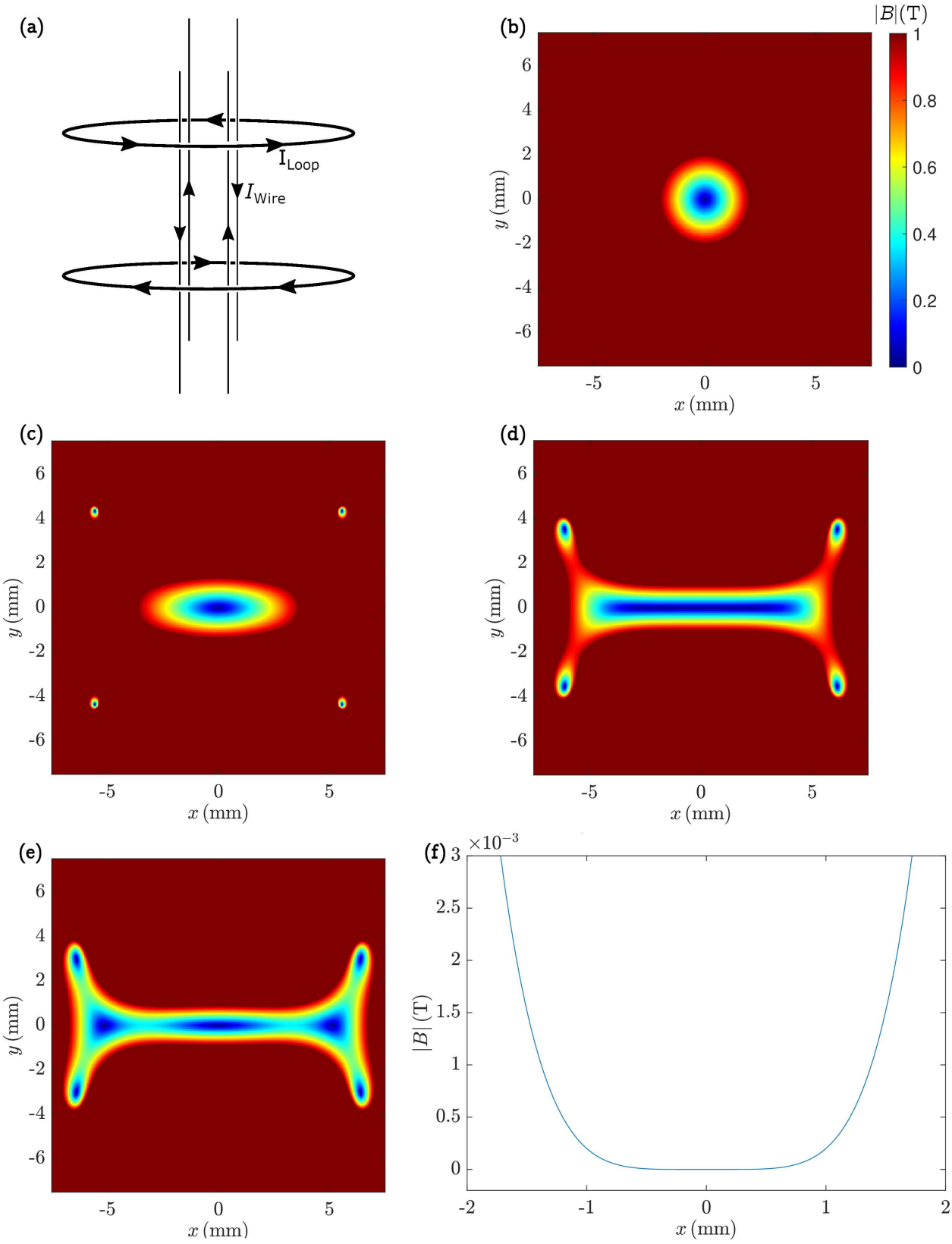


Figure 9: (a)Schematic of a trap that can generate different potentials for a levitated superconducting particle. (b-e)Field strength in the xy-plane corresponding to harmonic (b,c), quartic (d) and triple-well (e) potentials. The current through the wires is 0 A, 15 A, 31.25 A and 40 A, respectively, with $d \approx 7.07\,\text{mm}$ and $b_z = 1\,\text{T/m}$. (f)Field strength $|B|$ on the x-axis for the quartic potential, same parameters as in (d).

of a single wire is

$$\mathbf{B_{Wire}}(\mathbf{x}) = \pm \frac{\mu_0 I_{Wire}}{2\pi \left(\left(x \pm \frac{d}{\sqrt{2}} \right)^2 + \left(y \pm \frac{d}{\sqrt{2}} \right)^2 \right)} \left(- \left(y \pm \frac{d}{\sqrt{2}} \right), x \pm \frac{d}{\sqrt{2}}, 0 \right),$$

with the signs depending on the direction of the current and the displacement. The total field is then the sum of the AHC field and the fields of the wires. If the directions of the currents are chosen as depicted in Fig. 9a it is possible to switch between a 3D harmonic potential, a 2D harmonic and 1D quartic potential as well as a 2D harmonic and 1D triple well potential simply by changing the current through the wires[6]. As a straight wire has very little inductance, this current can be switched very fast compared to a typical mechanical period. In Fig. 9b-e we plot the magnetic field strength in the xy-plane for the three cases described above. I would like to emphasize that this is a more or less randomly chosen example configuration and, although it definitively has some practical applications, the main point I want to highlight in this section is the versatility of the potential landscape for magnetic levitation. The ability to rapidly alter the potential of a levitated particle is integral to some protocols for creating non-trivial quantum states, see e.g. [NCRI+24, RLRCC+24].

3.4 Coupling to an external circuit

As we have seen in the section 3.2, the field distribution around a superconducting sphere in a quadrupole field depends on its position. This enables us to infer the position of the sphere from a measurement of the field. In practice, the measured quantity is usually the magnetic flux through a certain area (simply because there are no practical measurement devices that measure the magnetic field at a single point). One possibility to measure the flux is to use a superconducting quantum interference device (SQUID), which is a flux sensor that can have a near quantum-limited sensitivity. Operating SQUIDs in large static fields (such as the trap field) can impede the performance of the SQUID [CK04]. Since we are only interested in the change of the flux due to the motion of the particle, we will use a flux transformer (cf. Fig. 10), i.e. we place a superconducting coil (pickup coil) close to the trap center, such that the fluctuations of the flux through the coil induce a current in it. This coil is connected to a second coil (SQUID input coil), which then changes the flux through the SQUID. One

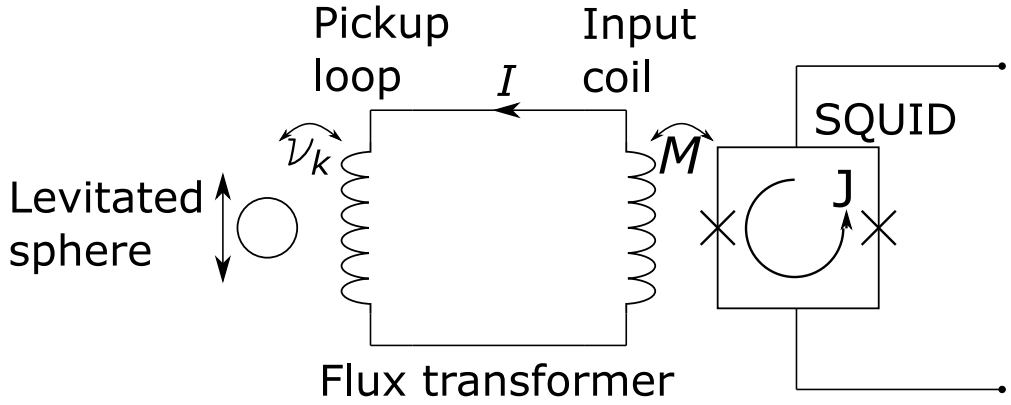


Figure 10: Schematic of a readout system. The motion of the levitated sphere is coupled to a SQUID via two superconducting coils (pickup loop and input coils) forming a flux transformer.

[6]We have already seen that the potential depends on the shape of the superconductor as well, the statements here are valid for a spherical superconductor.

should be aware that placing additional superconducting structures, such as pickup coils, near the trap center can alter the trap field and properties for several different reasons: First, as the pickup loop is made from superconductors and usually zero-field-cooled, it will also exclude the magnetic field from its interior. However, our pickup coils are made from thin films and have a thin wire width; simulations show that, for our setup, the influence of this effect on the field near the trap center is negligible. Second, the current that is induced in the flux transformer due to the particle motion will also effect a force back on the particle. As we will see below, if the flux transformer is superconducting and purely inductive, the currents will be in-phase with the motion of the particle and change the trap frequency. If the pickup coil is positioned such that it couples to multiple modes, this will also induce coupling between the different modes. Third, currents from other sources may be induced in the flux transformer. One unavoidable source of such currents is the SQUID itself, as the currents inside the SQUID necessarily couple back into the flux transformer. This is the origin of the back-action force (cf. section 2.2) in our setup.

We will now take a closer look at how to calculate the coupling to a pickup loop and a SQUID, as well as the back-action effects stemming from the induced currents.

To start, we look at how the flux through an arbitrary surface changes with the motion of the particle. The flux through a surface bounded by a closed path γ can be expressed as a path integral

$$\Phi_\gamma = \oint_\gamma \mathbf{A}\mathbf{t} dc,$$

where $\mathbf{A}$ is the vector potential and $\mathbf{t}$ the tangential vector along the path. Considering again a sphere in a quadrupole field, the vector potential outside the sphere is fully analytic and, in a coordinate frame with the trap center at the origin, given by

$$\begin{aligned}
\mathbf{A_{out}} &= \begin{pmatrix} b_y yz \\ -b_x xz \\ 0 \end{pmatrix} \\
&+ \frac{1}{2} f_1\left(\frac{\lambda}{R}\right) \frac{R^3}{r'^3} \left[b_x x_0 \begin{pmatrix} 0 \\ z - z_0 \\ -(y - y_0) \end{pmatrix} + b_y y_0 \begin{pmatrix} -(z - z_0) \\ 0 \\ x - x_0 \end{pmatrix} + b_z z_0 \begin{pmatrix} y - y_0 \\ -(x - x_0) \\ 0 \end{pmatrix} \right] \\
&+ \frac{1}{2} f_2\left(\frac{\lambda}{R}\right) \frac{R^5}{r'^5} \left[\frac{1}{3}(b_y - b_x) \begin{pmatrix} -(y - y_0)(z - z_0) \\ -(x - x_0)(z - z_0) \\ 2(x - x_0)(y - y_0) \end{pmatrix} + b_z (z - z_0) \begin{pmatrix} y - y_0 \\ -(x - x_0) \\ 0 \end{pmatrix} \right]
\end{aligned} \tag{15}$$

with $r' = \sqrt{(x - x_0)^2 + (y - y_0)^2 + (z - z_0)^2}$. This expression for the vector potential outside the sphere is obtained from Eq. 10 by expressing it in terms of a vector potential and changing frames. We need not consider the vector potential inside the sphere as any physical pickup loop cannot pass through the sphere. The expressions resulting from the path integral are, in general, cumbersome to write, but can be evaluated either numerically or analytically in a symbolic computation software such a MATHEMATICA for arbitrary pickup loop geometries. When the oscillations of the particle are small, it is often useful to consider just the linear parts of the Taylor expansion, i.e. the terms

$$\nu_k = \partial_k \Phi_\gamma|_{\mathbf{x_0}=0}$$

with $k \in \{x_0, y_0, z_0\}$. These terms are called the coupling strengths w.r.t. the individual modes (depending on the context, coupling strength might also refer to the absolute value). The meaning of the these terms is that for small oscillations of the particle around the rest

position the flux is given to a good approximation by

$$\Phi_\gamma(\mathbf{x_0}) \approx \Phi_\gamma(0) + \sum_k \nu_k k.$$

How small the oscillations need to be for this to be a good approximation depends, of course, on the exact values of ν_k relative to the higher order terms of the Taylor expansion.

We now assume that the closed path γ corresponds to a thin superconducting wire. As the wire forms a closed superconducting circuit with self-inductance L, the total flux through the wire is conserved, i.e.

$$\Phi = LI + \Phi_\gamma = const. \tag{16}$$

The constant term in this expression corresponds to the flux that was present when the loop became superconducting. We will from now on assume that the superconducting loop becomes superconducting only after the trap field has been established, with the sphere levitating at the minimum of the field. For small displacements Eq. 16 can then be written as

$$I \approx -\frac{\sum_k \nu_k k}{L}. \tag{17}$$

It is important to note that this is not a mere mathematical formality but corresponds to a specific experimental condition that needs to be fulfilled. If a superconducting ring is placed close to the trap center before the trap field is turned on, the currents induced in the ring during the build-up of the field would modify the final field and the trap parameters might be quite different than those of the unmodified quadrupole field. One can ensure this condition in practice by locally heating the wire and keeping it in the normal conducting state while ramping up the trap field to its final value - in the case of a flux transformer, small resistors are usually placed on the same wafer close to the superconducting wire precisely for this purpose.

We now consider the effect of the induced currents on the dynamics of the particle. An easy way to look at this problem is via the potential energy of the system including the currents in the ring, which, using Eq. 17, can be expressed as

$$U = \frac{1}{2} m \sum_k \left(\omega_k^2 + \frac{\nu_k^2}{mL} \right) k^2 + \frac{1}{2L} \sum_{k \neq p} \nu_k \nu_p \, k \, p. \tag{18}$$

One can see that the "back-action" effects of the superconducting loop modify the frequency and introduce a coupling between the individual modes. It is worth mentioning that for a 100 µm diameter sphere, even for optimal coupling, any of the terms $\frac{\nu_k \nu_p}{L}$ are more than three orders of magnitude smaller than any of the terms $m\omega_k^2$. This means that for most purposes, especially if the coupling strengths ν_k are not optimized, these terms will be negligible - this was also the case in the experiments described in [HGH+23], where the coupling strengths were several orders of magnitude below the optimum.

I stress again that we have made some assumptions in deriving this result. First, we have assumed that the quasi-static approximation is valid; this leads to currents and back-action forces that are in-phase with the motion of the particle. Second, we have assumed that the loop is zero-field-cooled in the presence of the trap field and the sphere at its center - this condition needs to be fulfilled experimentally, otherwise the modification of the trap field due to a constant current in the ring needs to be considered and the treatment above has to be adapted. Third, we have assumed that the oscillations of the sphere are small compared to the distance to the loop in order to linearize the coupling. If this is not the case, the full expression for the flux needs to be used in order to characterize the non-linear effects.

3.4.1 Coupling to a SQUID

We will now consider the case where we want to measure the currents that are induced in the superconducting circuit with a SQUID (Fig. 10). For our purposes here, we can consider the SQUID simply as a flux sensor. We can adopt the treatment introduced above, where ν still characterizes the coupling to the superconducting circuit. The coupling between the superconducting circuit and the SQUID is described by the mutual inductance M, such that the flux through the SQUID is given by

$$\Phi_S = IM = -\frac{M}{L}\sum_k \nu_k k = -\sum_k \eta_k k,$$

where we have defined the coupling strength w.r.t. the SQUID as $\eta_k = \frac{M}{L}\nu_k$. We have assumed here that there is no direct coupling between the levitated particle and the SQUID. This is ensured by a suitable design of the superconducting circuit connecting the sphere and the SQUID. For example, while the pickup loop needs to be located close to the levitated particle, the input coil and the SQUID can be located outside the trap, such that the SQUID and the levitated sphere are spatially separated. In addition the SQUID is often housed inside a magnetic shield.

Note that the effects described in the last section (modified spring constant, coupling between modes) are still present and depend only on the current I induced in the superconducting circuit by the particle motion. In addition, a current J in the SQUID (typically arising from thermal or zero-point fluctuations in the shunt resistors) will couple into the superconducting circuit and cause a force $\eta^2 J$ on the levitated particle. This force will drive the particle and, for a quantum-limited SQUID, results in the standard quantum limit for sensing the particle motion.

A thorough analysis describing both an optimization of the superconducting circuit connecting the motion of the levitated particle to the SQUID as well as the limits arising due to the intrinsic noise of the SQUID is presented in the supplementary of the manuscript [HGH+23].

3.5 Dissipation due to induced currents

The change in the magnetic field due to the movement of the superconducting particle will induce currents not only in a pickup-loop, but in any nearby conductors. As in the case of a superconducting pickup-loop, the induced currents will have a component that is in-phase with the particle motion, which can be treated exactly the same way as in the previous section (and will result in a modified trap frequency and coupled modes). However, if these conductors are resistive (i.e. not superconducting) the induced currents will also decay and have an out-of-phase component (shifted 90° relative to the particle motion), which leads to damping of the motion.

I will now quantitatively derive these effects, first analytically considering a conducting ring, and then the general equations that can be applied to conductors of arbitrary geometry. In the latter case there usually isn't a closed analytical expression and we will use finite element simulations to solve this case for some examples.

3.5.1 Dissipation in a conducting ring

Consider a conducting ring with inductance L and resistance $\mathscr{R}$ in the presence of an oscillating particle and denote the total flux through the ring by $\phi = LI + \phi_{ext}$, where I is the current flowing in the ring. From Faraday's and Ohm's laws it follows that $\mathscr{R}I + \dot{\phi} = 0$.

We will make the same assumptions as in the previous section, in particular that the external flux ϕ_{ext} through the ring depends, for each mode, linearly on the displacement of the particle, i.e. $\phi_{ext} = \sum_k \nu_k k$ with $k \in \{x_0, y_0, z_0\}$ (this is a valid assumption for small displacements and a suitable position of the ring, cf. section 3.4). Then the current in the frequency domain is

$$I(\omega) = -\frac{\omega^2 L + i\omega\mathscr{R}}{\mathscr{R}^2 + (\omega L)^2} \sum_k \nu_k k$$

and the components of the force on the particle due to the induced current are

$$F_{k,eddy} = -\frac{\omega^2 L + i\omega\mathscr{R}}{\mathscr{R}^2 + (\omega L)^2} \sum_p \nu_k \nu_p p.$$

Note that for $\mathscr{R} \to 0$ this reduces to the expressions (Eq. 18) from the previous section. For finite $\mathscr{R}$, the difference to the previous section is the presence of an out-of-phase component due to the imaginary part of I, which corresponds to an additional frequency-dependent damping force $-\frac{\nu_i^2 \mathscr{R}}{\mathscr{R}^2+(\omega L)^2}\dot{k}$ for each mode. If the overall damping of the oscillator is still small and if we are interested in the resonant motion, we can replace ω with the resonance frequency of the mode ω_i and write the additional damping as

$$\gamma_{i,eddy} = \frac{\nu_i^2 \mathscr{R}}{m(\mathscr{R}^2 + (\omega_i L)^2)}. \tag{19}$$

The damping for the i-mode is thus highest when the resistance of the ring matches $\omega_i L$, in which case

$$\gamma_{i,eddy} = \frac{\nu_i^2}{2m\omega_i L}.$$

We assume from now on that the ring is coaxial with the z-axis. In this case the coupling strengths obtained from Eq. 15 are $\nu_x = \nu_y = 0$ and

$$\nu_z = \pi b_z R_P^2 \left(\frac{R^2}{R_P^2 + Z_P^2}\right)^{\frac{3}{2}} \left(1 - \frac{R^2}{R_P^2 + Z_P^2}\left(1 - \frac{5Z_P^2}{R_P^2 + Z_P^2}\right)\right), \tag{20}$$

where R is again the radius of the superconducting sphere and R_P, Z_P are the radius and z-position of the conducting ring. Note that the right-hand-side term comes from the quadrupole component of the vector potential and can be neglected if we assume that the ring is far away from the levitated particle ($R_P \gg R$ or $Z_P \gg R$). In this case Eq. 20 reduces to

$$\nu_z^{DP} = \pi b_z R_P^2 \left(\frac{R^2}{R_P^2 + Z_P^2}\right)^{\frac{3}{2}}.$$

3.5.2 Finite element method

In the general case one has to consider Ohm's law $\mathbf{j} = \sigma\mathbf{E}$ in addition to Maxwell's equations. Here σ denotes the local conductivity of the material and $\mathbf{E}$ the induced electric field, which is related to the magnetic field fluctuations by $\mathbf{E} = -\partial_t \mathbf{A}$ or, in the frequency domain, $\mathbf{E} = -i\omega\mathbf{A}$. $\mathbf{A}$ is again the vector potential in the Coulomb gauge. These equations can be solved numerically (e.g. in COMSOL) and the total dissipated power is then obtained by integrating $\sigma\mathbf{E}^2$ over the volume of the conductor.

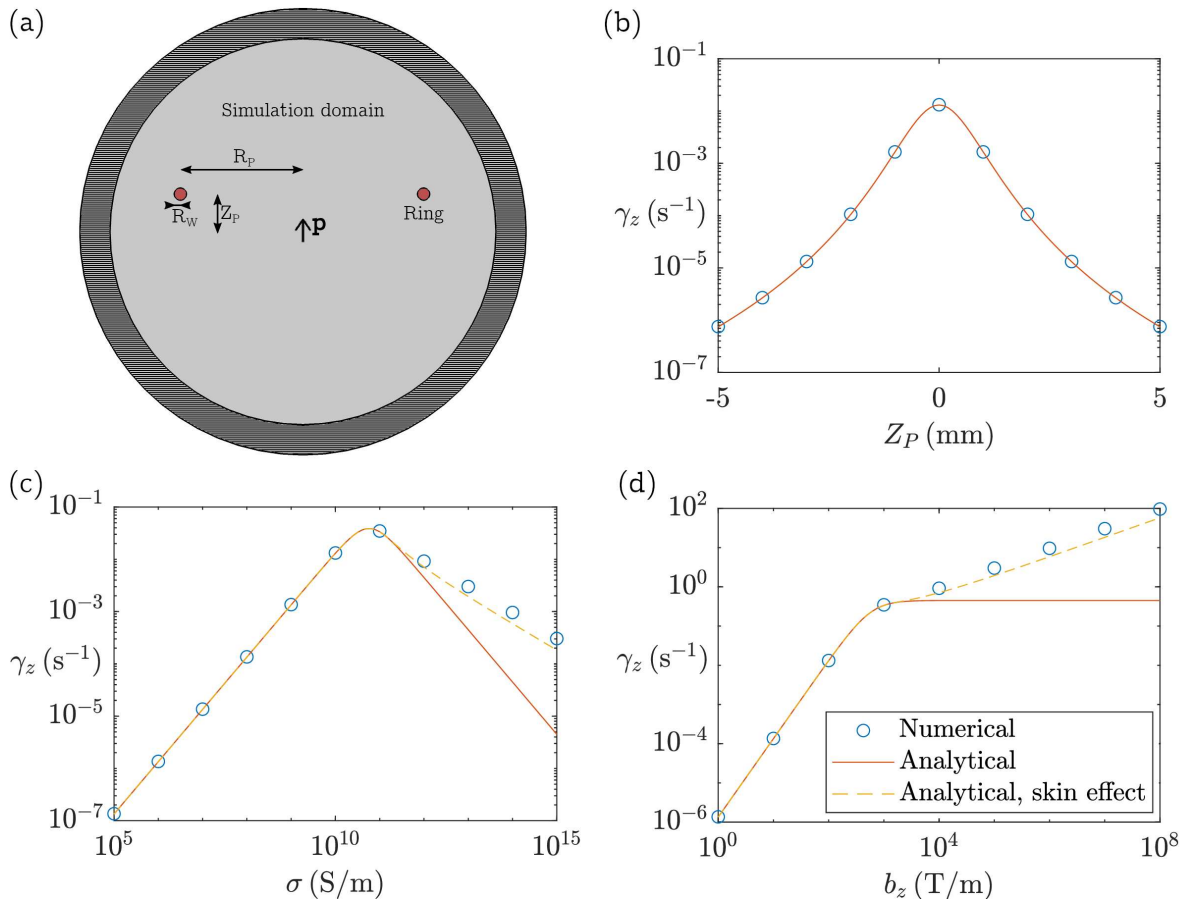


Figure 11: (a)Cross section of the numerical simulation setup. In the simulation domain Maxwell's equations and Ohms law are solved in the frequency domain. In the outer (striped) layer of the simulation domain distances between the mesh elements are scaled (infinite element domain) to minimize effects of the finite size of the domain on the results. (b)Comparison of the numerical solution (circles) for a conducting ring to the analytical solution (solid line, Eq. 19) for different values of Z_P. The parameters used for this and subsequent simulations are, unless otherwise stated, $R = 50\,\mu\mathrm{m}$, $R_P = 1\,\mathrm{mm}$, $R_W = 0.1\,\mathrm{mm}$, $b_z = 100\,\mathrm{T/m}$, $\rho = 10\,900\,\mathrm{kg/m^3}$ and $\sigma = 1 \times 10^{10}\,\mathrm{S}$. (c)Comparison for different values of σ and $Z_P = 0\,\mathrm{m}$. As mentioned in the text, the damping exhibits a maximum when $\mathscr{R} = \omega_z L$. (d)Comparison for different values of b_z and $Z_P = 0\,\mathrm{m}$. Note that both the frequency and the coupling increase with b_z, which leads to the asymptotically flat behavior for large b_z (for the analytical solution). The discrepancies between the numerical and analytical values in (c,d) at higher conductivities resp. gradients are due to the skin effect; the main difference is a higher effective resistance that is not accounted for by Eq. 22. By applying a very simple model to approximate this effect (using the resistance of a tube with the wall width set to the skin depth $\sqrt{\frac{2}{\mu_0 \omega_z \sigma}}$ as the effective resistance) we already achieve a good agreement between the modified analytical (dashed lines) and numerical values.

As a sanity check, we can use the simulations to calculate the power dissipated in a thin conducting ring and compare the result to Eq. 19. Fig. 11 show a simulation where a ring with radius R_P and a wire radius of R_W is located coaxial with the z-axis. The oscillating field is produced by a point dipole with the dipole moment (cf. Eq. 10)

$$\mathbf{p} = \frac{2\pi}{\mu_0} b_z R^3 \sin(\omega_z t) .$$

Here we have not included the quadrupole moment as we consider the case where the conductors are far away from the oscillating sphere (compared to the sphere radius). This is the relevant case for our experiments, where a micrometer-sized sphere levitates several millimeters away from the nearest surface. Note, however, that this underestimates the damping if any conductors are placed near the particle. The inductance of the ring is given by [Jac99]

$$L = \mu_0 R_P \left(\ln\left(8 \frac{R_P}{R_W} \right) - \frac{7}{4} \right) \tag{21}$$

and its resistance is

$$\mathscr{R} = 2R_P/(\sigma R_W^2), \tag{22}$$

where σ is the conductivity of the material of the wire. These formulas do not capture changes to the inductance and resistance due to the skin effect, since these become relevant only at conductivities and/or frequencies much higher than those used in our experiments, cf. Fig. 11. We plot the resulting damping term γ_z for various parameters in Fig. 11b-d and compare the analytical and numerical results, which agree well with each other.

3.5.3 Limitations to the quality factor

We can now use the simulation described above to evaluate eddy current damping in arbitrary conductors. As an example we consider a large conducting disk, as depicted in Fig. 12a. I assume the same values as for the simulations in the last section (cf. Fig. 11), in particular $R = 50\,\mu\text{m}$, $\rho = 10\,900\,\text{kg/m}^3$ and $b_z = 100\,\text{T/m}$, corresponding to a frequency of $f_z \approx 167 Hz$ (close to typical experimental values). I also use the cryogenic electrical conductivity of copper ($\sigma \approx 1 \times 10^{10}\,\text{S/m}$; depending on its purity the cryogenic conductivity of copper can range from approx. $1 \times 10^8\,\text{S/m}$ to approx. $1 \times 10^{12}\,\text{S/m}$ [SDR92]) for Fig. 12b,d and highlight both the conductivities of copper and stainless steel ($\sigma \approx 2 \times 10^6\,\text{S/m}$ [CCW70]) in Fig. 12c.

The main takeaway of this section is that eddy current damping can be a large source of dissipation for magnetic levitation if conductors are close (within several millimeters of the levitated particle). Also, note that for the frequencies considered here, high conductivity materials (e.g. copper) are usually worse w.r.t. damping than low conductivity materials (e.g. stainless steel). In the experiment presented in [HGH+23] we removed all normal conducting material from the vicinity of the trap (tens of centimeters) and thus made eddy current damping negligible.

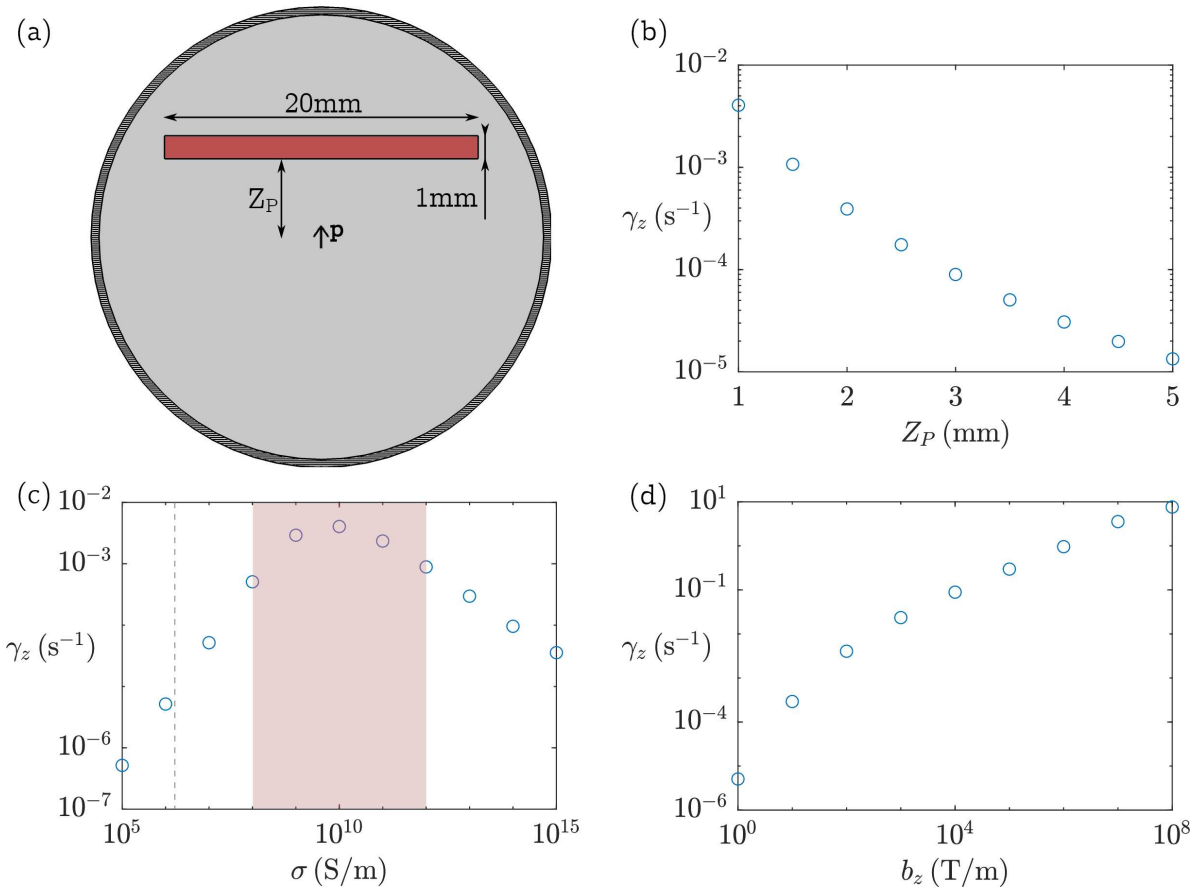


Figure 12: (a)Cross section of the numerical simulation setup. The red area corresponds to the disk shaped conductor with a diameter of 20 mm and a height of 1 mm. (b-d)Damping as a function of distance (b), conductivity (c) and gradient (d). For (c,d) $Z_P = 1$ mm, the other parameters are the same as in Fig. 11. The red shaded area in (c) corresponds to typical cryogenic conductivities of copper, while the dashed line corresponds to a typical conductivity of stainless steel.

4 Analytic solutions to the Maxwell–London equations and levitation force for a superconducting sphere in a quadrupole field

A precise knowledge of the magnetic field distribution around the superconducting levitator is critical to accurately predict the properties of the magnetic trap: Force and torque are derived from the field on the surface of the superconductor, and the flux in a given area (such as a SQUID loop) determines the magnetomechanical coupling strength.

The initial proposal for the levitation of a superconducting sphere in a quadrupole field [RICN+12] circumvented the problem of finding the field distribution by treating the sphere as a point dipole and assigning it an equivalent dipole moment based on the value of the applied field at the c.o.m. of the sphere. The procedure to arrive at the dipole moment is straightforward [RICN+12]: One treats the superconductor as a perfect diamagnet, assumes an uniform magnetization and assumes that the demagnetization factor (i.e. the proportionality factor between the magnetization and the demagnetizing field) is the same as it is for a perfectly diamagnetic sphere in a uniform field. This results in the dipole moment

$$\mathbf{p}(\mathbf{x_0}) = \frac{3V}{2\mu_0}\mathbf{B_0}(\mathbf{x_0}).$$

Comparing this to the dipole component of the induced field (cf. Eq. 10), we see that the expressions agree when the penetration depth is negligible. This approach does not account for the quadrupole component of the induced field. However, because the integral over the quadrupole component evaluates to zero in the integral expression for the force (Eq. 11), one still obtains the correct expression for the force. At the same time, other trap properties such as the coupling strengths to a measurement device or dissipation due to eddy current damping depend on the full field including the quadrupole component and cannot be evaluated using only the dipole component of the field (the dipole component will, however, provide a good approximation if the pickup loop or the conductors are located far away from the particle).

It is thus important to be aware that the approach from [RICN+12] is heuristic and does not, in general, result in correct expressions for the properties of the magnetic trap. Also, while it can provide a good approximation for a sphere in a quadrupole field in many cases, it does not work at all for other trapping fields or non-spherical superconductors.

For these reasons I considered it important to find the correct field distribution around a sphere in a quadrupole field and finding an approach that could be generalized to non-spherical superconductors and different trapping fields.

In the following manuscript I derive the magnetic field distribution around a superconducting sphere with arbitrary penetration depth in a quadrupole field by solving the Maxwell-London equations. I then derive the force acting on the sphere as well as the maximum surface field. I also present a case study for solid lead spheres and show that levitation is possible for sphere radii ranging from approximately 10 nm up to 1 cm.

The procedure to derive the field distribution can be generalized to different trapping fields. It is also possible to generalize it to find an analytical solution for some non-spherical superconductors such as dumbbells, and, by using the same approach with numerical techniques, one can find the field distribution for an arbitrary geometry of the superconductor.

Analytic solutions to the Maxwell-London equations and levitation force for a superconducting sphere in a quadrupole field

J Hofer and M Aspelmeyer

Vienna Center for Quantum Science and Technology (VCQ), Faculty of Physics, University of Vienna, Boltzmanngasse 5, Vienna A-1090, Austria

This is the author's accepted version of this work. The definite version was published in *Physica Scripta* "Analytic solutions to the Maxwell–London equations and levitation force for a superconducting sphere in a quadrupole field" volume 94, number 12, DOI 10.1088/1402-4896/ab0c44.

Abstract

Recent proposals suggest using magnetically trapped superconducting spheres in the Meissner state to create low-loss mechanical oscillators with long coherence times. In these proposals the derivation of the force on the superconducting sphere and the coupling to the sphere typically relies on a vanishing penetration depth λ as well as a specific symmetry (i.e. restricting the position of the sphere to one axis) or heuristic methods (e.g. assigning an equivalent point magnetic dipole moment to the sphere). In this paper we analytically solve the Maxwell-London equations with appropriate boundary conditions for a superconducting sphere in a quadrupole field. The analytic solutions provide the full field distribution for arbitrary λ and for an arbitrary sphere position as well as the distribution of shielding currents within the sphere. We furthermore calculate the force acting on the sphere and the maximum field over the volume of the sphere. We show that for a certain range of λ the maximum field experienced by the superconducting sphere is actually lower than it is for a non-magnetic sphere.

4.1 Introduction

The last decade has seen significant progress in achieving quantum control over solid state mechanical devices [PvdZ12]. One key idea is to exploit the available toolbox of quantum optics in both the optical and microwave domain by coupling mechanical motion to optical cavities or superconducting circuits [AKM14, BM15]. Recent examples include the generation of non-classical states of motion [OHA+10, WLW+15, HRM+17] and even of quantum entanglement involving micro-mechanical systems [RWM+18, OKDP+18, MacWR+18, PTSL13]. Several proposals have suggested that quasi-static magnetic levitation of superconductors in the Meissner state allows to further increase both system size and coherence time in such experiments, thereby not only improving the system performance but also enabling access to a completely new parameter regime of macroscopic quantum physics [RICN+12, CBT12, PPCS+18]. The requirements on the magnetic traps are similar to those of atom traps [FZ07], as in both cases a minimum in the magnetic field norm is necessary for levitation. Several trap configurations, such as the Anti-Helmholtz setup suggested in [RICN+12], produce a (local) quadrupole field, i.e. a magnetic field of the form $\frac{1}{2}\, b_\mathrm{z}\, \{x,\, y,\, -2\, z\}$, where b_z denotes the magnetic gradient along the z-axis. Coupling to the motion of the sphere is facilitated by placing a pickup loop in the proximity of the sphere. The flux through the pickup loop then depends on the position of the sphere. A detailed knowledge of the magnetic field distribution for arbitrary sphere positions is essential for a good understanding of both the trap dynamics and the coupling strength. However, a full analysis of the magnetic field distribution of such a configuration has not been carried out yet. The proposals referenced above provide results only for vanishing penetration depth ($\lambda = 0$) and rely either on symmetry features, where the sphere is restricted to the z-axis or use heuristic methods such as approximating the sphere as a point dipole. The aim of this paper is to avoid these restrictions and provide analytic expressions for the magnetic field for arbitrary λ and arbitrary sphere positions.

In section 2 we derive the magnetic field and the supercurrent on the surface of the sphere for the special case $\lambda = 0$ by solving the Maxwell equation with the appropriate boundary condition; in section 3 we generalize these results for arbitrary λ by solving the Maxwell-London equations with the appropriate boundary condition.

In section 4 we derive the force acting on the sphere and the maximum field over the volume of the sphere when it is located at the origin of the quadrupole field. The latter is important because if the maximum field seen by the sphere surpasses a critical field B_{c1} (dependent on the material), the sphere will no longer be in the Meissner state.

Section 5 provides a brief summary and a discussion of the results.

In the appendix we apply our results to the specific case of a lead sphere and demonstrate the applicability of this work to experiments.

For mathematical simplicity we choose the coordinate system such that the superconducting sphere of radius R is at the origin and the center of the quadrupole field is displaced relative to the origin by $-\mathrm{d}\mathbf{x} = -\{\mathrm{d}x,\, \mathrm{d}y,\, \mathrm{d}z\}$. We use $\mathbf{x} = \{x,\, y,\, z\}$ for the position vector in Cartesian coordinates. As is conventionally done, we refer to the magnetic flux density $\mathbf{B}$ as the magnetic field. The applied quadrupole field thus takes the form

$$\mathbf{B}_0 = \frac{1}{2}\, b_\mathrm{z}\, \{x + \mathrm{d}x,\, y + \mathrm{d}y,\, -2\,(z + \mathrm{d}z)\}. \tag{23}$$

We will also use spherical coordinates $(r,\, \theta,\, \phi)$ and the corresponding basis vectors $\mathbf{e}_\mathrm{r},\, \mathbf{e}_\theta,\, \mathbf{e}_\phi$. Spherical harmonics $Y_n^m$are understood to have the normalization

$$Y_n^m = \sqrt{\frac{2n+1}{4\pi}\,\frac{(n-m)!}{(n+m)!}}\, P_n^m(\cos\theta)\, \exp(\mathrm{i}\phi),$$

where P_n^m stands for the associated Legendre polynomials [Jac99]. The vector potential and magnetic field inside the sphere are denoted by $\mathbf{A}_{\text{in}}$ and $\mathbf{B}_{\text{in}}$, respectively, while $\mathbf{B}_{\text{out}}$ is used for the field outside the sphere. There is no current outside the sphere, so we can use a scalar potential Φ such that $\mathbf{B}_{\text{out}} = \mathbf{B}_0 - \nabla\Phi$. Since physical solutions for the induced field density $-\nabla\Phi$ vanish at infinity, it follows from $\Delta\Phi = 0$ that

$$\Phi = \sum_{n=0}^{\infty} r^{-(n+1)} \sum_{m=-n}^{n} a_{n,m}\, Y_n^m, \tag{24}$$

where the coefficients $a_{n,m}$ will be detemathrmined below. Components of a vector will be denoted by a superscript rather than a subscript, e.g. $\mathbf{B}_{\text{in}}^{\text{r}} = \mathbf{B}_{\text{in}} \cdot \mathbf{e}_{\text{r}}$. We will use the Coulomb gauge $\nabla\mathbf{A} = 0$ for any vector potential $\mathbf{A}$ throughout this paper.

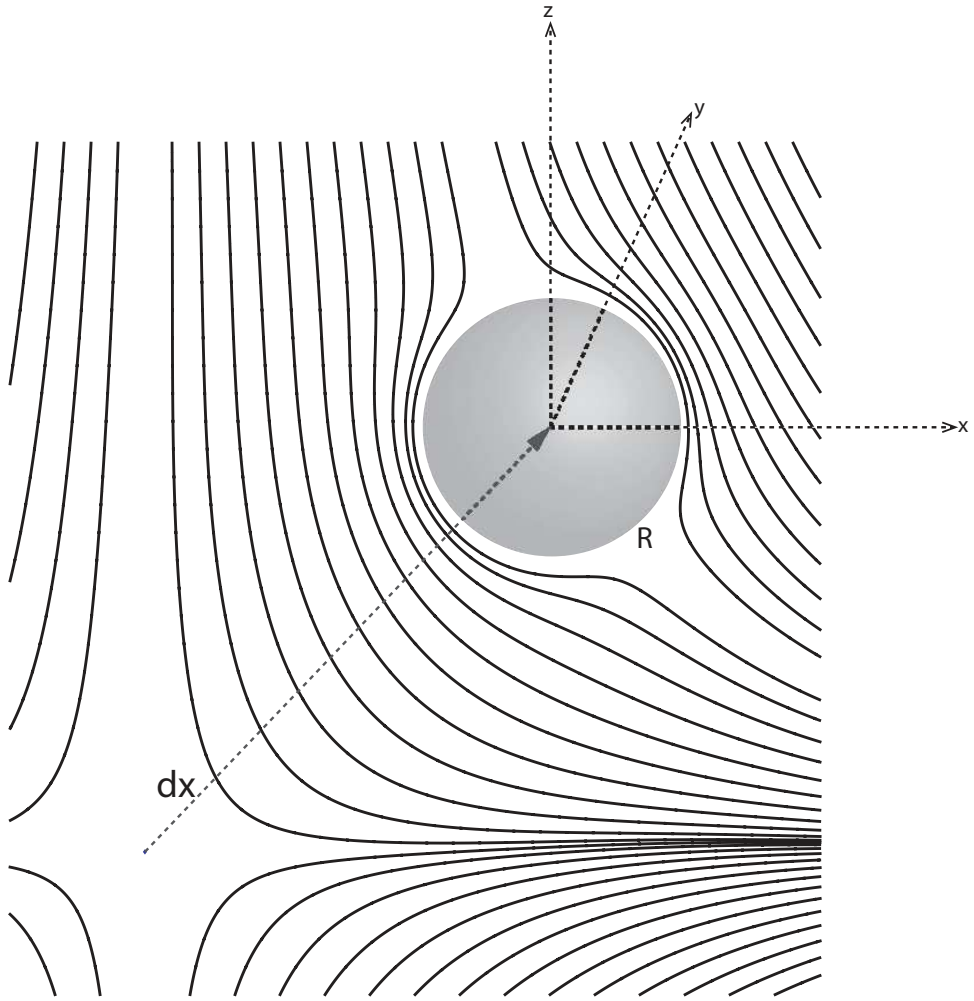


Figure 13: Sketch of the geometry. The superconducting sphere, located at the origin of the coordinate system, is displaced from the center of the quadrupole field by $\mathrm{d}\mathbf{x} = \{\mathrm{d}x, \mathrm{d}y, \mathrm{d}z\}$. The field is depicted by its streamlines in the xz-plane.

4.2 Magnetic field for $\lambda = 0$

For vanishing penetration depth there is no magnetic field inside the superconductor and the normal component of the magnetic field vanishes at the surface of the superconductor [Tin96], which in our case corresponds to

$$\mathbf{B}_{\text{in}} = 0, \;\; \mathbf{B}_{\text{out}}^{\text{r}}|_{r=R} = 0. \tag{25}$$

It follows from (23) and (24) that the radial part of the applied field and the induced field are given by

$$\begin{aligned}\mathbf{B}_0^{\mathrm{r}} = b_z\big(&- \sqrt{4\pi/3}\,\mathrm{d}z\,Y_1^0 + \sqrt{\pi/6}\,(\mathrm{i}\,\mathrm{d}y + \mathrm{d}x)\,Y_1^{-1} \\ &+ \sqrt{\pi/6}\,(\mathrm{i}\,\mathrm{d}y - \mathrm{d}x)\,Y_1^1 - \sqrt{4\pi/5}\,r\,Y_2^0\,\big),\end{aligned}$$

and

$$(-\nabla\Phi)^{\mathrm{r}} = \sum_{n=0}^{\infty}(n+1)\,r^{-(n+2)}\sum_{m=-n}^{n} a_{n,m}\,Y_n^m,$$

respectively. The boundary condition (25) then readily yields the coefficients as

$$\begin{aligned} a_{1,0} &= b_z\,\sqrt{\pi/3}\,R^3\,\mathrm{d}z, \\ a_{1,-1} &= -b_z\,\sqrt{\pi/24}\,R^3\,(\mathrm{d}x + \mathrm{i}\,\mathrm{d}y), \\ a_{1,1} &= b_z\,\sqrt{\pi/24}\,R^3\,(\mathrm{d}x - \mathrm{i}\,\mathrm{d}y), \\ a_{2,0} &= b_z\,\sqrt{4\pi/45}\,R^5, \end{aligned} \tag{26}$$

all other coefficients being zero. We also introduce normalized quantities by measuring length in units of R and the magnetic field in units of $b_z R$, i.e.

$$\tilde{\mathbf{x}} = \mathbf{x}/R,\ \mathrm{d}\tilde{\mathbf{x}} = \mathrm{d}\mathbf{x}/R,\ \tilde{\mathbf{B}}(\tilde{\mathbf{x}}) = \mathbf{B}(\tilde{\mathbf{x}}R)/(b_z R).$$

Selected normalized field components are plotted in figure 14. As the field is zero inside the sphere and there is by definition no current outside the sphere, the supercurrent density $\mathbf{K}$ vanishes everywhere except on the surface of the sphere and is related to the transverse magnetic field by

$$\mathbf{K}^\theta = -\mathbf{B}^{\Phi}_{\mathrm{out}}|_{r=R}/\mu_0,\ \ \mathbf{K}^\phi = \mathbf{B}^{\theta}_{\mathrm{out}}|_{r=R}/\mu_0,$$

where μ_0 denotes the vacuum permeability. The normalized supercurrent distribution

$$\tilde{\mathbf{K}}(\theta,\phi) = \mu_0\mathbf{K}(\theta,\phi)/(b_z R)$$

is thus obtained as

$$\begin{aligned} \tilde{\mathbf{K}}^\theta &= \frac{3}{4}(\mathrm{d}\tilde{x}\,\sin\phi - \mathrm{d}\tilde{y}\,\cos\phi), \\ \tilde{\mathbf{K}}^\phi &= \frac{3}{4}\cos\theta\,(\mathrm{d}\tilde{x}\,\cos\phi + \mathrm{d}\tilde{y}\,\sin\phi) + \frac{3}{2}\,\mathrm{d}\tilde{z}\,\sin\theta + \frac{5}{4}\sin(2\theta). \end{aligned} \tag{27}$$

4.3 Magnetic field for finite λ

For finite λ the magnetic field inside the sphere is finite and determined by the London equation, i.e.

$$\Delta\mathbf{A}_{\mathrm{in}} = 1/\lambda^2\mathbf{A}_{\mathrm{in}},\ \mathbf{B}_{\mathrm{in}} = \nabla\times\mathbf{A}_{\mathrm{in}}. \tag{28}$$

The boundary condition that takes the place of (25) is simply

$$\mathbf{B}_{\mathrm{in}}|_{r=R} = \mathbf{B}_{\mathrm{out}}|_{r=R}. \tag{29}$$

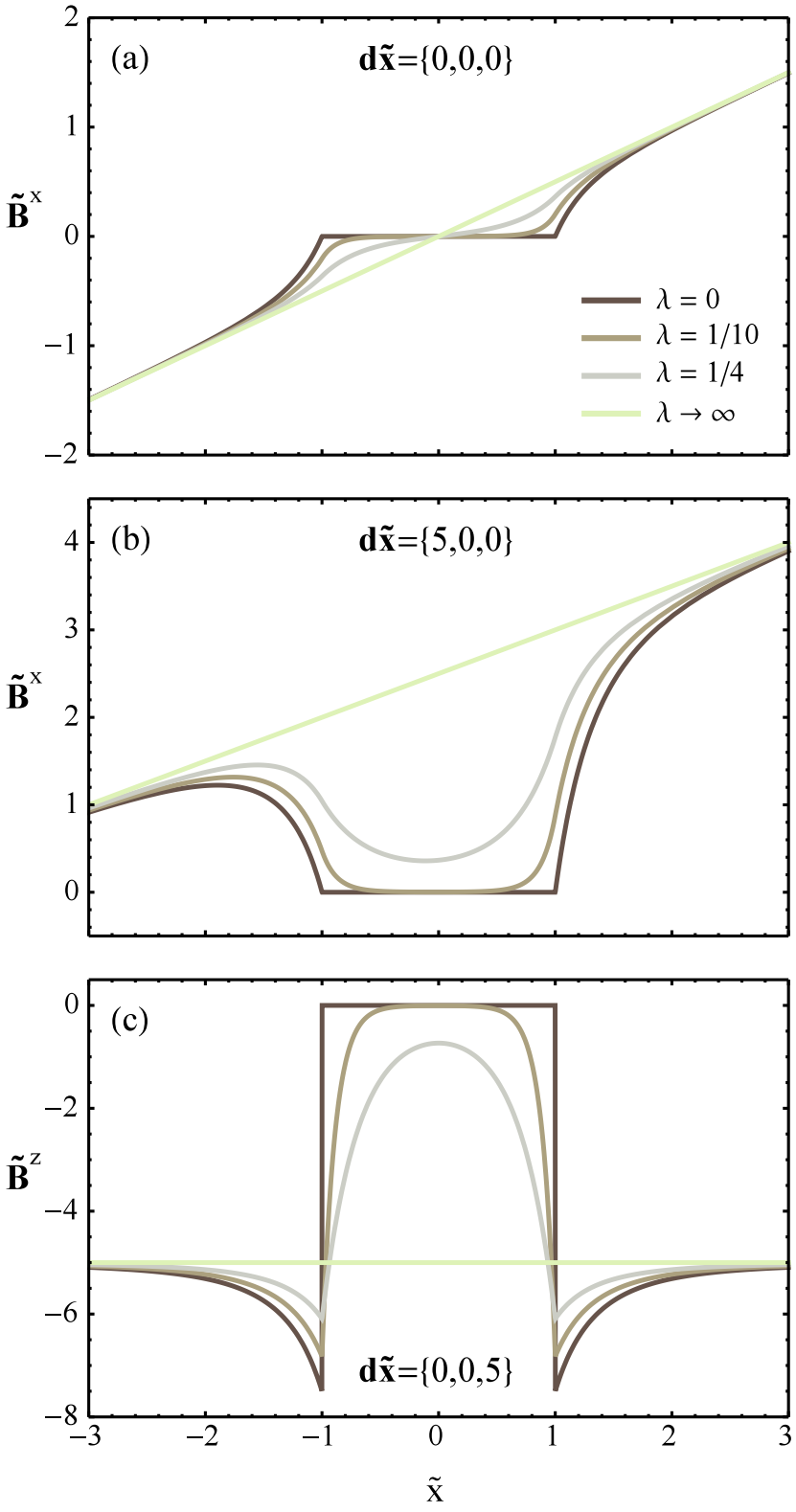


Figure 14: Plot of normal and transverse magnetic field along the normalized x-axis for various penetration depths and sphere displacements. (a)Plot of normal magnetic field for $d\tilde{\mathbf{x}} = \{0, 0, 0\}$. (b)Plot of normal magnetic field for $d\tilde{\mathbf{x}} = \{5, 0, 0\}$. (c)Plot of transverse magnetic field for $d\tilde{\mathbf{x}} = \{0, 0, 5\}$. The legend printed in panel (a) is valid for all panels.

To find the solution we first introduce the vector spherical harmonics [BEG85]

$$\mathbf{Y}_n^m = Y_n^m \, \mathbf{e}_\mathrm{r}, \quad \mathbf{\Psi}_n^m = r \, \nabla Y_n^m, \quad \mathbf{\Phi}_n^m = \mathbf{e}_\mathrm{r} \times \mathbf{\Psi}_n^m$$

and make the ansatz

$$\mathbf{A}_{\text{in}} = \sum_{n=0}^{\infty} \sum_{m=-n}^{n} C_{n,m}(r)\, \mathbf{\Phi}_n^m(\theta,\phi).$$

Note that if a solution of this form with continuously differentiable $C_{n,m}(r)$ exists, then

$$\nabla\big(C_{n,m}(r)\, \mathbf{\Phi}_n^m(\theta,\phi)\big) = 0$$

and the Coulomb gauge condition is fulfilled. The London equation (28) leads to

$$r\, \partial_r^2\big(rC_{n,m}\big) - \big(r^2/\lambda^2 + n(n+1)\big)C_{n,m} = 0,$$

which is the modified spherical Bessel equation. The only solution (convergent at the origin) for the inside vector potential is therefore given by

$$\mathbf{A}_{\text{in}} = \sum_{n=0}^{\infty} i_n(\frac{r}{\lambda}) \sum_{m=-n}^{n} c_{n,m}\, \mathbf{\Phi}_n^m(\theta,\phi),$$

where the i_n are first order modified spherical Bessel functions [AS64] and the coefficients $c_{n,m}$ are yet to be determined. The fields can be expressed in vector spherical harmonics as

$$\begin{aligned}\mathbf{B}_{\text{in}} = -\frac{1}{r} \sum_{n=0}^{\infty} \sum_{m=-n}^{n} c_{n,m} \big[& n(n+1)\, i_n(\frac{r}{\lambda})\, \mathbf{Y}_n^m \\ & + \partial_r\big(r\, i_n(\frac{r}{\lambda})\big)\, \mathbf{\Psi}_n^m\big],\end{aligned} \tag{30}$$

$$\mathbf{B}_{\text{out}} = \mathbf{B}_0 + \sum_{n=0}^{\infty} r^{-(n+2)} \sum_{m=-n}^{n} a'_{n,m}\big((n+1)\, \mathbf{Y}_n^m - \mathbf{\Psi}_n^m\big),$$

$$\begin{aligned}\mathbf{B}_0 = b_z \big[& - \sqrt{4\pi/3}\, \mathrm{d}z\, (\mathbf{Y}_1^0 + \mathbf{\Psi}_1^0) \\ & + \sqrt{\pi/6}\, (\mathrm{d}x + \mathrm{i}\, \mathrm{d}y)\, (\mathbf{Y}_1^{-1} + \mathbf{\Psi}_1^{-1}) \\ & - \sqrt{\pi/6}\, (\mathrm{d}x - \mathrm{i}\, \mathrm{d}y)\, (\mathbf{Y}_1^1 + \mathbf{\Psi}_1^1) \\ & - \sqrt{\pi/5}\, r\, (2\, \mathbf{Y}_2^0 + \mathbf{\Psi}_2^0)\big].\end{aligned}$$

The boundary condition (29) then determines the coefficients as

$$\begin{aligned} a'_{1,m} &= f_1(\frac{\lambda}{R})\, a_{1,m}, \\ a'_{2,0} &= f_2(\frac{\lambda}{R})\, a_{2,0}, \\ c_{1,m} &= (3\,\lambda)/\big(R^3\, i_2(\frac{R}{\lambda})\big)\, a'_{1,m}, \\ c_{2,0} &= \big(5\,\lambda\big)/\big(2\, R^4\, i_3(\frac{R}{\lambda})\big)\, a'_{2,0}, \end{aligned}$$

with

$$\begin{aligned} f_1(\frac{\lambda}{R}) &= 1 - 3\,\frac{\lambda}{R}(\coth\frac{R}{\lambda} - \frac{\lambda}{R}), \\ f_2(\frac{\lambda}{R}) &= 1 - 5\,\frac{\lambda}{R}\big((\coth\frac{R}{\lambda} - \frac{\lambda}{R})^{-1} - 3\,\frac{\lambda}{R}\big). \end{aligned}$$

Here the $a'_{n,m}$ denote the coefficients of the scalar potential for finite λ, while the $a_{n,m}$ still refer to the coefficients for $\lambda = 0$ as given in (26). Note that $a'_{n,m}$ is related to $a_{n,m}$ by a scaling function that depends only on the ratio λ/R. For $\lambda/R \to 0$ we get $a'_{n,m} \to a_{n,m}$ and $c_{n,m} \to 0$ and the solution for finite λ thus converges to the solution for $\lambda = 0$ determined in the last section. Normalized field components are plotted in figure 14, the scaling functions are plotted in figure 15. The supercurrent distribution $\mathbf{j}$ inside the sphere can now be simply obtained from the London equation (28) and $\nabla \times \mathbf{B}_{\text{in}} = \mu_0 \mathbf{j}$ as $\mathbf{j} = -\frac{1}{\mu_0 \lambda^2} \mathbf{A}_{\text{in}}$.

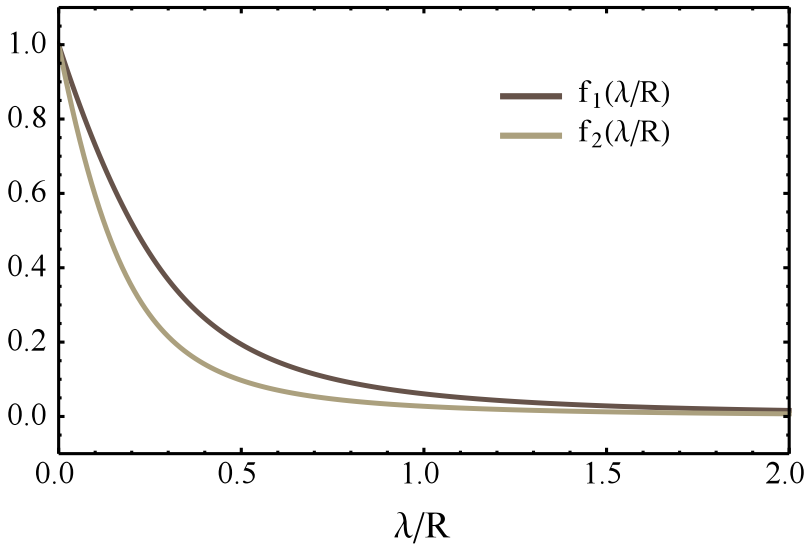


Figure 15: Plot of the scaling functions f_1 and f_2. As shown in the next paragraph, the force on the sphere scales as f_1 with increasing λ/R.

4.4 Levitation force and maximum field

The force on the sphere can be written in terms of the magnetic field on the surface of the sphere as

$$\mathbf{F} = \frac{R^2}{\mu_0} \int_0^{\pi} \mathrm{d}\theta \int_0^{2\pi} \mathrm{d}\phi \, \sin\theta \left[(\mathbf{e}_{\mathrm{r}} \mathbf{B}) \mathbf{B} - \frac{1}{2} \mathbf{e}_{\mathrm{r}} \mathbf{B}^2 \right]_{r=R}.$$

Here $\mathbf{B}$ denotes either $\mathbf{B}_{\text{in}}$ or $\mathbf{B}_{\text{out}}$, as they coincide on the surface of the sphere. Carrying out the integration we find

$$F_z = -\frac{3V}{2\mu_0} b_z^2 \, f_1(\frac{\lambda}{R}) \, \mathrm{d}z, \quad \frac{1}{\mathrm{d}x} F_x = \frac{1}{\mathrm{d}y} F_y = \frac{1}{4\,\mathrm{d}z} F_z, \tag{31}$$

where $V = \frac{4\pi}{3} R^3$ is the volume of the sphere. For $\lambda \to 0$ we have $f_1(\frac{\lambda}{R}) \to 1$ and we recover the expressions given in [RICN+12].

We now determine the maximum field strength $B_{\max} = \max(\sqrt{\mathbf{B}_{\text{in}}^2})$, where the maximum is evaluated over the volume of the sphere, for $\mathrm{d}\mathbf{x} = 0$. In this case the squared magnetic field inside the sphere reduces to

$$\begin{aligned} \mathbf{B}_{\text{in}}^2 =& (45\, c_{2,0}^2)/(4\pi r^2) \big[(3\cos^2\theta - 1)^2 \, i_2^2(\frac{r}{\lambda}) \\ &+ \cos^2\theta \, \sin^2\theta \, \big(\frac{r}{\lambda} i_3(\frac{r}{\lambda}) + 3\, i_2(\frac{r}{\lambda}) \big)^2 \big]. \end{aligned}$$

Evaluating the partial derivatives with respect to r and θ it follows that $\partial_r \vec{B}_{\text{in}}^2 \geq 0 \; \forall (r, \theta)$, i.e. the maximum lies on the surface of the sphere, and that the maximum occurs for $\theta = \theta_{\max}$ with $\theta_{\max}$ determined by

$$\cos^2 \theta_{\max} = \frac{\left(\frac{R}{\lambda} i_3(\frac{R}{\lambda})/i_2(\frac{R}{\lambda}) - 3\right)^2 - 6}{2\left(\left(\frac{R}{\lambda} i_3(\frac{R}{\lambda})/i_2(\frac{R}{\lambda}) - 3\right)^2 - 9\right)} \tag{32}$$

for $\lambda/R \lesssim 0.54$ and $\theta_{\max} \in \{0, \pi\}$ otherwise. We then get $B_{\max} = |\mathbf{B}_{\text{in}}(R, \theta_{\max})|$. Note that the expression on the right hand side of (32) converges to $\frac{1}{2}$ for $\lambda/R \to 0$, which corresponds to $\theta_{\max} \to \frac{\pi}{2} \pm \frac{\pi}{4}$ and

$$B_{\max} \to \frac{5}{4} b_z R \tag{33}$$

(this result can of course also directly be read off equation (27) derived in section 2 for $\lambda = 0$). On the other hand, for $\lambda/R \to \infty$, i.e. a non-magnetic sphere, we simply have $\theta_{\max} \in \{0, \pi\}$ and $B_{\max} \to b_z R$. In figure 16 we plot $\theta_{\max}$ as well as $\tilde{B}_{\max}$ against the ratio λ/R. It is interesting to note that for $\lambda/R \gtrsim 0.14$ the maximum field strength is smaller than $b_z R$, i.e. in that range $B_{\max}$ is actually smaller for a superconducting sphere than it would be for a non-magnetic sphere. This result is counter-intuitive at first glance and in stark contrast to the case of a superconducting sphere in a homogeneous field [Mat99] $\mathbf{B}_{\text{hom}}$, where the maximum field strength for any value of λ/R will always be higher than $|\mathbf{B}_{\text{hom}}|$. One can understand this behavior qualitatively by looking at the absolute fields at $\theta = 0$ and $\theta = \frac{\pi}{4}$ for increasing values of λ/R. In the former case we have $|\mathbf{B}_{\text{in}}(R, 0, \phi)|_{\lambda=0} = 0$ monotonically increasing to $|\mathbf{B}_{\text{in}}(R, 0, \phi)|_{\lambda\to\infty} \to b_z R$, while in the latter case we have $|\mathbf{B}_{\text{in}}(R, \pi/4, \phi)|_{\lambda=0} = \frac{5}{4} b_z R$ monotonically decreasing to $|\mathbf{B}_{\text{in}}(R, \pi/4, \phi)|_{\lambda\to\infty} \to \sqrt{\frac{5}{8}} b_z R$. Thus, when $\theta_{\max}$ shifts towards $\theta = 0$ with increasing λ/R we will, at some point, have $|\mathbf{B}_{\text{in}}(R, \theta_{\max}, \phi)| < b_z R$. Analytic solutions for the maximum field strength for $|\mathrm{d}\mathbf{x}| > 0$ can be found as well, but the resulting expressions are bulky and do not serve to further enhance understanding of the physics. For anyone interested in these results we recommend starting with (30) and using a computer algebra system to derive the expressions for the maximum.

4.5 Summary and discussion

In the previous sections we have derived analytical solutions for the magnetic field distribution for a superconducting sphere in the Meissner state placed in an applied quadrupole field by analytically solving the Maxwell-London equations with appropriate boundary conditions. The solutions are obtained by expanding the fields in terms of vector spherical harmonics. We then derived the force acting on the sphere. The results are valid as long as the maximum field strength on the surface of the sphere is below a critical field strength B_{c1}, the exact value of which depends on the superconducting material. Above B_{c1} the superconductor will enter an intermediate state (type-I) or mixed state (type-II) [Tin96], respectively, and the analysis provided here can no longer be applied. We also calculated the maximum field strength seen by the superconducting sphere when it is located at the center of the quadrupole field, and demonstrated that for a certain range of λ/R the maximum field strength is lower than it is for a non-magnetic sphere.

We expect these results to be applied in the context of quasi-static magnetic traps for superconductors and to greatly enhance understanding of these traps. From the analytic solutions for the force and the field distribution one can directly obtain analytic results for trapping frequencies and coupling strengths. Previous analysis was limited to spheres that are large compared to their penetration depth ($\lambda/R \to 0$), while our results are valid

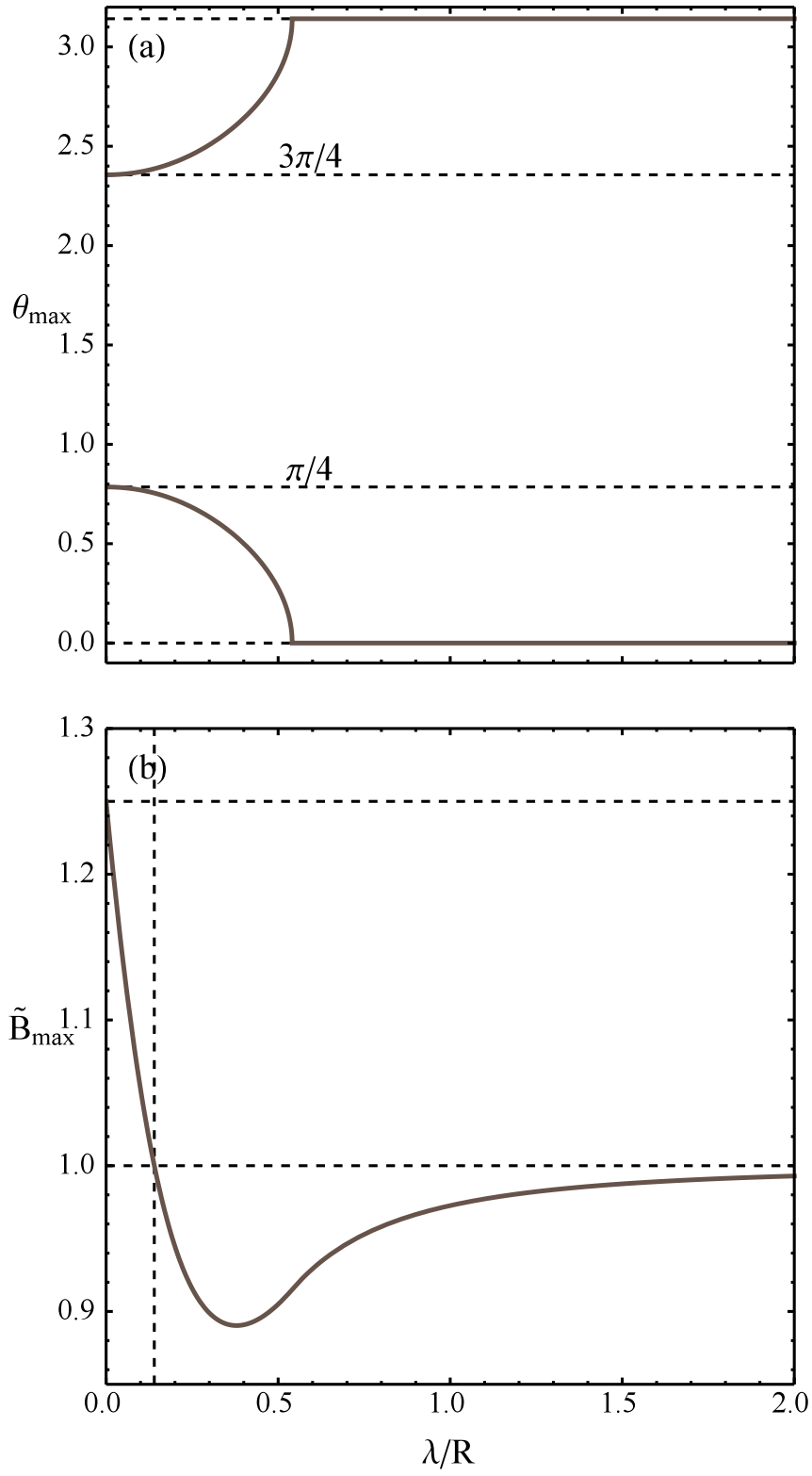


Figure 16: (a)Plot of the double-valued angle for which the field strength is at a maximum. (b)Plot of the normalized maximum field strength $\tilde{B}_{\max}$. The dashed lines are guides to the eye.

for arbitrarily sized spheres. Our results furthermore show a way to connect dynamical parameters of the magnetic trap (e.g. frequency) to material constants (e.g penetration depth), opening up new ways to measure these quantities.

The solution can easily be extended to magnetic fields of various forms, as long as they

possess an expansion in vector spherical harmonics.

Acknowledgements

The authors are grateful for discussions with A. Sanchez and his group. This work was supported by the European Union's Horizon 2020 research and innovation programme under grant agreement No 736943 (MaQSens), the European Research Council (ERC CoG QLev4G), and the Austrian Science Fund (FWF) under project F40 (SFB FOQUS).

4.6 References

These are the references cited in the author's version of the manuscript.

[AKM14] Markus Aspelmeyer, Tobias J. Kippenberg, and Florian Marquardt. Cavity optomechanics. *Rev. Mod. Phys.*, 86:1391–1452, 2014.

[AS64] Milton Abramowitz and Irene A. Stegun. *Handbook of Mathematical Functions with Formulas, Graphs, and Mathematical Tables*. Dover, 1964.

[BBR+09] S. Becker, M. Bussmann, S. Raith, M. Fuchs, R. Weingartner, P. Kunz, W. Lauth, U. Schramm, M. El Ghazaly, F. Grüner, H. Backe, and D. Habs. Characterization and tuning of ultrahigh gradient permanent magnet quadrupoles. *Phys. Rev. ST Accel. Beams*, 12:102801, Oct 2009.

[BEG85] R G Barrera, G A Estevez, and J Giraldo. Vector spherical harmonics and their application to magnetostatics. *European Journal of Physics*, 6(4):287, 1985.

[BM15] Warwick P. Bowen and Gerard J. Milburn. *Quantum Optomechanics*. CRC Press, 2015.

[CBT12] M. Cirio, G. K. Brennen, and J. Twamley. Quantum magnetomechanics: Ultrahigh-q-levitated mechanical oscillators. *Phys. Rev. Lett.*, 109:147206, Oct 2012.

[FZ07] József Fortágh and Claus Zimmermann. Magnetic microtraps for ultracold atoms. *Rev. Mod. Phys.*, 79:235–289, 2007.

[HRM+17] Sungkun Hong, Ralf Riedinger, Igor Marinković, Andreas Wallucks, Sebastian G. Hofer, Richard A. Norte, Markus Aspelmeyer, and Simon Gröblacher. Hanbury brown and twiss interferometry of single phonons from an optomechanical resonator. *Science*, 358(6360):203–206, 2017.

[Jac99] John David Jackson. *Classical electrodynamics*. Wiley, 3rd ed. edition, 1999.

[MacWR+18] Igor Marinković, Andreas Wallucks, Ralf Riedinger, Sungkun Hong, Markus Aspelmeyer, and Simon Gröblacher. Optomechanical bell test. *Phys. Rev. Lett.*, 121:220404, 2018.

[Mat99] Ernesto A. Matute. On the superconducting sphere in an external magnetic field. *American Journal of Physics*, 67(9):786–788, 1999.

[OHA+10] A. D. O'Connell, M. Hofheinz, M. Ansmann, Radoslaw C. Bialczak, M. Lenander, Erik Lucero, M. Neeley, D. Sank, H. Wang, M. Weides, J. Wenner, John M. Martinis, and A. N. Cleland. Quantum ground state and single-phonon control of a mechanical resonator. *Nature*, 464:697, Mar 2010.

[OKDP+18] C. F. Ockeloen-Korppi, E. Damskägg, J.-M. Pirkkalainen, M. Asjad, A. A. Clerk, F. Massel, M. J. Woolley, and M. A. Sillanpää. Stabilized entanglement of massive mechanical oscillators. *Nature*, 556(7702):478–482, 2018.

[PPCS+18] H Pino, J Prat-Camps, K Sinha, B Prasanna Venkatesh, and O Romero-Isart. On-chip quantum interference of a superconducting microsphere. *Quantum Science and Technology*, 3(2):025001, 2018.

[PTSL13] T. A. Palomaki, J. D. Teufel, R. W. Simmonds, and K. W. Lehnert. Entangling mechanical motion with microwave fields. *Science*, 342(6159):710–713, 2013.

[PvdZ12] Menno Poot and Herre S.J. van der Zant. Mechanical systems in the quantum regime. *Physics Reports*, 511(5):273 – 335, 2012.

[RICN+12] O. Romero-Isart, L. Clemente, C. Navau, A. Sanchez, and J. I. Cirac. Quantum magnetomechanics with levitating superconducting microspheres. *Phys. Rev. Lett.*, 109:147205, 2012.

[RWM+18] Ralf Riedinger, Andreas Wallucks, Igor Marinkovic, Clemens Löschnauer, Markus Aspelmeyer, Sungkun Hong, and Simon Gröblacher. Remote quantum entanglement between two micromechanical oscillators. *Nature*, 556(7702):473–477, 2018.

[Str01] J. Strait. Very high gradient quadrupoles. *Proceedings of the 2001 Particle Accelerator Conference*, 1:176–180, 2001.

[Tin96] M. Tinkham. *Introduction to Superconductivity*. Dover Publications, 1996.

[WLW+15] E. E. Wollman, C. U. Lei, A. J. Weinstein, J. Suh, A. Kronwald, F. Marquardt, A. A. Clerk, and K. C. Schwab. Quantum squeezing of motion in a mechanical resonator. *Science*, 349(6251):952–955, 2015.

4.7 Appendix

To show the practicality of this analysis with regard to magnetic levitation, we consider a lead sphere with density $\rho = 11340 kg/m^3$ at millikelvin temperatures, s.t. the London penetration depth $\lambda \approx 30nm$ and the critical field $B_c \approx 80mT$. To successfully levitate the sphere we need the magnetic force (31) to counteract the gravitational force (which we take to act along the z-axis) $F_{grav} = \{0,\, 0\,, -V\,\rho\,g\}$, where $g \approx 10m/s^2$. This results in an equilibrium position of the sphere at $dz = -2\,\mu_0\,\rho\,g/\big(3\,b_z^2\,f_1(\frac{\lambda}{R})\big)$. Self-consistency requires that the maximum field over the sphere at this position is below B_c. As shown in figure 17, this condition is indeed fulfilled for a wide range of particle radii R and field gradients b_z. Quadrupole fields with gradients of up to $500T/m$ have already been demonstrated [BBR+09, Str01]. Specifically, taking $R = 1\mu m$ and $b_z = 500T/m$, the rest position of the sphere is $dz = -0.4\mu m$ and the maximum field strength on its surface is approximately $0.8mT$, two orders of magnitude below the critical field.

It is noteworthy that the minimum gradient $b_{z,min}$ that is necessary for levitation stays approximately constant over a wide range of radii, in this case $b_{z,min} \approx 1.78T/m$ for particle

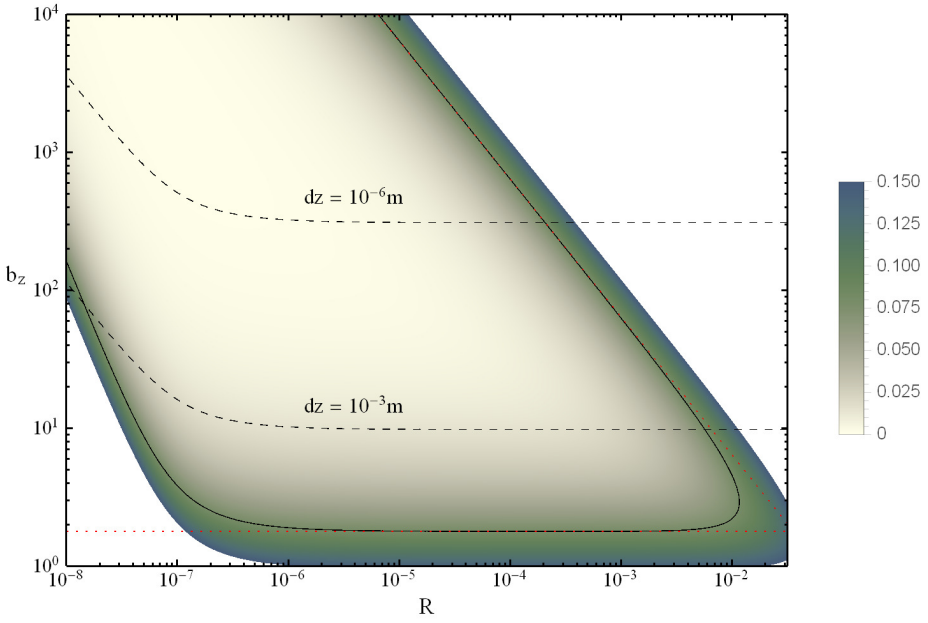


Figure 17: Plot of the maximum field strength on the surface of the sphere at its rest position in a gravitational field. The solid line corresponds to a field strength of $80mT$, while the dashed lines correspond to sphere displacements of $1\mu m$ resp. $1mm$. The dotted red lines are the limiting cases as described in the text. The units on the color bar are Tesla.

radii between approximately $1\mu m$ and $1mm$. This is due to the fact that for $\lambda \ll R \ll |dz|$ the maximum field on the particle surface is approximately given by $\frac{3}{2} b_z |dz| \approx \mu_0 \, \rho \, g \, b_z^{-1}$ and it follows that

$$b_{z,min} \approx \mu_0 \, \rho \, g \, B_c^{-1}.$$

For radii below $1\mu m$ one has to take into account the penetration depth, while for radii above $1mm$ one has to consider the radius of the sphere. For $|dz| \ll R$, the maximum radius R_{max} follows directly from (33) as

$$R_{max} \approx 4 \, B_c / (5 \, b_z).$$

These two limiting cases correspond to the red dotted lines in figure 17.

Our analysis does not predict a lower limit to the radius as long as one can produce a sufficiently high magnetic gradient, but the London equations(and therefore this analysis) are only valid for materials with dimensions well above the atomic length scale.

This analysis can easily be adapted to any specific superconductor and temperature, as long as the material parameters are known.

5 High-Q Magnetic Levitation and Control of Superconducting Microspheres at Millikelvin Temperatures

While the theoretical predictions regarding levitation of zero-field-cooled superconductors were promising [RICN+12], they had not yet been experimentally verified. Although zero-field-cooled superconducting (hollow) spheres are used for superconducting gravimeters [Goo99], the motion of the sphere in that case has a very low ($< 1\,\mathrm{Hz}$) resonance frequency and is strongly overdamped by design. A pioneering experiment showing the levitation of a superconducting lead particle in the magnetic field produced by an Anti-Helmholtz coil was performed in [vW16], however, here the quality factor was limited by the presence of ambient Helium gas. Our aim was to improve on this experiment by reducing dissipation as much as possible. In addition, we wanted to include and test all components necessary for preparing a magnetically levitated sphere in a quantum state, in particular (i)a measurement device that is capable of measuring the motion of the sphere close to the quantum limit, (ii)a feedback system that allows us to control and cool the motion of the sphere and (iii)vibration isolation and magnetic shielding to keep the contributions to the heating rate from non-thermal forces low. To achieve low dissipation, we used a cryogenic dilution refrigerator that does not rely on exchange gas to thermalize the components of the setup. The particle itself was initially lying on, and thus in thermal contact with, a surface close to the trap center. While levitating, it was kept cold by minimizing thermal radiation from the outside (through the windows) with appropriate optical wavelength filters. In this way we did not see a limitation of the levitation time. Additionally, to avoid resistive damping due to induced currents in nearby materials as described in the introductory sections, we took great care to avoid any conductors close to the trap. The position of the particle was measured with a superconducting flux transformer connected to a SQUID. To implement fast magnetic feedback, we processed the measured signal using a FPGA and fed it back to the levitated particle by means of a superconducting coil mounted approximately 1 mm below the trap center. We used superconducting shields to protect the particle from fluctuations of the magnetic background field in the laboratory and a self-built cryogenic vibration isolation system to attenuate environmental vibrations at the resonance frequency by seven orders of magnitude.

As a result, we report in this publication the levitation of superconducting spheres with quality factors of up to 2.6×10^7 for the c.o.m. motion, which, to the best of my knowledge, are the highest ones reported for any magnetic levitation experiment at the current date. We show feedback control of all c.o.m. degrees of freedom and, due to the excellent isolation from environmental noise, a steady-state motion of the particle below the measurement noise of $1\,\mathrm{nm}/\sqrt{\mathrm{Hz}}$. The quality factor appears to be limited by remanent trapped flux in the type-II superconducting sphere and is expected to increase in future experiments by either using a type-I superconductor as levitator or adding ferromagnetic shielding to protect the particle from magnetic fields when it is cooled below its transition temperature. The main limitations in this experiment remain the comparatively small coupling as well as fluctuations of the trap current. The former can be improved by optimizing the design and position of the pickup loop, while the latter can be improved by using a persistent-current trap. A careful analysis of the results shows that ground-state cooling of of a magnetically levitated superconductor is possible with the highlighted improvements.

High-Q Magnetic Levitation and Control of Superconducting Microspheres at Millikelvin Temperatures

J. Hofer[1,2], R. Gross[3,4,5], G. Higgins[2,6], H. Huebl[3,4,5], O. F. Kieler[7], R. Kleiner[8], D. Koelle[8], P. Schmidt[2], J. A. Slater[1], M. Trupke[1], K. Uhl[8], T. Weimann[7], W. Wieczorek[1,6], and M. Aspelmeyer[1,2]

[1]Faculty of Physics, Vienna Center for Quantum Science and Technology (VCQ), University of Vienna, A-1090 Vienna, Austria
[2]Institute for Quantum Optics and Quantum Information (IQOQI), Austrian Academy of Sciences, A-1090 Vienna, Austria
[3]Walther-Meißner-Institut, Bayerische Akademie der Wissenschaften, D-85748 Garching, Germany
[4]Physik-Department, Technische Universität München, D-85748 Garching, Germany
[5]Munich Center for Quantum Science and Technology (MCQST), D-80799 München, Germany
[6]Department of Microtechnology and Nanoscience (MC2), Chalmers University of Technology, S-412 96 Gothenburg, Sweden
[7]Physikalisch-Technische Bundesanstalt (PTB), D-38116 Braunschweig, Germany
[8]Physikalisches Institut, Center for Quantum Science (CQ) and LISA$^+$, University of Tuebingen, D-72076 Tuebingen, Germany

This is the author's accepted version of this work. The definite version was published in *Physical Review Letters* "High-Q Magnetic Levitation and Control of Superconducting Microspheres at Millikelvin Temperatures" volume 131, issue 4, DOI 10.1103/PhysRevLett.131.043603.

Abstract

We report the levitation of a superconducting lead-tin sphere with 100 µm diameter (corresponding to a mass of 5.6 µg) in a static magnetic trap formed by two coils in an anti-Helmholtz configuration, with adjustable resonance frequencies up to 240 Hz. The center-of-mass motion of the sphere is monitored magnetically using a dc superconducting quantum interference device as well as optically and exhibits quality factors of up to 2.6×10^7. We also demonstrate 3D magnetic feedback control of the motion of the sphere. The setup is housed in a dilution refrigerator operating at 15 mK. By implementing a cryogenic vibration isolation system, we can attenuate environmental vibrations at 200 Hz by approximately 7 orders of magnitude. The combination of low temperature, large mass and high quality factor provides a promising platform for testing quantum physics in previously unexplored regimes with high mass and long coherence times.

5.1 Introduction

Diamagnets and superconductors partially expel magnetic fields, allowing stable levitation in field minima [Bra89]. A prominent application of magnetically levitated systems is the use as ultraprecise acceleration sensors, most notably in the superconducting gravimeter [Goo99], which relies on the levitation of centimeter-sized hollow superconducting spheres in a stable magnetic field generated by superconducting coils in persistent current mode. More recently, several proposals [RICN+12, CBT12] have highlighted the potential of magnetic levitation for tests of quantum physics with macroscopic, micrometer-sized objects.

Successfully preparing a magnetically levitated particle in a quantum state requires a magnetic trap with low damping, low heating rates and the ability to control the mechanical motion. Some of these features are already present in recent demonstrations of magnetically levitated systems, such as the levitation of permanent magnets above a superconducting surface [VFG+20, GKR+20] and the levitation of diamagnets in the field of permanent magnets at cryogenic temperatures [LLK+21] or room temperature [LKED21]. However, as of yet no system has combined these features. Furthermore, as typical levitation frequencies for these systems range from subhertz to kilohertz, the heating rate is dominated by environmental vibrations.

One of the most promising avenues toward the quantum regime is the levitation of a type-I (or zero-field-cooled type-II) superconductor in a magnetic field produced by persistent currents, as this avoids dissipation due to hysteresis and eddy currents, which is inherent to levitation schemes involving ferromagnets or flux-pinned type-II superconductors [WLO+19, Bra88]. Using persistent currents should result in an extremely stable trap, as both the drift and noise can be kept extremely low [Goo99, VDFZS99, BBS+16]. Working at millikelvin temperatures also naturally enables coupling to nonlinear quantum systems such as superconducting qubits [RICN+12], and miniaturizing the trap architecture [LHRW20, LPH+22, GLHP+23] might lead to fully on-chip coupled quantum systems [PPCS+18]. In comparison with optical levitation, which has already been established as a means for studying massive objects in the quantum regime [DRD+20, MRB+21, TMR+21], magnetostatic levitation has the potential to access a new parameter regime of even larger mass [HA19, NMTS21] and longer coherence times [RICN+12, PPCS+18]: While the size of optically levitated particles is, in practice, limited by the available laser power to the micrometer scale [MGFM17], magnetic levitation can support train-scale objects [FCM95] and due to the static nature of the fields there is no heating from photon absorption.

A first step toward a fully superconducting platform was presented in [vW16], where a lead particle was levitated in the magnetic field of a superconducting coil. This approach, however, was limited in performance by the presence of cryogenic exchange gas at 4 K and environmental vibrations. Here, we report an experiment that provides orders of magnitude improvements in both damping and vibration isolation. We demonstrate the levitation of a superconducting sphere in the magnetic field generated by a superconducting coil. We detect the center of mass (c.m.) motion of the particle magnetically by inductive coupling to a superconducting quantum interference device (SQUID) via a pickup coil (cf. Fig. 18) and demonstrate feedback control of all three c.m. translational degrees of freedom by real-time processing of the SQUID signal. We find that the motion of the particle has a low

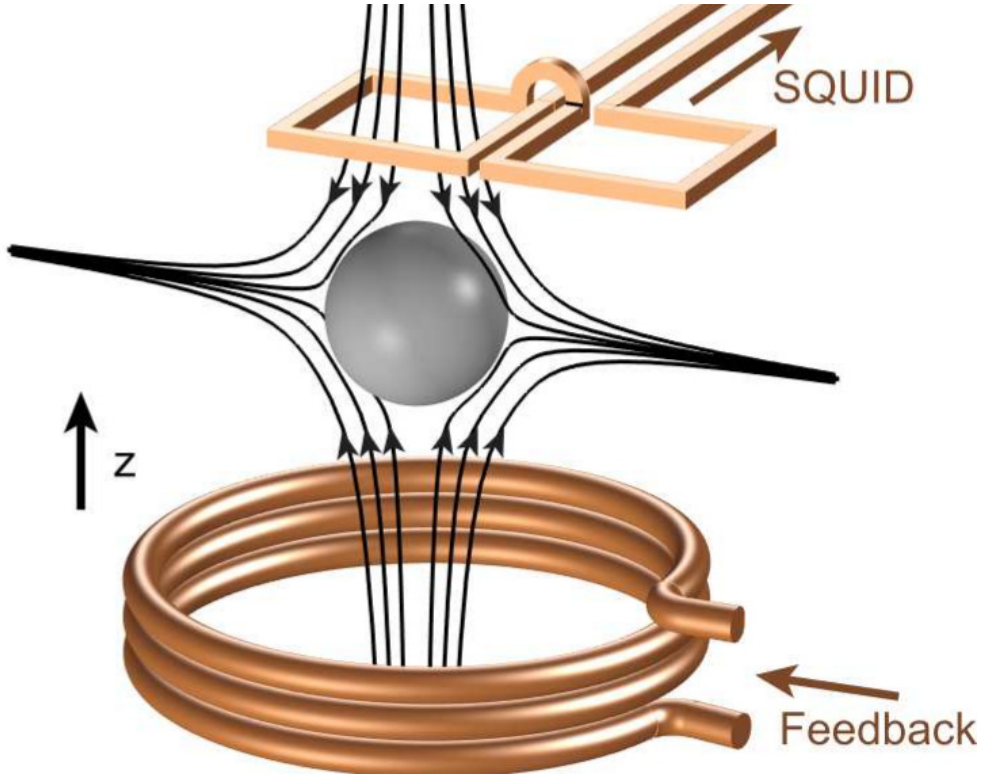


Figure 18: Conceptual representation of the experiment showing the levitated sphere, the pickup coil and the feedback coil. The trap field is depicted by its field lines.

damping rate, corresponding to quality factors of up to 2.6×10^7. We also implement a custom vibration isolation system to reduce heating from environmental vibrations. Finally, we discuss the limitations of our current setup and the improvements that are necessary for ground state cooling.

5.2 Trapping

The energy of an object of volume V with permeability μ in an applied magnetic field B_0 in free space can be approximated by $-1/2V(\mu - \mu_0)B_0^2$ [Bra89], where μ_0 is the permeability of free space. Because $\nabla^2 B_0^2 \geq 0$, stable levitation is possible in a field minimum for $\mu < \mu_0$, i.e. for diamagnets. A superconducting sphere can act as a perfect diamagnet ($\mu = 0$), because it reacts to a change in the applied magnetic field by forming screening currents on its surface, counteracting the applied field and keeping the interior of the sphere field free.

For a sphere trapped in the field of an anti-Helmholtz coil, the resulting potential close to the field minimum is harmonic and two of the c.m. modes are degenerate [RICN+12, HA19]; to lift the degeneracy we use elliptical coils [Sup]. The z direction is along the coil axis, which

coincides with the vertical direction, while x and y are perpendicular to z, with x along the major axis of the coils. We use numerical simulations [Sup] to model the magnetic field created by such an arrangement and confirm that the magnetic field near the center between the coils is well described by $(b_x x, b_y y, b_z z)$, where the field gradients b_i are proportional to the trap current with $|b_x| < |b_y| < |b_z|$ and $b_z = -(b_x + b_y)$. This field shape constitutes a three-dimensional harmonic trap for a levitated superconducting sphere with the c.m. frequencies [Sup]

$$f_i = \sqrt{\frac{3}{8\pi^2 \mu_0 \rho}} |b_i|, \tag{34}$$

where ρ is the density of the sphere.

Our setup is housed in a dilution refrigerator (Bluefors BF-LD400) with a loaded base temperature of approximately 15 mK. The microspheres are commercial (EasySpheres) solder balls with diameter 100(6) µm, made of a 90-10 lead-tin alloy with density $\rho = 10.9 \times 10^3\,\mathrm{kg/m^3}$. Lead-tin is a type-II superconductor with a critical temperature of approximately 7 K [Liv63]. A single sphere is initially placed in a 3D-printed polylactide bowl glued to the lower trap coil, such that it rests around 1 mm below the trap center. The bowl helps to prevent accidental loss of the sphere during assembly and between measurement runs. After cooling down the system to millikelvin temperatures, lift-off is achieved by increasing the coil current until the upward magnetic force on the sphere is stronger than the downward gravitational and adhesive forces. The trap coils are surrounded by an aluminum shield with small openings for optical access and wires, which screens the sphere from magnetic field fluctuations when the aluminum is superconducting. To suppress field fluctuations from the trapping coils and feedback coil, we use a low pass filter and attenuation stages, respectively [Sup].

5.3 Readout

A planar Niobium thin film gradiometric pickup coil consisting of two square loops positioned approximately 400 µm above the trap center is used to magnetically probe the particle motion. Each loop is 145 µm × 145 µm and the separation between the loops is 3 µm. As the particle moves, it induces a current in the pickup loop [Sup], which is connected with Nb wires to the input coil of a SQUID current sensor [SKK20]. The SQUID has an intrinsic flux noise level of $S_\Phi^{1/2} = 0.8\,\mu\Phi_0/\sqrt{\mathrm{Hz}}$, where $\Phi_0 \approx 2.1 \times 10^{-15}$ Wb is the flux quantum. When the SQUID is incorporated into the setup and the pickup loop is connected, the noise rises to $S_\Phi^{1/2} \approx 10\,\mu\Phi_0/\sqrt{\mathrm{Hz}}$. We believe this is due to external field fluctuations inductively coupling into the wires connecting the pickup loop and the SQUID. With a commercial SQUID (Supracon CSblue), that was used for some of the measurements, the noise floor in the setup further increased by an order of magnitude.

To calibrate the SQUID signal, we optically record the motion of the sphere by illuminating it and imaging its shadow on a camera, while simultaneously recording the motion with the SQUID [Sup]. The coupling strengths (flux induced in the SQUID per sphere displacement) for the different motional modes depend on the position of the pickup loop in relation to the sphere as well as the trap gradients, i.e. mechanical frequencies. The highest measured coupling strength was approximately $13 \times 10^3\,\Phi_0/\mathrm{m}$ for the z mode and $3 \times 10^3\,\Phi_0/\mathrm{m}$ for the x and y modes. Together with a flux noise floor of $10\,\mu\Phi_0/\sqrt{\mathrm{Hz}}$ these coupling strengths correspond to a displacement sensitivity of approximately $1\,\mathrm{nm}/\sqrt{\mathrm{Hz}}$ for the z mode. During these measurements the separation between pickup loop and sphere was approximately 400 µm. We estimate that, with a smaller separation and an optimized pickup loop geometry, an improvement of 4 orders of magnitude is possible [Sup].

5.4 Mechanical frequencies

The c.m. frequencies of the particle are visible in the power spectral density (PSD) of the SQUID signal, as shown in Fig. 19. The c.m. frequencies depend linearly on the magnetic field gradient of the trap [see Eq. (34)] and, thus, the current in the trap coils, as shown in the inset. The highest frequency reached in the present setup is 240 Hz (corresponding

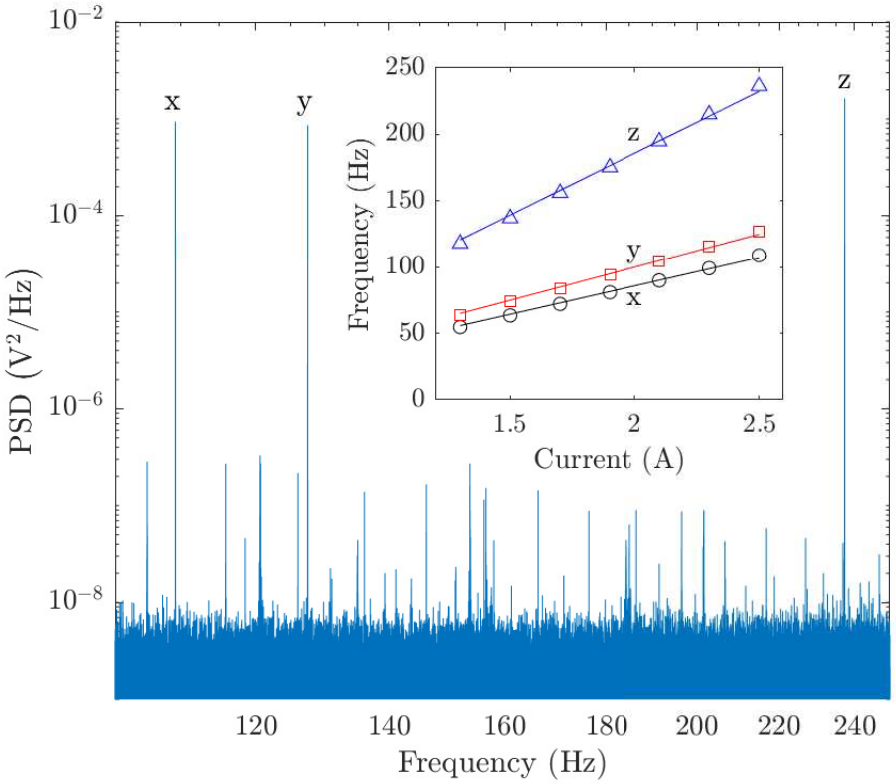


Figure 19: The PSD of the SQUID signal displays three peaks which correspond to the c.m. modes of the particle. The motion of the particle is excited to approximately one micrometer rms displacement in this figure - measurement noise prevents us from resolving the equilibrium motion of the particle. The inset shows the linear dependence of the c.m. frequencies on the trap current. The solid lines are zero-intercept linear fits.

to $b_z \approx 150\,\mathrm{T/m}$), limited by the maximum current output of the low-noise current source. We can trap at lower frequencies, down to $f_z \approx 20\,\mathrm{Hz}$, where the lower limit stems from the gravity-induced shift of the trapping position and our trap geometry. However, at low trapping frequencies, the sphere is strongly excited by environmental vibrations.

We can apply a magnetic feedback force on the levitated sphere by processing the SQUID signal on an FPGA (STEMlab 125-14) and applying a feedback current to a small coil with approximately 20 windings positioned approximately 1 mm below the trap center [Sup]. As measurement noise prevents us from resolving the equilibrium c.m. motion of the particle, we use feedback here only as a means to quickly adjust the amplitudes and prepare other measurements (cf. Fig. 20, inset).

5.5 Quality factor

We measure the quality factor by performing ringdown measurements, where the initial starting amplitude is set by applying an appropriate feedback signal before the start of the measurement. We do see occasional jumps in the damping rate (cf. Fig. 20), which we

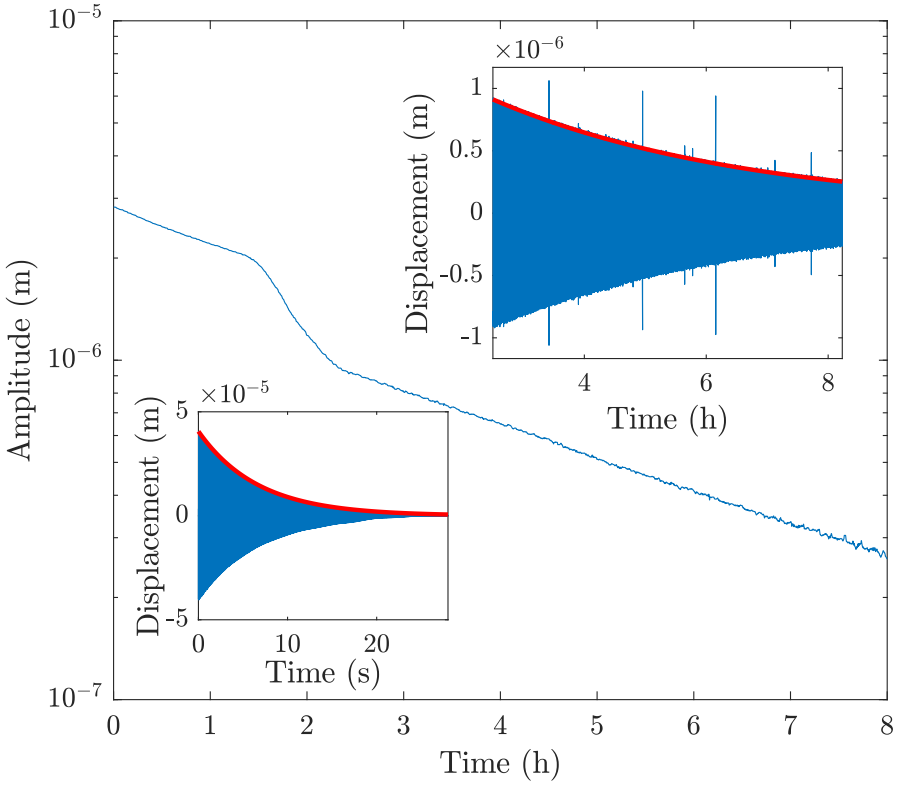


Figure 20: Ringdown measurement of the z mode. The upper right inset shows a linear plot for the latter part of the data, starting at t=2.5 h. The red line is a fit to an exponential decay. The spikes correspond to a brief loss of the SQUID lock, they were removed for the amplitude plot. The lower left inset shows a ringdown while direct feedback is applied (note that the x axis scale is in seconds).

attribute to the detaching and attaching of flux lines to a pinning center. Unpinned flux lines can move within the superconductor (flux creep), a mechanism that is known to cause damping in the levitation of flux-pinned superconductors or magnets [Bra88, NBKN90]. Although we do not apply a magnetic field during the cooldown, there is a nonzero background field, and hence, we expect some frozen-in flux to be present in the levitated sphere. As a consequence, the measured quality factors vary with time and between measurement runs, but they are generally between 1×10^7 and 2.5×10^7 for the z mode and about half as high for the x and y modes. The highest quality factor we have measured is 2.6×10^7 at 212 Hz, corresponding to a dissipation rate of $5 \times 10^{-5}\,\mathrm{s}^{-1}$, and likely still limited by flux creep inside the particle. We also consider other possible contributions to the damping [Sup], but find that the expected contributions cannot explain the measured values. In future experiments we plan to use a particle made of a type-I superconductor such as monocrystalline lead, which will expel all magnetic flux via the Meissner effect and prevent flux creep.

5.6 Sensing

A massive system acting as a harmonic oscillator can be used for force and acceleration sensing, with the sensitivities depending on the mass m and the dissipation rate γ of the oscillator. In equilibrium with a thermal bath at temperature T_0, the thermal force noise is given by $\sqrt{S_{FF}^{\mathrm{th}}} = \sqrt{4k_B T_0 m\gamma}$ [Kub66], where k_B is Boltzmann's constant. The dissipation rate γ is related to the quality factor Q and the angular mechanical resonance frequency

ω_0 by $\gamma = \omega_0/Q$. The corresponding acceleration sensitivity is $\sqrt{S_{FF}^{\mathrm{th}}}/m$. For a particle of mass $m \approx 5.6\,\mu\mathrm{g}$, assuming it is in thermal equilibrium with its surroundings in the dilution refrigerator at 15 mK, this sets the limits for force and acceleration sensing at $5 \times 10^{-19}\,\mathrm{N}/\sqrt{\mathrm{Hz}}$ and $9 \times 10^{-12}\,\mathrm{g}/\sqrt{\mathrm{Hz}}$, using our highest measured quality factor $Q = 2.6 \times 10^7$ at 212 Hz. Our current experimental sensitivities are approximately 1 order of magnitude above the thermal noise, limited by drifts in the trap current and measurement noise [Sup].

5.7 Cryogenic vibration isolation

Vibrations of the cryostat accelerate the trapping coils and, thus, the trap center, effecting a force onto the levitated sphere. Denoting the vibrational PSD by $S_{\epsilon\epsilon}$, the displacement PSD of our sphere becomes $|\chi(\omega)|^2 m^2 \omega_0^4 S_{\epsilon\epsilon}(\omega)$, where χ denotes the mechanical susceptibility. From independent accelerometer measurements on the cryostat, we estimate $\sqrt{S_{\epsilon\epsilon}} \approx 1 \times 10^{-10}\,\mathrm{m}/\sqrt{\mathrm{Hz}}$ at 200 Hz, which would result in a peak height of $2.6 \times 10^{-3}\,\mathrm{m}/\sqrt{\mathrm{Hz}}$ and a root-mean-square displacement of 9 µm, corresponding to an effective temperature of 6×10^{10} K. To mitigate the effects of vibrations, we implement a passive cryogenic vibration isolation system: the aluminum shield containing the trap is hung from the 4 K stage of the dilution refrigerator via 38 µm-thick stainless steel wires and two intermediate stages. The system acts like a triple pendulum, offering isolation from horizontal (x and y) vibrations, while the elasticity of the wires provides isolation from vertical (z) vibrations. To prevent coupling of external vibrations into the experimental setup via electrical wires and the copper braids used for thermalization, we connect these wires and braids to an additional vibration isolation platform, as represented in Fig. 21. Vibrations of the experimental system could also be induced by fluctuating magnetic fields acting on the aluminum shield. To prevent this, we surround the setup by a second aluminum shield which is rigidly mounted to the cryostat. We typically operate at vertical (z) trap frequencies above 200 Hz and initially found that the vibration isolation system attenuates vibrations at these frequencies by approximately 5 orders of magnitude. We have further improved the system by optimizing the mass and wire length for each stage, leading to an attenuation of almost 7 orders of magnitude at 200 Hz. Theoretically, vibrations along the horizontal axis as well as librational fluctuations around the axes are suppressed even more, but in practice, we expect vibrations from the vertical axis to couple into all degrees of freedom [AMTM92]. More details on the vibration isolation platform are provided in [Sup].

5.8 Prospects for ground state cooling

Now, we discuss the potential of this system to reach the ground state, which would be a first step toward accessing the quantum regime. SQUID noise can be separated into flux noise $S_{\phi\phi}$ and noise in the circulating current S_{JJ}, which may be partially correlated [TC79] and fulfill $\sqrt{S_{\phi\phi}S_{JJ} - S_{\phi J}^2} \geq \hbar$ [KVHC81, DLZ83]. The flux noise results in the measurement noise $\frac{S_{\phi\phi}}{\eta^2}$, while the current noise corresponds to a back action $\eta^2 S_{JJ}$, where η is the coupling strength. Applying direct feedback with optimum gain and assuming vanishing correlations between flux and current noise, one can estimate the final phonon occupation [Sup] as

$$\bar{n} = \frac{1}{\hbar\eta^2}\left(k_B T_0 m\gamma \tilde{L_S}\right) + \frac{1}{2}\left(\frac{\sqrt{S_{\phi\phi}S_{JJ}}}{\hbar} - 1\right),$$

where $\tilde{L_S} = \sqrt{\frac{S_{\phi\phi}}{S_{JJ}}}$ depends on the working point of the SQUID and is typically on the order of the SQUID inductance L_S. The first term describes heating from coupling to an

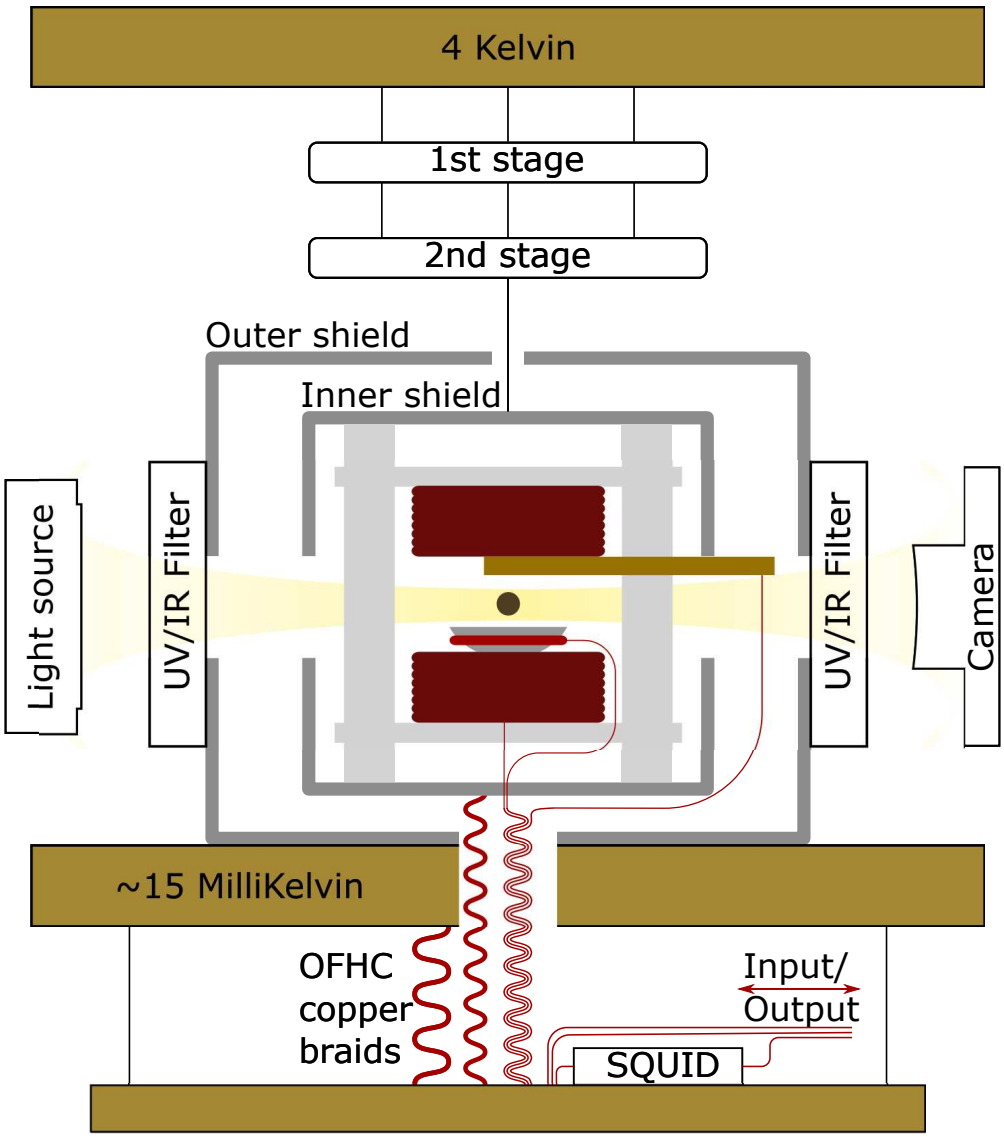


Figure 21: Sketch of the setup including the vibration isolation system (not to scale). The light source is turned on only for calibration measurements. The UV-IR cutoff filters on the millikelvin stage prevent ambient radiation from heating the levitated sphere. Thermal connections are made with oxygen free high conductivity (OFHC) copper braids.

effective thermal reservoir with temperature T_0, while the second term is the backaction limit under continuous feedback. We can reach a coupling strength of $\eta \approx 5.5 \times 10^7\,\Phi_0/\mathrm{m}$ [Sup], so assuming $T_0 \approx 15\,\mathrm{mK}$ and a typical SQUID inductance of $L_S \approx 15\,\mathrm{pH}$, we need $\gamma \approx 1 \times 10^{-6}\,\mathrm{s}^{-1}$ to keep the former negligible. Ground state cooling then requires $\sqrt{S_{\phi\phi}S_{JJ}} < 3\hbar$. In addition to feedback cooling with a SQUID, we will investigate other potential avenues for ground state cooling such as coupling the levitated sphere to a flux qubit or a microwave cavity [RICN+12, STAP+20, SSB17, ZJSK20].

5.9 Discussion and outlook

We built a platform based on the diamagnetic levitation of a superconductor in a magnetostatic trap in a dilution refrigerator at 15 mK and demonstrate quality factors exceeding 1×10^7 for the three c.m. modes of a 5.6 µg oscillator. The high quality factors result in excellent sensing capabilities, with achievable force (acceleration) sensitivities that are, otherwise, only reached with much smaller (larger) masses [HVT+17, Goo99]. We also demonstrated simultaneous feedback cooling of all c.m. modes using either direct or parametric feedback. While we have focused, here, on a 100 µm-sized sphere, the setup allows for particles from submicron size to millimeter size to be levitated [HA19]. We have identified improvements to mitigate technical issues: First, we plan to use a type-I superconducting sphere to avoid trapped flux and dissipation caused by flux creep, which we expect is limiting our quality factor. Second, we can improve the magnetomechanical coupling by 4 orders of magnitude by better positioning of the pickup coil and by using a pickup coil with multiple windings matched to the input coil of the SQUID. Together with an optimized SQUID shielded from environmental noise (such that our readout is limited by the intrinsic SQUID noise), this would result in an improvement of the measurement noise floor by 6 orders of magnitude [Sup]. Third, we plan to implement a persistent current switch to improve the trap current stability. With these improvements, our system offers a promising approach for bringing microgram objects to the quantum regime, which opens a potential avenue for quantum-limited acceleration sensing or even probing quantum effects of gravity [KP20, MV17, BMM+17, Asp22].
The data of this study are available at the Zenodo repository [Hof23].

Acknowledgements

We thank G. Kirchmair, O. Romero-Isart, and A. Sanchez for discussions. We thank Matthias Rudolph for assisting with the initial setup of a SQUID measurement system. We thank F. Wulschner for setting up a helium flow cryostat and assisting with measurements during the initial phase of the project. This work was supported by the European Union's Horizon 2020 research and innovation programme under Grant Agreement No. 863132 (iQLev), the European Union's Horizon Europe 2021-2027 Framework Programme under Grant Agreement No. 101080143 (SuperMeQ), the European Research Council (ERC CoG QLev4G and ERC Synergy QXtreme), and the Austrian Science Fund (FWF) under Project No. F40 (SFB FOQUS). We gratefully acknowledge financial support from the Deutsche Forschungsgemeinschaft (DFG, German Research Foundation) under Germany's Excellence Strategy Grant No. EXC-2111 – 390814868. G. H. acknowledges support from the Swedish Research Council (Grant No. 2020-00381). P. S. is supported by the Alexander von Humboldt Foundation through a Feodor Lynen Fellowship.

5.10 References

These are the references cited in the author's version of the manuscript.

[AMTM92] T. L. Aldcroft, P. F. Michelson, R. C. Taber, and F. A. McLoughlin. Six-degree-of-freedom vibration isolation systems with application to resonant-mass gravitational radiation detectors. *Review of Scientific Instruments*, 63(8):3815–3827, 1992.

[ARK+88] D. D. Awschalom, J. R. Rozen, M. B. Ketchen, W. J. Gallagher, A. W. Kleinsasser, R. L. Sandstrom, and B. Bumble. Low-noise modular microsusceptometer using nearly quantum limited dc SQUIDs. *Applied Physics Letters*, 53(21):2108–2110, 1988.

[Asp22] Markus Aspelmeyer. How to avoid the appearance of a classical world in gravity experiments, 2022.

[BBS+16] J. W. Britton, J. G. Bohnet, B. C. Sawyer, H. Uys, M. J. Biercuk, and J. J. Bollinger. Vibration-induced field fluctuations in a superconducting magnet. *Phys. Rev. A*, 93:062511, Jun 2016.

[BMM+17] Sougato Bose, Anupam Mazumdar, Gavin W. Morley, Hendrik Ulbricht, Marko Toroš, Mauro Paternostro, Andrew A. Geraci, Peter F. Barker, M. S. Kim, and Gerard Milburn. Spin entanglement witness for quantum gravity. *Phys. Rev. Lett.*, 119:240401, Dec 2017.

[Bra88] Ernst Helmut Brandt. Friction in levitated superconductors. *Applied Physics Letters*, 53:1554–1556, 1988.

[Bra89] E. H. Brandt. Levitation in physics. *Science*, 243(4889):349–355, 1989.

[CBT12] M. Cirio, G. K. Brennen, and J. Twamley. Quantum magnetomechanics: Ultrahigh-Q-levitated mechanical oscillators. *Phys. Rev. Lett.*, 109:147206, Oct 2012.

[CCTL98] P. Carelli, M. G. Castellano, G. Torrioli, and R. Leoni. Low noise multiwasher superconducting interferometer. *Applied Physics Letters*, 72(1):115–117, 1998.

[CG96] John C. Crocker and David G. Grier. Methods of digital video microscopy for colloidal studies. *Journal of Colloid and Interface Science*, 179(1):298–310, 1996.

[DLZ83] V. Danilov, K. Likharev, and A. Zorin. Quantum noise in squids. *IEEE Transactions on Magnetics*, 19(3):572–575, 1983.

[DRD+20] Uros Delic, Michael Reisenbauer, Kahan Dare, David Grass, Vuletic Vladan, Nikolai Kiesel, and Markus Aspelmeyer. Cooling of a levitated nanoparticle to the motional quantum ground state. *Science*, 367:892–895, 2020.

[FBC+08] P. Falferi, M. Bonaldi, M. Cerdonio, R. Mezzena, G. A. Prodi, A. Vinante, and S. Vitale. $10\hbar$ superconducting quantum interference device amplifier for acoustic gravitational wave detectors. *Applied Physics Letters*, 93(17):172506, 2008.

[FCM95] Pei-Zen Chang Francis C. Moon. *Superconducting Levitation: Applications to Bearings and Magnetic Transportation*. Wiley-VCH, 1995.

[GKR+20] J. Gieseler, A. Kabcenell, E. Rosenfeld, J. D. Schaefer, A. Safira, M. J. A. Schuetz, C. Gonzalez-Ballestero, C. C. Rusconi, O. Romero-Isart, and M. D. Lukin. Single-spin magnetomechanics with levitated micromagnets. *Phys. Rev. Lett.*, 124:163604, Apr 2020.

[GLHP+23] Martí Gutierrez Latorre, Gerard Higgins, Achintya Paradkar, Thilo Bauch, and Witlef Wieczorek. Superconducting microsphere magnetically levitated in an anharmonic potential with integrated magnetic readout. *Phys. Rev. Appl.*, 19:054047, May 2023.

[Goo99] John M. Goodkind. The superconducting gravimeter. *Review of Scientific Instruments*, 70(11):4131–4152, 1999.

[GOST98] M. E. Gehm, K. M. O'Hara, T. A. Savard, and J. E. Thomas. Dynamics of noise-induced heating in atom traps. *Phys. Rev. A*, 58:3914–3921, Nov 1998.

[HA19] J Hofer and M Aspelmeyer. Analytic solutions to the Maxwell–London equations and levitation force for a superconducting sphere in a quadrupole field. *Physica Scripta*, 94(12):125508, oct 2019.

[HK90] L. D. Hinkle and B. R. F. Kendall. Pressure-dependent damping of a particle levitated in vacuum. *Journal of Vacuum Science & Technology A*, 8(3):2802–2805, 1990.

[Hof23] J. Hofer et al. Data used in the article "High-Q Magnetic Levitation and Control of Superconducting Microspheres at Millikelvin Temperatures". *Zenodo,*, 2023.

[HVT+17] David Hempston, Jamie Vovrosh, Marko Toroš, George Winstone, Muddassar Rashid, and Hendrik Ulbricht. Force sensing with an optically levitated charged nanoparticle. *Applied Physics Letters*, 111(13):133111, 2017.

[KP20] Shreya P. Kumar and Martin B. Plenio. On quantum gravity tests with composite particles. *Nature Communications*, 11(1):3900, Aug 2020.

[Kub66] R Kubo. The fluctuation-dissipation theorem. *Reports on Progress in Physics*, 29(1):255–284, jan 1966.

[KVHC81] Roger H. Koch, D. J. Van Harlingen, and John Clarke. Quantum noise theory for the dc SQUID. *Applied Physics Letters*, 38(5):380–382, 1981.

[LHRW20] Martí Gutierrez Latorre, Joachim Hofer, Matthias Rudolph, and Witlef Wieczorek. Chip-based superconducting traps for levitation of micrometer-sized particles in the Meissner state. *Superconductor Science and Technology*, 33(10):105002, aug 2020.

[Liv63] J. D. Livingston. Magnetic properties of superconducting lead-base alloys. *Phys. Rev.*, 129:1943–1949, Mar 1963.

[LKED21] Charles W. Lewandowski, Tyler D. Knowles, Zachariah B. Etienne, and Brian D'Urso. High-sensitivity accelerometry with a feedback-cooled magnetically levitated microsphere. *Phys. Rev. Applied*, 15:014050, Jan 2021.

[LLK+21] Yingchun Leng, Rui Li, Xi Kong, Han Xie, Di Zheng, Peiran Yin, Fang Xiong, Tong Wu, Chang-Kui Duan, Youwei Du, Zhang-qi Yin, Pu Huang, and Jiangfeng Du. Mechanical dissipation below 1μHz with a cryogenic diamagnetic levitated micro-oscillator. *Phys. Rev. Applied*, 15:024061, Feb 2021.

[LPH+22] Martí Gutierrez Latorre, Achintya Paradkar, David Hambraeus, Gerard Higgins, and Witlef Wieczorek. A chip-based superconducting magnetic trap for levitating superconducting microparticles. *IEEE Transactions on Applied Superconductivity*, 32(4):1–5, 2022.

[MC83] J. Martinis and J. Clarke. Measurements of current noise in dc SQUIDS. *IEEE Transactions on Magnetics*, 19(3):446–448, 1983.

[MC85] John M. Martinis and John Clarke. Signal and noise theory for a dc SQUID amplifier. *Journal of Low Temperature Physics*, 61(3):227–236, Nov 1985.

[MGFM17] Fernando Monteiro, Sumita Ghosh, Adam Getzels Fine, and David C. Moore. Optical levitation of 10-ng spheres with nano-g acceleration sensitivity. *Phys. Rev. A*, 96:063841, Dec 2017.

[MRB+21] Lorenzo Magrini, Philipp Rosenzweig, Constanze Bach, Andreas Deutschmann-Olek, Sebastian G. Hofer, Sungkun Hong, Nikolai Kiesel, Andreas Kugi, and Markus Aspelmeyer. Real-time optimal quantum control of mechanical motion at room temperature. *Nature*, 595(7867):373–377, 2021.

[MV17] C. Marletto and V. Vedral. Gravitationally induced entanglement between two massive particles is sufficient evidence of quantum effects in gravity. *Phys. Rev. Lett.*, 119:240402, Dec 2017.

[NBKN90] V. V. Nemoshkalenko, E. H. Brandt, A. A. Kordyuk, and B. G. Nikitin. Dynamics of a permanent magnet levitating above a high-T_c superconductor. *Physica C*, 170:481–485, 1990.

[NMC+17] L. Neuhaus, R. Metzdorff, S. Chua, T. Jacqmin, T. Briant, A. Heidmann, P.-F. Cohadon, and S. Deléglise. PyRPL (Python Red Pitaya Lockbox) — An open-source software package for FPGA-controlled quantum optics experiments. In *2017 Conference on Lasers and Electro-Optics Europe European Quantum Electronics Conference (CLEO/Europe-EQEC)*, pages 1–1, 2017.

[NMTS21] Carles Navau, Stefan Minniberger, Michael Trupke, and Alvaro Sanchez. Levitation of superconducting microrings for quantum magnetomechanics. *Phys. Rev. B*, 103:174436, May 2021.

[PPB21] T. W. Penny, A. Pontin, and P. F. Barker. Performance and limits of feedback cooling methods for levitated oscillators: A direct comparison. *Phys. Rev. A*, 104:023502, Aug 2021.

[PPCS+18] H Pino, J Prat-Camps, K Sinha, B Prasanna Venkatesh, and O Romero-Isart. On-chip quantum interference of a superconducting microsphere. *Quantum Science and Technology*, 3(2):025001, jan 2018.

[RICN+12] O. Romero-Isart, L. Clemente, C. Navau, A. Sanchez, and J. I. Cirac. Quantum magnetomechanics with levitating superconducting microspheres. *Phys. Rev. Lett.*, 109:147205, 2012.

[SKK20] Jan-Hendrik Storm, Oliver Kieler, and Rainer Körber. Towards ultrasensitive SQUIDs based on submicrometer-sized Josephson junctions. *IEEE Transactions on Applied Superconductivity*, 30(7):1–5, 2020.

[SSB17] Olga Shevchuk, Gary A. Steele, and Ya. M. Blanter. Strong and tunable couplings in flux-mediated optomechanics. *Phys. Rev. B*, 96:014508, Jul 2017.

[STAP+20] Philip Schmidt, Mohammad T. Amawi, Stefan Pogorzalek, Frank Deppe, Achim Marx, Rudolf Gross, and Hans Huebl. Sideband-resolved resonator electromechanics based on a nonlinear Josephson inductance probed on the single-photon level. *Communications Physics*, 3(1):233, Dec 2020.

[Sup] See supplemental material, which includes Refs. [NMC+17, HK90, MC85, CG96, ARK+88, CCTL98, Whe28, PPB21, MC83, FBC+08, GOST98], for more information on the derivation of trap parameters, the effects of trap current fluctuations, the vibration isolation system, estimations of different contributions to the damping, the calibration of the SQUID signal as well as more details on ground state cooling.

[TC79] Claudia D. Tesche and John Clarke. dc SQUID: Current noise. *Journal of Low Temperature Physics*, 37(3):397–403, Nov 1979.

[TMR+21] Felix Tebbenjohanns, M. Luisa Mattana, Massimiliano Rossi, Martin Frimmer, and Lukas Novotny. Quantum control of a nanoparticle optically levitated in cryogenic free space. *Nature*, 595(7867):378–382, 2021.

[VDFZS99] R. S. Van Dyck, D. L. Farnham, S. L. Zafonte, and P. B. Schwinberg. Ultrastable superconducting magnet system for a penning trap mass spectrometer. *Review of Scientific Instruments*, 70(3):1665–1671, 1999.

[VFG+20] A. Vinante, P. Falferi, G. Gasbarri, A. Setter, C. Timberlake, and H. Ulbricht. Ultralow mechanical damping with Meissner-levitated ferromagnetic microparticles. *Phys. Rev. Appl.*, 13(6), 2020.

[vW16] Bob van Waarde. *The lead zeppelin : a force sensor without a handle*. Ph.D. thesis, Leiden University, 2016.

[Whe28] H.A. Wheeler. Simple inductance formulas for radio coils. *Proceedings of the Institute of Radio Engineers*, 16(10):1398–1400, 1928.

[WLO+19] Tao Wang, Sean Lourette, Sean R. O'Kelley, Metin Kayci, Y.B. Band, Derek F. Jackson Kimball, Alexander O. Sushkov, and Dmitry Budker. Dynamics of a ferromagnetic particle levitated over a superconductor. *Phys. Rev. Applied*, 11:044041, Apr 2019.

[ZJSK20] D. Zoepfl, M. L. Juan, C. M. F. Schneider, and G. Kirchmair. Single-photon cooling in microwave magnetomechanics. *Phys. Rev. Lett.*, 125:023601, Jul 2020.

Supplemental material: High-Q magnetic levitation and control of superconducting microspheres at millikelvin temperatures

J. Hofer[1,2], R. Gross[3,4,5], G. Higgins[2,6], H. Huebl[3,4,5], O. F. Kieler[7], R. Kleiner[8], D. Koelle[8], P. Schmidt[2], J. A. Slater[1], M. Trupke[1], K. Uhl[8], T. Weimann[7], W. Wieczorek[1,6], and M. Aspelmeyer[1,2]

[1]Faculty of Physics, Vienna Center for Quantum Science and Technology (VCQ), University of Vienna, A-1090 Vienna, Austria
[2]Institute for Quantum Optics and Quantum Information (IQOQI), Austrian Academy of Sciences, A-1090 Vienna, Austria
[3]Walther-Meißner-Institut, Bayerische Akademie der Wissenschaften, D-85748 Garching, Germany
[4]Physik-Department, Technische Universität München, D-85748 Garching, Germany
[5]Munich Center for Quantum Science and Technology (MCQST), D-80799 München, Germany
[6]Department of Microtechnology and Nanoscience (MC2), Chalmers University of Technology, S-412 96 Gothenburg, Sweden
[7]Physikalisch-Technische Bundesanstalt (PTB), D-38116 Braunschweig, Germany
[8]Physikalisches Institut, Center for Quantum Science (CQ) and LISA$^+$, University of Tuebingen, D-72076 Tuebingen, Germany

Abstract

We provide more information on: (i)The field distribution of the magnetic trap, the resulting trap frequencies and the derivation of the coupling strength. (ii)Effects of current fluctuations and drifts on the measured spectral density. (iii)Limits to the force sensitivity due to measurement noise and current drifts. (iv)Feedback control of the levitated particle. (v)The vibration isolation system. (vi)Possible contributions to the damping. (vii)Calibration of the SQUID signal. (viii)Optimizations and requirements for ground state cooling.

5.11 Derivation of the magnetic trap's properties

5.11.1 Trapping field

We performed numerical simulations in COMSOL MULTIPHYSICS to predict the field configuration generated by the arrangement of our trapping coils. The design of the coils and the simulated magnetic field density are shown in Fig. 40a,b. The field gradients for a trap current of 2.5 A are obtained as $(b_x, b_y, b_z) = (57, 90, 147)\mathrm{T/m}$, which would correspond to frequencies of $(92, 144, 236)$Hz. Comparing this to the measured values of $(109, 127, 236)$Hz we can see that the agreement between the numerical and measured z-mode frequency is excellent, but that the simulations predict a much stronger split for the x- and y-mode than what we see in the experiment. This is likely due to the fact that the spooling process resulted in coils that were more circular than the design (cf. Fig. 40c). For a perfectly circular coil the x- and y-mode frequencies are degenerate [HA19], so a smaller frequency split is to be expected. Close to the center the field is very well approximated by a quadrupole field: Within a cubic volume of $200\,\mu\mathrm{m} \times 200\,\mu\mathrm{m} \times 200\,\mu\mathrm{m}$ the maximum relative root-mean-square deviation, defined as $|\mathbf{B_{sim}} - (b_x x, b_y y, b_z z)|/|\mathbf{B_{sim}}|$, is less than 0.1 %.

5.11.2 Mechanical frequencies

In this section we build on the calculations in [HA19] to analytically calculate the magnetic field distribution for a superconducting sphere in an axially-asymmetric magnetic quadrupole field. We consider a superconducting sphere at the origin of the coordinate system and displaced from the center the quadrupole field by $\mathbf{x_0} = (x_0, y_0, z_0)$. The applied field then reads

$$\mathbf{B_0} = (b_x(x + x_0), b_y(y + y_0), b_z(z + z_0))\,.$$

As our sphere's radius R is much larger than the expected penetration depth λ [Liv63], we can use the approximation $\lambda/R \to 0$, i.e. we assume $\mathbf{B} = 0$ inside the sphere and $B_r = 0$ on the sphere's surface [HA19], where B_r denotes the radial component of the field. As there are no currents outside the sphere, there exists a scalar potential Φ s.t. $\mathbf{B} = \mathbf{B_0} - \nabla\Phi$ and

$$\Phi = \sum_{n=0}^{\infty} r^{-(n+1)} \sum_{m=-n}^{n} a_{n,m} Y_n^m,$$

where $r = \sqrt{x^2 + y^2 + z^2}$ and the Y_n^m are spherical harmonics. The coefficients $a_{n,m}$ are determined by the boundary condition $B_{0,r} = (\nabla\Phi)_r$ on the sphere's surface as

$$\begin{aligned}
a_{1,0} &= -\ b_z\sqrt{\pi/3}\ R^3 z_0,\\
a_{1,-1} &= -\ \sqrt{\pi/6}\ R^3(b_x x_0 + i b_y y_0),\\
a_{1,1} &= \ \ \sqrt{\pi/6}\ R^3(b_x x_0 - i b_y y_0),\\
a_{2,0} &= -\ b_z\sqrt{4\pi/45}\ R^5,\\
a_{2,-2} &= \ \ (b_y - b_x)\sqrt{2\pi/135}\ R^5,\\
a_{2,2} &= \ \ a_{2,-2},
\end{aligned}$$

all other coefficients are zero. From this field distribution we obtain the force on the sphere as

$$\mathbf{F} = -\frac{3V}{2\mu_0}\left(b_x^2 x_0, b_y^2 y_0, b_z^2 z_0\right),$$

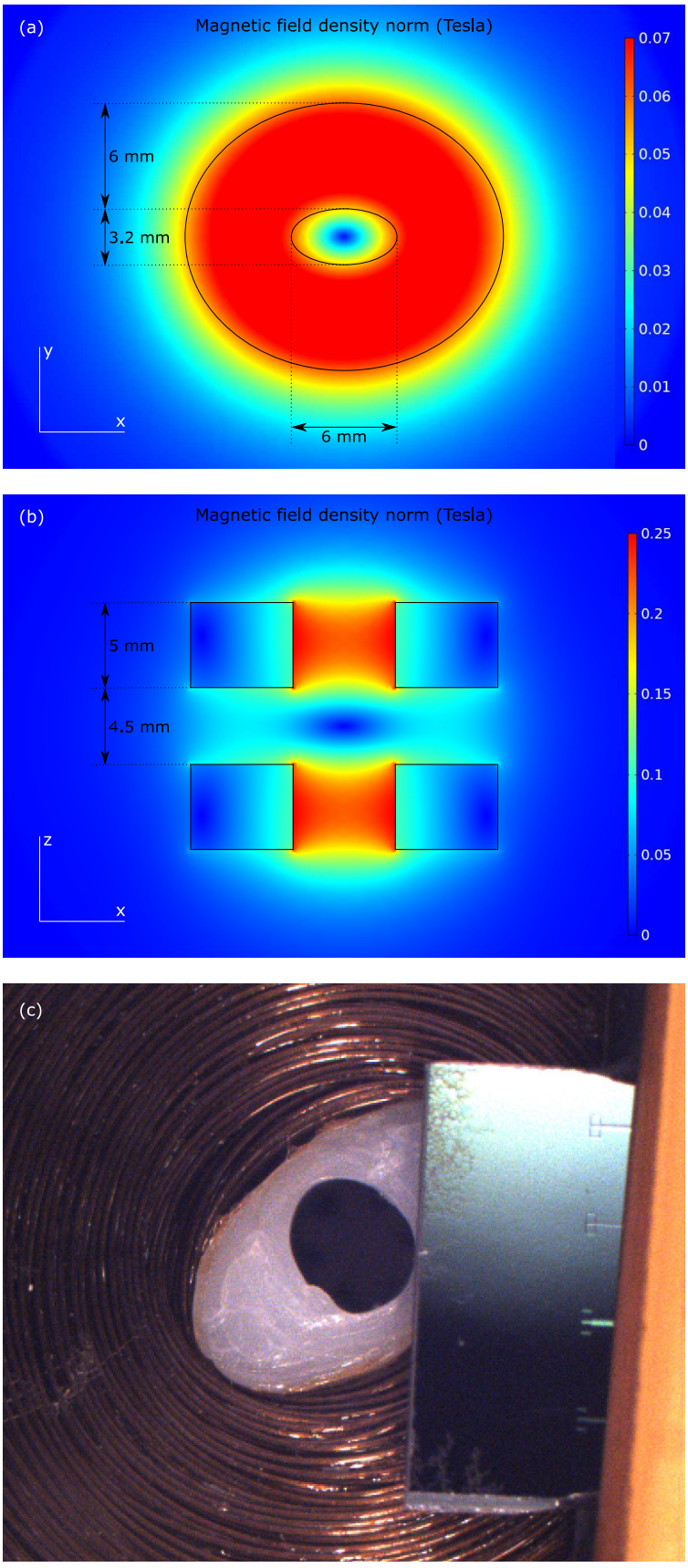


Figure 22: (a,b)Numerical simulations of the magnetic field density created by coaxial elliptical coils with counter-propagating currents. (c)Photograph of the top surface of a single trap coil. On the right side the wafer with the pickup loops is visible (not in its final position).

where V is the volume of the sphere. The magnetic field thus creates a harmonic trapping potential for a superconducting sphere, with trapping frequencies described by

$$f_i = \sqrt{\frac{3}{8\pi^2\mu_0\rho}}|b_i|.$$

5.11.3 Coupling strength

The linear coupling strength with respect to a pickup loop that is described by a closed path γ is defined as $\nu_i = \partial_i\Phi_\gamma$, where Φ_γ is the flux through the area enclosed by the pickup loop and $i \in \{x_0, y_0, z_0\}$. We can express this as

$$\nu_i = \int_\gamma \mathrm{d}\gamma\ \partial_i\mathbf{A}, \tag{35}$$

where $\mathbf{A}$ denotes the magnetic vector potential, defined by $\nabla\times\mathbf{A} = \mathbf{B}$ and $\nabla\mathbf{A} = 0$. While the resulting expressions are generally bulky, they can be easily evaluated using a computer algebra system, we use Wolfram Mathematica. We measure the current that is induced in the pickup loop using a SQUID current sensor, i.e. the pickup loop is connected to an input coil on the same wafer as the SQUID and inductively coupled to the SQUID. The coupling strength with respect to the SQUID is thus obtained as $\eta_i = \nu_i M/L$, where L is the inductance of the circuit formed by pickup loop, input coil of the current sensor, and the connecting wires, while M is the mutual inductance between input coil and SQUID. In our case $M/L \approx 0.02$. In Fig. 41 we plot the dependence of the coupling strength on the vertical separation between trap center and pickup loop, when the x- and y-position of the pickup loop relative to the trap center (as shown in the inset) is approximately the same as what we estimate for our setup (from pictures taken at room temperature, cf. Fig. 40c). The horizontal dotted lines correspond to the measured coupling strengths, while the vertical dotted line corresponds to the vertical separation extracted from camera images (approx. 400 µm) of the levitated sphere.

5.11.4 Trap displacement due to gravity

The rest position of the sphere is slightly displaced from the field minimum due to gravity. In our case the setup is aligned such that the direction of gravity coincides with the z-axis. The expected displacement is thus

$$z_g = -g/(2\,\pi\,f_z)^2,$$

where $g \approx 9.81\,\mathrm{m/s^2}$. In general this displacement needs to be taken into account when calculating the coupling strength, but for larger trapping frequencies it becomes negligible. We usually operate at $f_z > 200\,\mathrm{Hz}$, for which $z_g < 6\,\mu\mathrm{m}$.

5.12 Current fluctuations

Since the sphere's motional frequencies depend linearly on the trap current, current fluctuations result in frequency fluctuations, and thus can cause heating as well as broadening of the mechanical spectral peaks. We stabilize the trap current both passively and actively, as described in the following. We implement a first-order low-pass RL-filter by adding a short copper wire (resistance $\mathrm{R_C}$) in parallel to the trap coils (inductance $\mathrm{L_C}$). We characterize the filter's cut-off frequency by measuring its step response in an empty trap (Fig. 24). The cutoff frequency is $R_C/L_C \approx 0.036\,\mathrm{s^{-1}}$, which results in an attenuation of approximately

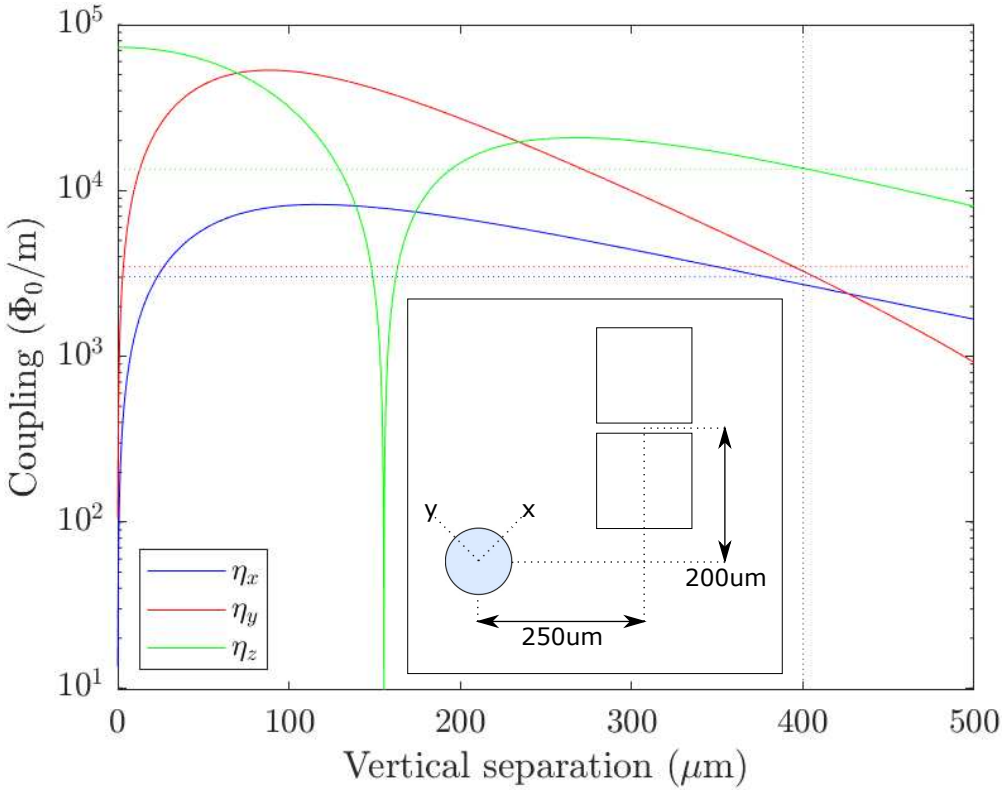


Figure 23: Dependence of the coupling strength on the vertical separation between trap center and pickup loop, when the separation along x and y is as shown in the inset - these are the values we estimate for our setup. The vertical separation in our setup is approximately 400 µm. The dotted horizontal lines correspond to the measured coupling strengths.

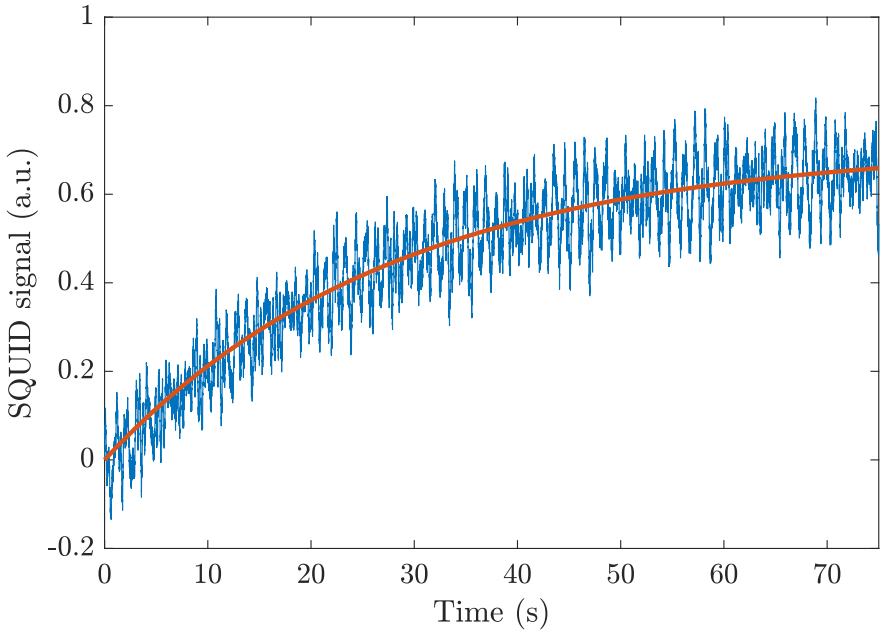


Figure 24: Step response of the filter measured using the SQUID. The solid line is a fit of the filter's step response $1 - \exp(-R_C/L_C\, t)$.

$-180\,\mathrm{dB}$ at $200\,\mathrm{Hz}$, while the added thermal current noise from the copper wire is only on the order of $1 \times 10^{-11}\,\mathrm{A}/\sqrt{\mathrm{Hz}}$.

We actively stabilize the filtered trap current by monitoring the mean current source output using a digital ammeter and updating the current source output based on an estimation of the trap current. This lessens current drifts and the associated resonance broadening, as seen by comparing Fig. 25(a) with (b). Even with active current stabilization we observe drifts of the particle's resonance frequency shown in Fig. 25(d), which we attribute to low-frequency noise in the ammeter reading.

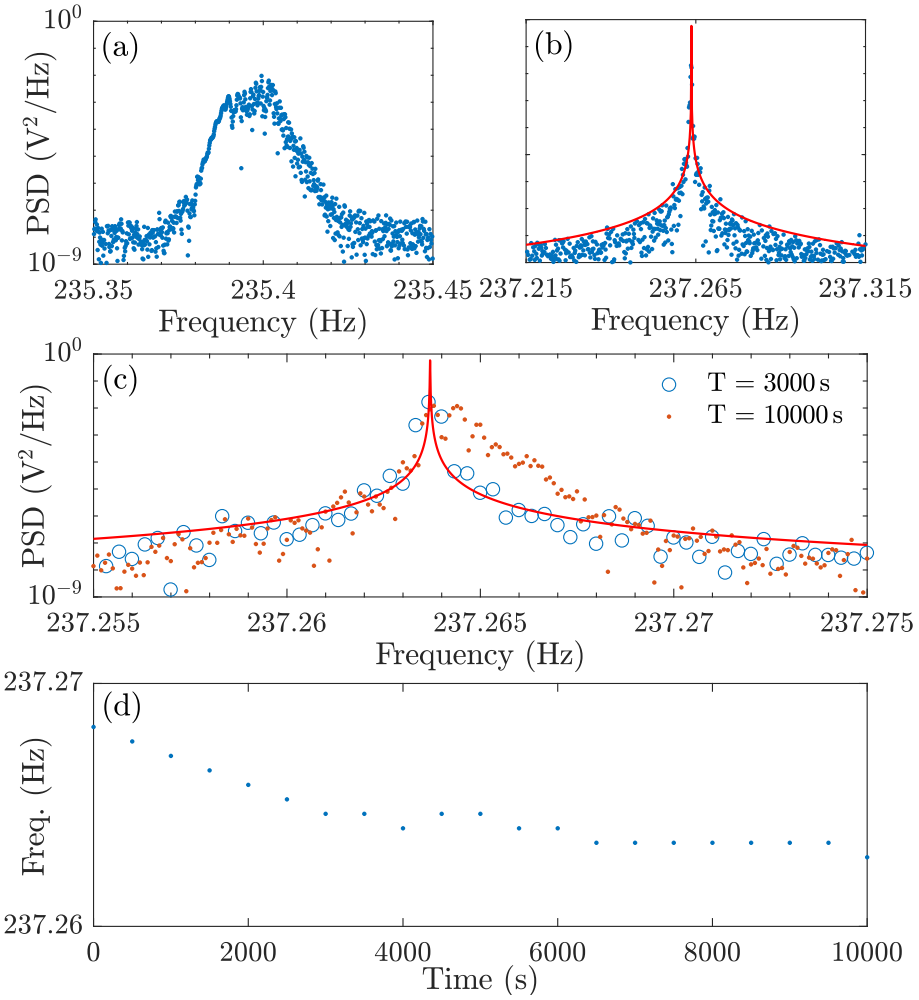


Figure 25: (a) Typical motional resonance without active current stabilization. (b) Typical motional resonance with active current stabilization. (c) Comparison of PSDs for different measurement lengths T with trap current feedback on. For short T the linewidth is determined by the spectral resolution 1/T and spectral leakage, while for longer T there is still linewidth broadening due to drifts in frequency. The solid line in (b) and (c) is a Lorentzian with the linewidth set by a ringdown measurement. (d) The resonance frequency drifts by around 5 mHz over three hours.

5.13 Sensing

Taking into account measurement noise, we can calculate the force sensitivity as

$$\sqrt{S_{FF}} = \sqrt{4k_B T_0 m\gamma + |\chi|^{-2} S_{nn}},$$

where $\sqrt{S_{nn}} \approx 1 \times 10^{-9}\,\mathrm{m}/\sqrt{\mathrm{Hz}}$ is the measurement noise and $\chi(\omega) = 1/[m(\omega_0^2 - \omega^2 - i\gamma\omega)]$ denotes the mechanical susceptibility. In our case, using $Q = 2.6 \times 10^7$ at 212 Hz and assuming $T_0 = 15\,\mathrm{mK}$, this would result in a force sensitivity of $\sqrt{S_{FF}} = 6.3 \times 10^{-19}\,\mathrm{N}/\sqrt{\mathrm{Hz}}$ on resonance, close to the thermal limit of $4.9 \times 10^{-19}\,\mathrm{N}/\sqrt{\mathrm{Hz}}$, and a noise equivalent temperature of $T_n = T_0 + |\chi(\omega_0)|^{-2} S_{nn}/(4k_B m\gamma) = 24\,\mathrm{mK}$ (cf. Fig. 26). However, due to the

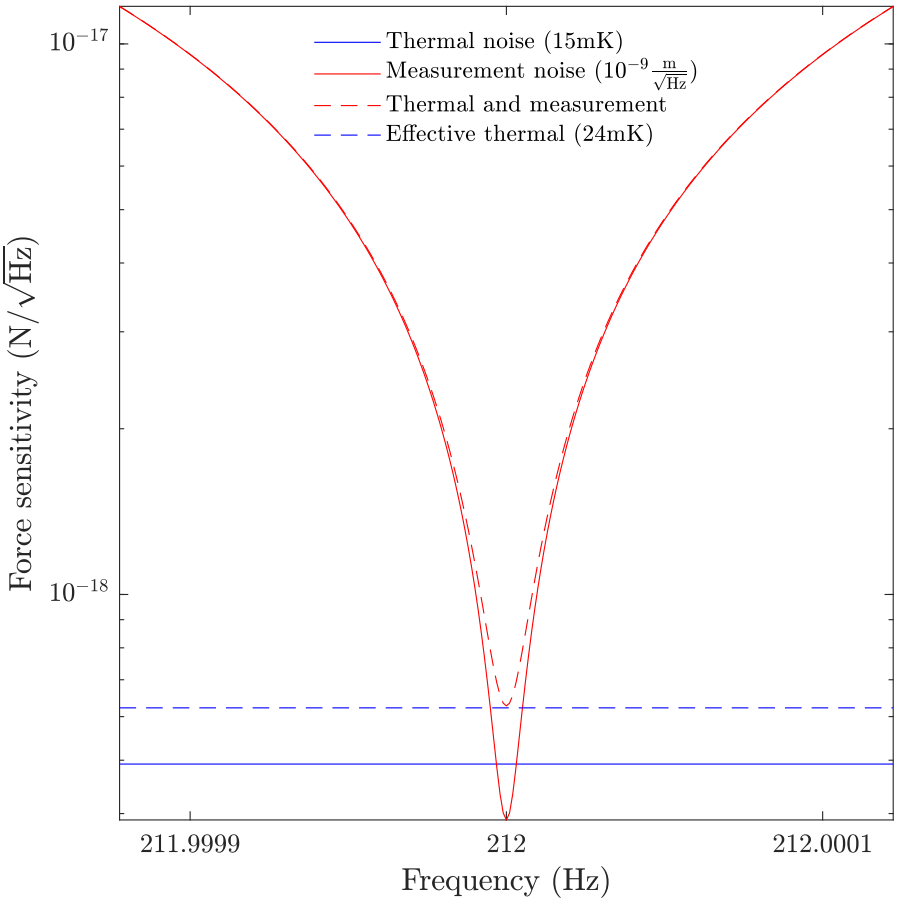


Figure 26: (a)Force sensitivity limits due to thermal noise and measurement noise. The parameters used for the plot are $Q = 2.6 \times 10^7$ and $f_0 = 212\,\mathrm{Hz}$.

stochastic frequency fluctuations described in the last section the susceptibility is stochastic as well. We briefly sketch how this reduces our sensitivity: Note that a measurement with frequency drifts can be approximated as a series of shorter measurements at different, but constant, resonance frequencies. For a finite measurement duration T the measured force power spectral density at resonance is approximately

$$4k_B T_0 m\gamma + S_{nn} \frac{\Delta f}{\int_{\Delta f} df |\chi(f)|^2},$$

where the integration runs over the bin width $\Delta f = \frac{1}{T}$ of the bin containing the resonance. Our force sensitivity thus becomes $\sqrt{S_{FF}} = \sqrt{4k_B T_0 m\gamma + |\chi|^{-2}_{avg} S_{nn}}$ with $|\chi|^2_{avg} = \frac{1}{\Delta f}\int_{\Delta f} df |\chi(f)|^2$. For $\Delta f > \frac{\gamma}{2\pi}$, we get $\frac{|\chi(f_0)|^2}{|\chi|^2_{avg}} \propto \frac{\Delta f}{\gamma}$. In our case this boosts the measurement noise above the thermal noise and, for a typical measurement, our force sensitivity worsens by at least an order of magnitude, corresponding to an noise equivalent temperature of at

least 2.5 K. Both improving the coupling, which corresponds to an effective decrease of the measurement noise, and improving the stability of the resonance frequency will allow us to perform measurements limited by thermal noise. We show below that we can increase the coupling by almost four orders of magnitude. Regarding the latter, we note that persistent current coils have reached a relative current stability better than 2×10^{-11}/h [VDFZS99].

5.14 Feedback

We can apply a magnetic feedback force on the levitated sphere by processing the SQUID signal and applying a feedback current to a small coil with approximately 20 windings positioned approximately 1 mm below the trap center. The feedback current generates an additional magnetic field, thereby shifting the field minimum of the trapping field and enabling us to apply direct feedback. The gradient of the trapping field is changed as well, such that we also have the possibility to apply parametric feedback at twice the particle's resonance frequencies. Since the COM modes are separated in frequency, we can apply feedback to all modes simultaneously. When we apply direct feedback, we pass the SQUID signal to a FPGA (STEMlab 125-14), which, for each of the mechanical frequencies, applies a bandpass-filter, gain and phase shift [NMC+17]. The resulting signals are then recombined on the FPGA and fed back to the feedback coil. When we apply parametric feedback at twice the mechanical frequencies we additionally use a phase-locked loop and a clock divider on a second FPGA. As described in the last section, our current noise floor corresponds to a noise equivalent temperature that is higher than the base temperature of our dilution refrigerator. This noise equivalent temperature also sets the limit for feedback cooling. Due to the large ambient noise reduction provided by our vibration isolation, magnetic shielding and trap current filter, the equilibrium temperature of the particle is below the noise equivalent temperature, meaning that even without applied feedback the particle's motion undergoes exponential decay until it is not detectable anymore. We thus cannot cool the particle's modes below their equilibrium temperature and use feedback currently only as a way to quickly adjust the amplitudes and prepare other measurements.

5.15 Characterization of the vibration isolation system

Our vibration isolation system consists of several cylindrical plates connected by straight wires, with the top plate mounted to the 4K-platform of the dilution refrigerator and the bottom plate mounted to the aluminum can containing the magnetic trap. Electrical and thermal connections going to the setup are loosely coiled up and guided to the setup via a separate vibration isolation stage hung from the Mixing Chamber platform (cf. Fig. 27). We first characterized a single stage at room temperature, by exciting it mechanically and recording its motion with a camera. We find that the horizontal and vertical resonance frequencies are $f_h = 1.1$ Hz and $f_v = 18.7$ Hz, respectively, while the librational resonance frequencies are $f_{l,1} = 0.6$ Hz (around vertical axis), $f_{l,2} = 8.7$ Hz and $f_{l,3} = 9.0$ Hz (around horizontal axes). We are thus limited by vertical vibrations, which in general couple to the other degrees of freedom as well [AMTM92]. We then assembled the setup as shown in Fig. 27, with the bottom plate mounted to an accelerometer (instead of the setup) used to measure acceleration along the vertical axis. The mass of the bottom plate (including the accelerometer) was 0.29 kg in this assembly. The intermediate stages are each supported by three wires of equal length, while the bottom stage is supported by a single wire. The wires are made from type 304 stainless steel with a diameter of $D = 38$ µm and a yield load of 0.37 kg, as specified by the manufacturer (Fort Wayne Metals). The wires are connected to the stages with clamping connections. The vertical spring constant for the i-th stage is given

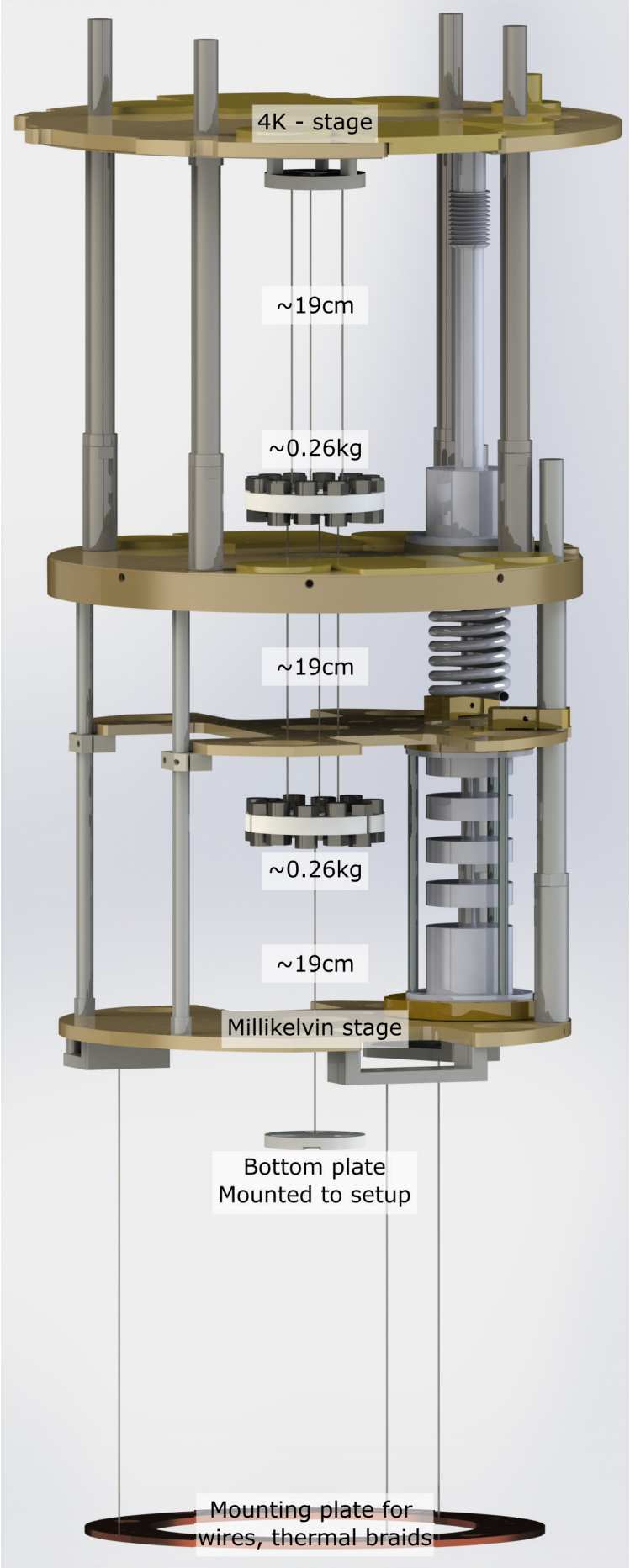


Figure 27: Model of the vibration isolation system.

by $k_{v,i} = (N_i Y D^2 \pi)/(4L_i)$, s.t. $f_{v,i} = 1/(2\pi)\sqrt{k_{v,i}/m_i}$ is the resonance frequency of a single stage. Here Y is the Young's modulus, N_i the number of supporting wires, L_i the wire length and m_i the mass of the stage. The normal mode frequencies $f_{n,i}$ of the assembled system are obtained by solving the characteristic equation of the system [AMTM92], resulting in the transfer function

$$\prod_{i=1}^{3} \frac{f_{v,i}^2}{|f_{n,i}^2 - f^2|}. \tag{36}$$

In Fig. 28 we compare the vibrations measured without vibration isolation (with the accelerometer mounted to the Mixing Chamber stage of the dilution fridge) and with vibration isolation. The highest normal mode frequency is approximately 30 Hz, above which the

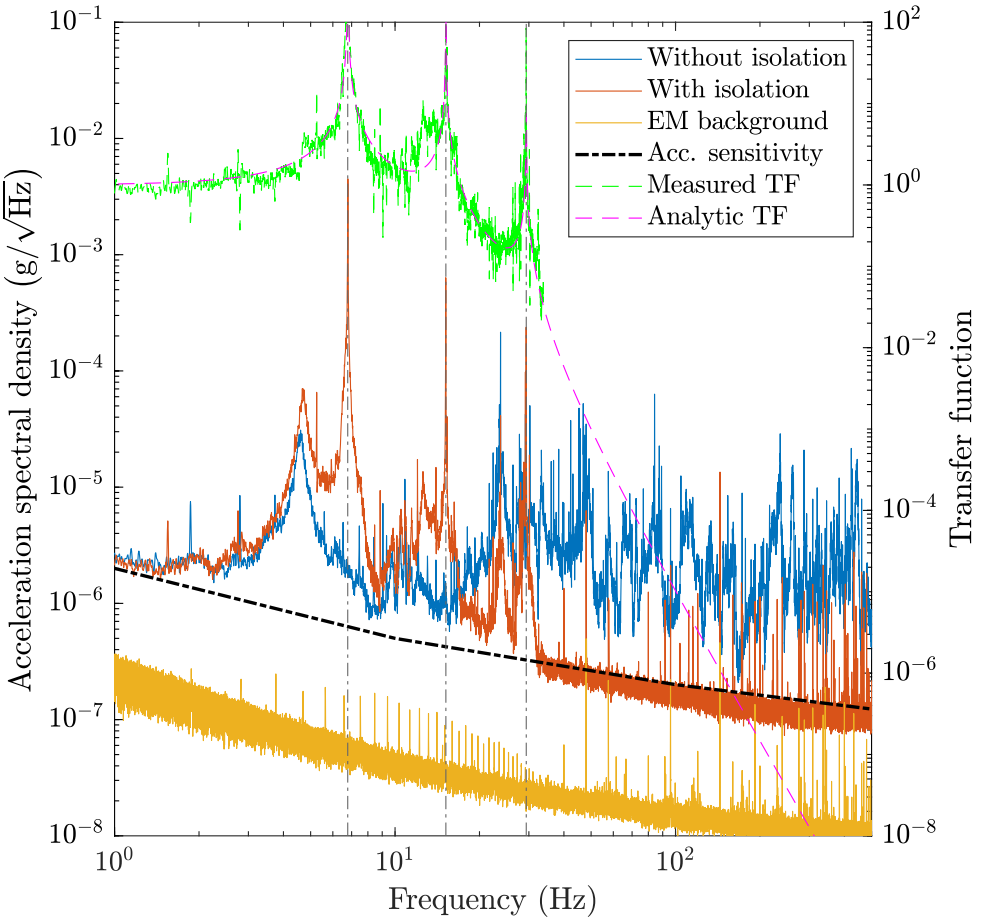


Figure 28: Characterization of the vibration isolation. The dash-dotted black line is the sensitivity of the accelerometer, as specified by the manufacturer. The solid orange and blue lines correspond to the measured acceleration with and without the vibration isolation, respectively, while the solid yellow line is data recorded with a 1 MΩ resistor connected to the SMA port inside the fridge. The dashed pink line is the analytic transfer function (Eq. 36), while the dashed green line is the measured transfer function, i.e. the ratio of the measured accelerations. The horizontal lines correspond to the normal mode resonance frequencies.

measured accelerations quickly drop below the sensitivity of the accelerometer, when it is mounted to the vibration isolation system. At lower frequencies the measured transfer function corresponds very well to the analytical values and we use the analytic expression to

extrapolate the attenuation at higher frequencies, resulting in an attenuation of 1×10^{-5} at 100 Hz and 1.5×10^{-7} at 200 Hz. The peaks at higher frequencies correspond to the electromagnetic background in the lab, which is verified by an independent measurement in which the accelerometer is replaced by an 1 MΩ resistor inside the fridge. This measurement reproduces the peaks at precisely the same frequencies as in the accelerometer measurement, although with a lower magnitude - this we attribute to the additional (unshielded) wiring going from the SMA port to the accelerometer, which can act as an antenna. In an initial approach we used different masses and wire lengths, such that the attenuation was approximately 5 orders of magnitude at 200 Hz.

5.16 Quality factor

In this section we estimate contributions to the dissipation due to gas damping and eddy currents. We also consider dissipation in the SQUID and flux creep in the pickup loop, which we rule out experimentally.

Collisions with background gas result in an additional damping of [HK90]

$$\gamma_P = \beta \frac{P}{\rho R \bar{v_{th}}},$$

where $\beta \approx 1.8$ and $\bar{v_{th}}$ is the mean thermal velocity of the molecules. We do not have a direct measure of the pressure at the trap location, but we can use the measured pressure at the room temperature side of the vacuum can, $P \approx 1 \times 10^{-6}$ mbar, to set an upper limit for the expected damping. Assuming the background gas consists mostly of Helium, we get $\gamma_P \approx 3 \times 10^{-7}\,\mathrm{s}^{-1}$, two orders of magnitude below the measured damping rates.

We avoid eddy current damping by not placing any normal conductors within the inner shield. Eddy currents can still be induced in conductors outside the shield, either via openings in the shield or via the pickup circuit, part of which is placed outside the shield. In the first case, we can estimate possible eddy current losses by imagining a conductive loop with resistance R_o and inductance L_o placed around the openings in the shield. The dissipation in mode $i \in \{x_0, y_0, z_0\}$ then takes a maximum value for $R_o = 2\pi f_i L_o$, corresponding to a damping

$$\gamma_i = \frac{(\partial_i \phi)^2}{2\pi m f_i L_o}.$$

Here ϕ denotes the flux in the loop induced by the oscillation of the sphere, which can be calculated from Eq. 35. Using the dimensions of our windows and estimating $L_o > 10$ nH for a similarly sized conductive loop, we get $\gamma_i < 1 \times 10^{-9}\,\mathrm{s}^{-1}$ for all modes.

We now consider eddy current damping mediated by the pickup circuit or damping due to flux creep in the pickup circuit, as well as dissipation in the SQUID due to a real part in the SQUID input impedance [MC85]. This implies $\gamma_i \propto \nu_i^2$, while in the experiment the damping is approximately equal for all three COM modes. In addition, during initial measurements the pickup loop was positioned farther from the trap center and coupling strengths were approximately one order of magnitude lower than the ones reported here, but we did not see any change in the quality factor.

5.17 Calibration

Our optical readout scheme is shown schematically in Fig. 29. The light source (Leica CLS150) produces a beam of light, which is further collimated by small windows in the cryostat and the magnetic shields. After passing through the cryostat, the light is focused

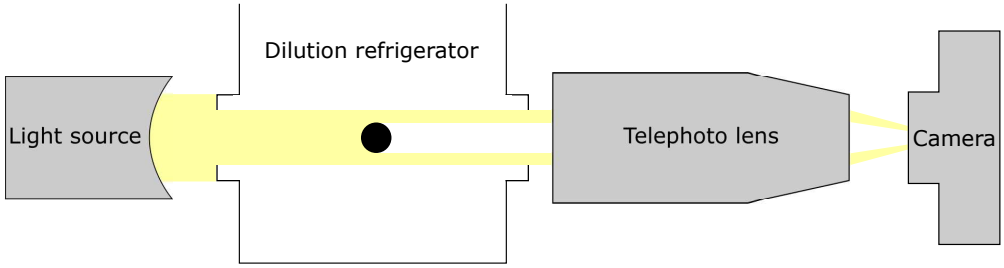


Figure 29: Sketch of the optical setup.

by a teleobjective into the camera (DFK 33UX287). Any object in the light path thus appears as a shadow on a bright background, corresponding to the projection of the object onto the image sensor. We use a frame rate of 596fps and 0.5ms exposure time to record the videos and then process them as follows. Each frame is first converted to grayscale, smoothed with Gaussian blurring, thresholded and then analyzed using the particle tracking software Trackpy [CG96]. This results in datasets for the horizontal and vertical (as defined by the camera's orientation) position of the sphere. The camera is aligned such that the vertical axis is along the trap coil axis and the direction of the particle's z-motion, while the particle's motion along x and y is projected onto the camera's horizontal axis. The trap coils are aligned such that the elliptic axes are at around 45° to the optical axis, so both the x and y motion can be imaged. To get separate trajectories for each mode we implement a digital bandpass filter around the respective resonance frequency. Calibration of the sphere's displacement relies on knowledge of the optical system's magnification, which we determine using knowledge of the sphere's size (100(6) µm, as specified by the manufacturer). Including the uncertainty from the alignment of the trap coils with respect to the optical axis in addition to the ±6 % uncertainty from the size of the sphere, we estimate a total uncertainty of ±13 % for the calibrated COM displacement.

The light source is turned on only for calibration measurements, as the illumination heats the particle and limits the levitation time to approximately one hour. Further, optical band-pass filters (approximately 400 nm – 650 nm) on the millikelvin stage reduce ambient light reaching the particle and heating it. Without the filters (and the light source turned off) levitation times are limited to around four hours, while we have not yet found a limit (>30 h) using the filters.

5.18 Optimizations and ground state cooling

In this section we provide more detail on how to implement the improvements that are necessary to perform feedback cooling to the ground state. We will consider only cooling of the z-mode, cooling of the other modes and 3D-cooling can be characterized and optimized in an analogous manner. We first show that the coupling strength can be increased by almost four orders of magnitude, s.t. the measurement noise (in units of $\mathrm{m}/\sqrt{\mathrm{Hz}}$) with a state-of-the-art SQUID decreases to $1 \times 10^{-15}\,\mathrm{m}/\sqrt{\mathrm{Hz}}$. We then take into account the back action from the SQUID due to the circulating current and determine the standard quantum limit (SQL) of our system. We proceed to evaluate the requirements for ground state cooling as well as contributions to heating from vibrations and frequency fluctuations.

5.18.1 Coupling strength

We can increase the coupling strength by better positioning of the pickup loop relative to the superconducting sphere and by increasing the number of turns of the pickup loop, thus

matching its inductance to that of the input coil. For the calculation, we will assume a planar pickup loop with circular windings, positioned coaxial with the z-axis. Then Eq. 35 leads to

$$\begin{aligned}\nu_1 = \quad & \pi b_z R_P^2 \left(\frac{R^2}{R_P^2+Z_P^2}\right)^{\frac{3}{2}} \\ & \times \left(1-\frac{R^2}{R_P^2+Z_P^2}\left(1-\frac{5Z_P^2}{R_P^2+Z_P^2}\right)\right)\end{aligned} \tag{37}$$

for the coupling strength w.r.t. a single turn of the pickup loop with radius R_P and z-position Z_P. The coupling strength to a multi-turn pickup loop can be written as a sum of terms of this form, $\nu = \sum_i \nu_1(R_{P,i}, Z_{P,i})$, and the coupling strength to the SQUID (cf. Fig. 30) is obtained as

$$\eta = \nu \frac{k\sqrt{L_I L_S}}{L_P + L_I + L_W}.$$

Here L_P, L_I and L_S are the inductances of pickup coil, SQUID input coil and SQUID,

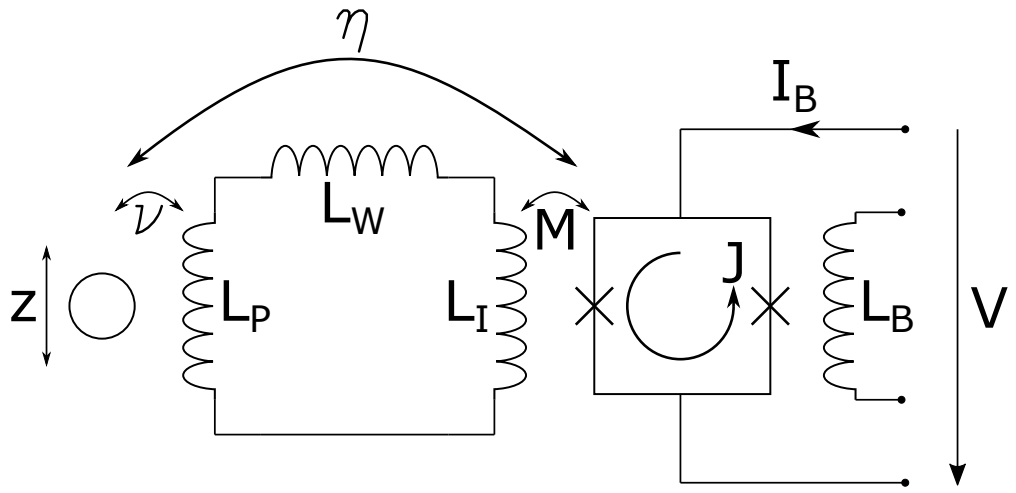


Figure 30: Schematic of the readout circuit. The working point of the SQUID is set by the bias current I_B and the bias flux coupled into the SQUID via L_B. For appropriate bias values and small changes in flux (in FLL mode this is assured by applying feedback over L_B), the voltage drop V is proportional to the flux in this SQUID loop.

respectively. We have used that the the mutual inductance M between input coil and SQUID can be written as $M = k\sqrt{L_I L_S}$ with $|k| < 1$. L_W denotes the stray inductance of the pickup circuit and is in our case dominated by the wires connecting the pickup coil to the SQUID, $L_W \approx 100nH$.

A relevant figure of merit for the measurement noise of the SQUID is the so-called energy resolution $S_{EE} = \frac{S_{\phi\phi}}{2L_S}$, with state-of-the-art SQUIDs reaching values on the order of $\hbar$ [ARK+88, CCTL98]. In terms of position resolution this can be written as

$$S_{nn} = \frac{S_{\phi\phi}}{\eta^2} = \frac{2S_{EE}}{k^2}\frac{(L_P+L_I+L_W)^2}{\nu^2 L_I}. \tag{38}$$

In order to get a realistic estimate for this we will use the SQUID parameters presented in [CCTL98], i.e. $L_S = 15\,\mathrm{pH}$, $L_I = 0.53\,\mu\mathrm{H}$, $M = 2.3\,\mathrm{nH}$ and $\frac{S_{\phi\phi}}{2k^2L_S} = 5.5\hbar$. For the pickup coil we assume a wire width of $0.3\,\mu\mathrm{m}$ and a distance between the wires of $0.45\,\mu\mathrm{m}$, which is also the resolution of the input coil of our existing SQUID. We use the modified Wheeler

formula [Whe28] to determine L_P, s.t. we get a fully analytical expression for S_{nn}. We also restrict us to $Z_P \geq R$. Given these parameters, as well as $b_z = 147\,\mathrm{T/m}$, we minimize S_{nn} with respect to R_P, Z_P and N, where R_P now denotes the inner radius of the pickup coil and N is the number of turns. This results in $\eta \approx 5.5 \times 10^7\,\phi_0/\mathrm{m}$ and $\sqrt{S_{nn}} \approx 1 \times 10^{-15}\,\mathrm{m}/\sqrt{\mathrm{Hz}}$ for $Z_P = R$, $R_P \ll R$ and $N \approx 87$. We note that the scaling of the coupling (Eq. 37) means that the measurement noise can be further decreased by working with higher gradients or using larger particles (a scale-independent expression for the coupling is easily obtained by measuring distance in units of R, magnetic fields in units of $b_z R$ and thus the coupling in units of $b_z R^2$).

5.18.2 The standard quantum limit

Equation 38 for the readout signal measured with the SQUID is valid only when the back-action stemming from the circulating SQUID current onto the levitating particle is negligible. This is a reasonable assumption given the weak coupling in our current setup, but for increased coupling strength the back-action should be considered. All relevant parameters are stated for the SQUID coupled to the input circuit and can be different than the parameters of the uncoupled SQUID, depending on the capacitive coupling at the Josephson frequency [MC85]. The readout noise is set by the flux noise, while the back-action noise is determined by fluctuations of the circulating current J. For a shunted SQUID the origin of both flux and current fluctuations is current noise in the shunt resistors and the quantum limit that arises from zero-point-fluctuations is $\sqrt{S_{\phi\phi}S_{JJ} - S_{\phi J}^2} \geq \hbar$ [KVHC81, DLZ83]. We will assume in the following that correlations between flux and current noise are negligible, $S_{\phi J} \approx 0$ [DLZ83, TC79].

A current J around the SQUID loop will effect a force $-\eta J$ on the levitated sphere and thus the measured displacement PSD of the sphere becomes

$$S_{zz}^m = \frac{S_{\phi\phi}}{\eta^2} + |\chi|^2(S_{FF}^{th} + \eta^2 S_{JJ}).$$

The product of measurement noise and back-action force noise thus fulfills the Heisenberg-like inequality $\frac{S_{\phi\phi}}{\eta^2}\eta^2 S_{JJ} \geq \hbar^2$ and S_{zz}^m is minimized for $\eta^2 = \frac{1}{|\chi|}\sqrt{\frac{S_{\phi\phi}}{S_{JJ}}}$, such that

$$S_{zz}^m = 2|\chi|\sqrt{S_{\phi\phi}S_{JJ}} + |\chi|^2 S_{FF}^{th}.$$

For $\sqrt{S_{\phi\phi}S_{JJ}} = \hbar$ this corresponds to the standard quantum limit.

5.18.3 Feedback cooling

We now assume we provide direct feedback s.t. the effective damping of the oscillator becomes $\gamma + \Gamma$, where Γ is the cold damping added by the feedback [PPB21] and $\tilde{\chi}(\omega) = 1/[m(\omega_0^2 - \omega^2 - i(\gamma + \Gamma)\omega)]$ is the effective susceptibility. The measurement noise will also enter the feedback system, resulting in an additional force, and the displacement power spectral density becomes

$$S_{zz} = |\tilde{\chi}|^2 \left(S_{FF}^{th} + \eta^2 S_{JJ} + (m\omega\Gamma)^2 \frac{S_{\phi\phi}}{\eta^2} \right).$$

For $\Gamma = \frac{\eta^2}{m\omega_0 \tilde{L_S}} \gg \gamma$ this corresponds a mean phonon number

$$\bar{n} = \frac{1}{\hbar\eta^2}\left(k_B T_0 m\gamma \tilde{L_S}\right) + \frac{1}{2}\left(\frac{\sqrt{S_{\phi\phi}S_{JJ}}}{\hbar} - 1\right),$$

where we have introduced the shorthand $\tilde{L_S} = \sqrt{\frac{S_{\phi\phi}}{S_{JJ}}}$. Close to the optimum working point $\tilde{L_S} \approx L_S$ [TC79]. Using $\eta = 5.5 \times 10^7\,\Phi_0/\mathrm{m}$ as well as assuming $T_0 = 15\,\mathrm{mK}$, $m = 5.6\,\mu\mathrm{g}$ and $L_S = 15\,\mathrm{pH}$, we need $\gamma \approx 1 \times 10^{-6}\,\mathrm{s}^{-1}$ to keep the left term negligible. Ground state cooling then requires $\sqrt{S_{\phi\phi}S_{JJ}} < 3\hbar$. While current noise in SQUIDs is challenging to measure [MC83], a DC-SQUID with $\sqrt{S_{\phi\phi}S_{JJ}} \approx 10\hbar$ has been reported [FBC+08]. Further, for $\tilde{L_S} \approx L_S$ we would expect $\sqrt{S_{\phi\phi}S_{JJ}} \approx 2S_{EE}$. The lowest energy resolution reported up to date is $S_{EE} \approx 1.7\hbar$ [ARK+88], so ground state cooling by continuous feedback will require a state-of-the-art SQUID.

5.18.4 Heating

We now consider fluctuations of the trap center with spectral density $S_{\epsilon\epsilon}$ as well as fractional fluctuations of the spring constant with spectral density $S_{\delta\delta}$. We note that the heating rate $\Gamma_\delta E$ due to frequency fluctuations is proportional to the energy E of the oscillator. The average energy of the oscillator is then described by

$$\langle \dot{E} \rangle = (\Gamma_\delta - \gamma)\langle E \rangle + k_B T_0 \gamma + \dot{Q}_\epsilon,$$

where $\dot{Q}_\epsilon$ is the heating rate due to fluctuations of the trap center. For $\Gamma_\delta < \gamma$ this results in an effective temperature of

$$T_{eff} = \frac{k_B T_0 \gamma + \dot{Q}_\epsilon}{k_B(\gamma - \Gamma_\delta)}.$$

The heating rates are given by [GOST98]

$$\dot{Q}_\epsilon = \frac{1}{4} m \omega_0^4 S_{\epsilon\epsilon}(\omega_0),$$

and

$$\Gamma_\delta = \frac{1}{4} \omega_0^2 S_{\delta\delta}(2\omega_0).$$

Using the values from the preceding paragraph, ground state cooling requires approximately $\sqrt{S_{\delta\delta}(2\omega_0)} < 1 \times 10^{-7}/\sqrt{\mathrm{Hz}}$ and $\sqrt{S_{\epsilon\epsilon}(\omega_0)} < 1 \times 10^{-19}\,\mathrm{m}/\sqrt{\mathrm{Hz}}$ (corresponding to $T_{eff} < 20\,\mathrm{mK}$). Regarding the former we note that relative fluctuations on the order of one part per billion can be reached in superconducting coils [BBS+16], while the latter requires further improvements to our vibration isolation system. Suspending the system from the top plate of the cryostat would allow us to add two more stages and achieve the required vibration suppression.

5.19 References

[AMTM92] T. L. Aldcroft, P. F. Michelson, R. C. Taber, and F. A. McLoughlin. Six-degree-of-freedom vibration isolation systems with application to resonant-mass gravitational radiation detectors. *Review of Scientific Instruments*, 63(8):3815–3827, 1992.

[ARK+88] D. D. Awschalom, J. R. Rozen, M. B. Ketchen, W. J. Gallagher, A. W. Kleinsasser, R. L. Sandstrom, and B. Bumble. Low-noise modular microsusceptometer using nearly quantum limited dc SQUIDs. *Applied Physics Letters*, 53(21):2108–2110, 1988.

[BBS+16] J. W. Britton, J. G. Bohnet, B. C. Sawyer, H. Uys, M. J. Biercuk, and J. J. Bollinger. Vibration-induced field fluctuations in a superconducting magnet. *Phys. Rev. A*, 93:062511, Jun 2016.

[CCTL98] P. Carelli, M. G. Castellano, G. Torrioli, and R. Leoni. Low noise multiwasher superconducting interferometer. *Applied Physics Letters*, 72(1):115–117, 1998.

[CG96] John C. Crocker and David G. Grier. Methods of digital video microscopy for colloidal studies. *Journal of Colloid and Interface Science*, 179(1):298–310, 1996.

[DLZ83] V. Danilov, K. Likharev, and A. Zorin. Quantum noise in squids. *IEEE Transactions on Magnetics*, 19(3):572–575, 1983.

[FBC+08] P. Falferi, M. Bonaldi, M. Cerdonio, R. Mezzena, G. A. Prodi, A. Vinante, and S. Vitale. $10\hbar$ superconducting quantum interference device amplifier for acoustic gravitational wave detectors. *Applied Physics Letters*, 93(17):172506, 2008.

[GOST98] M. E. Gehm, K. M. O'Hara, T. A. Savard, and J. E. Thomas. Dynamics of noise-induced heating in atom traps. *Phys. Rev. A*, 58:3914–3921, Nov 1998.

[HA19] J Hofer and M Aspelmeyer. Analytic solutions to the Maxwell–London equations and levitation force for a superconducting sphere in a quadrupole field. *Physica Scripta*, 94(12):125508, oct 2019.

[HK90] L. D. Hinkle and B. R. F. Kendall. Pressure-dependent damping of a particle levitated in vacuum. *Journal of Vacuum Science & Technology A*, 8(3):2802–2805, 1990.

[KVHC81] Roger H. Koch, D. J. Van Harlingen, and John Clarke. Quantum noise theory for the dc SQUID. *Applied Physics Letters*, 38(5):380–382, 1981.

[Liv63] J. D. Livingston. Magnetic properties of superconducting lead-base alloys. *Phys. Rev.*, 129:1943–1949, Mar 1963.

[MC83] J. Martinis and J. Clarke. Measurements of current noise in dc SQUIDS. *IEEE Transactions on Magnetics*, 19(3):446–448, 1983.

[MC85] John M. Martinis and John Clarke. Signal and noise theory for a dc SQUID amplifier. *Journal of Low Temperature Physics*, 61(3):227–236, Nov 1985.

[NMC+17] L. Neuhaus, R. Metzdorff, S. Chua, T. Jacqmin, T. Briant, A. Heidmann, P.-F. Cohadon, and S. Deléglise. PyRPL (Python Red Pitaya Lockbox) — An open-source software package for FPGA-controlled quantum optics experiments. In *2017 Conference on Lasers and Electro-Optics Europe European Quantum Electronics Conference (CLEO/Europe-EQEC)*, pages 1–1, 2017.

[PPB21] T. W. Penny, A. Pontin, and P. F. Barker. Performance and limits of feedback cooling methods for levitated oscillators: A direct comparison. *Phys. Rev. A*, 104:023502, Aug 2021.

[TC79] Claudia D. Tesche and John Clarke. dc SQUID: Current noise. *Journal of Low Temperature Physics*, 37(3):397–403, Nov 1979.

[VDFZS99] R. S. Van Dyck, D. L. Farnham, S. L. Zafonte, and P. B. Schwinberg. Ultrastable superconducting magnet system for a penning trap mass spectrometer. *Review of Scientific Instruments*, 70(3):1665–1671, 1999.

[Whe28] H.A. Wheeler. Simple inductance formulas for radio coils. *Proceedings of the Institute of Radio Engineers*, 16(10):1398–1400, 1928.

6 A numerical approach to levitated superconductors and its application to a superconducting cylinder in a quadrupole field

When I calculated the analytical solutions for a superconducting sphere in a quadrupole field published in [HA19], I also conducted early investigations of non-spherical superconductors and found that some shapes resulted in significantly higher trap frequencies and coupling strengths than those that can be obtained with a superconducting sphere. In addition, such shapes would provide access to librational and/or rotational degrees of freedom, which could lead both to practical applications (torque sensing) and grant access to quantum phenomena that are not present for the c.o.m. motion (e.g. quantized angular momentum states) [SHK21].

However, finding the field distribution around an arbitrarily shaped superconductor is not straightforward. The analytical method for calculating the magnetic field distribution around a superconducting sphere in a quadrupole field [HA19] can be generalized to almost arbitrary fields, but only to some non-spherical geometries. Analytical results for some other geometries (rings, ellipsoids) are known [NMTS21, BSCSDV+24], but the methods used to obtain them also cannot be generalized to arbitrary shapes.

A practical solution circumventing the difficulties of finding analytical solutions is to use finite element simulations, which numerically solve the equations on a discretized space. These simulations can provide numerical solutions for the field distribution around arbitrarily shaped superconductors. However, simulations are often difficult to setup reliably, need a lot of computing power and the results are hard to verify.

In the following publication I present a numerical model for the purpose of finding the field distribution around arbitrarily shaped superconductors, which is not resource intensive and can be run on a typical personal computer. The model is written in MATLAB and uses COMSOL MULTIPHYSICS for the finite element simulations. I verify the accuracy of the model by performing simulations of a superconducting sphere and comparing the results to the analytical solution.

I use this model to evaluate the trap parameters for a cylinder in a quadrupole field and find that, using a cylinder of suitable aspect ratio, one can obtain substantially higher trap frequencies and coupling strengths compared to a spherical superconductor. W.r.t. ground state cooling, this significantly lowers the demands on vibrational and thermal noise. More generally, this highlights that one can benefit by choosing a geometry suitable to the purpose of one's experiment.

A numerical approach to levitated superconductors and its application to a superconducting cylinder in a quadrupole field

J. Hofer[1,2]

[1]Faculty of Physics, Vienna Center for Quantum Science and Technology (VCQ), University of Vienna, A-1090 Vienna, Austria
[2]Institute for Quantum Optics and Quantum Information (IQOQI), Austrian Academy of Sciences, A-1090 Vienna, Austria

This is the author's accepted version of this work. The definite version was published in *Physica Scripta* "A numerical approach to levitated superconductors and its application to a superconducting cylinder in a quadrupole field" volume 99, number 19, DOI 10.1088/1402-4896/ad6bcf.

Abstract

Magnetically levitated superconductors in the Meissner state can be utilized as micro-mechanical oscillators with large mass, high quality factors and long coherence times. In previous works analytical solutions for the magnetic field distribution around a superconducting sphere in a quadrupole field have been found and used to derive the trap parameters, while non-spherical geometries have only been investigated in a few idealized cases. However, superconductors of almost arbitrary shape can be used as levitators in a magnetic trap and, as the trap's properties depend strongly on the superconductors shape, allow for a wider parameter regime to be accessed. Finite element models are suitable to obtain the field distribution around arbitrarily shaped superconductors in arbitrary fields, but have not yet been used widely in the context of levitated superconductors. Here we present a simple numerical model for this purpose and use it to calculate the field distribution around cylindrical superconductors in a quadrupole field and to evaluate the trap parameters. We find that the cylindrical shape, compared to spherical levitators, allows for substantially higher trap frequencies and coupling strengths. This in turn reduces the demands on vibration isolation and significantly eases the requirements for feedback cooling to the ground state. The numerical model is provided in a file repository and can easily be adapted to various geometries and trap fields.

6.1 Introduction

Magnetically levitated superconductors are already well established as accelerations sensors, most notably in the superconducting gravimeter [Goo99], which uses centimeter sized hollow spheres coated with Niobium. More recent proposals [RICN+12, PPCS+18] and experimental advances [VFG+20, HGH+23] have shown the potential of using much smaller magnetically levitated particles for approaching the quantum regime with massive, micrometer-sized particles. We believe that the most promising approach is the levitation of a type-I superconductor in the field produced by persistent currents, as this avoids non-fundamental sources of dissipation and decoherence which are present in other levitation schemes [HGH+23]. For spherical superconductors analytical solutions for the magnetic field distribution, which allow the accurate prediction of the magnetic trap's properties, exist [HA19] and are in good agreement with experimental results [HGH+23]. For non-spherical superconductors analytical solutions have been found for a few idealized cases, in particular thin rings [NMTS21] and ellipsoids [BSCSDV+24], and the results indicate that the trap parameters are strongly dependent on the shape of the superconductor and that non-spherical superconductors might allow access to trap parameters that are not attainable with spheres. Furthermore, non-spherical particles possess librational degrees of freedom, which exhibit properties that are not present for the center-of-mass motion [SHK21]. Here we present a numerical model for calculating the field distribution and resulting trap properties for a cylindrically shaped superconductor in a quadrupole field. The simulations are written in MATLAB and use COMSOL MULTIPHYSICS for the numerical evaluation. The model is resource friendly and can be run on a typical personal computer. All files are provided in a repository and can easily be modified to evaluate various superconducting geometries (e.g. dumbbells, cuboids). We test the numerical model by computing the field distribution for a spherical superconductor and comparing it to the analytical values, details on this are provided in the appendix.

6.2 Model

We consider a quadrupole trap, such that the applied field is of the form $\mathbf{B_0}(\mathbf{x}) = (b_x x, b_y y, b_z z)$ and, without loss of generality, assume $|b_x| \leq |b_y| < |b_z|$. Since the b_i are related by $b_z = -(b_x + b_y)$ (from $\nabla \mathbf{B_0} = 0$) we can choose a parameter ϵ with $0 \leq \epsilon < 1$ such that

$$\mathbf{B_0}(\mathbf{x}) = \frac{1}{2} b_z \left((1-\epsilon)x, (1+\epsilon)y, -2z\right). \tag{39}$$

We consider only the case where the cylinder's radius R and height H are both much larger than the superconducting penetration depth λ, s.t. $\lambda \to 0$ is a good approximation and the magnetic field vanishes inside the cylinder [HA19]. Outside of the cylinder we can introduce a scalar potential Φ such that

$$\mathbf{B} = \mathbf{B_0} - \nabla\Phi \quad \text{and} \quad \Delta\Phi = 0. \tag{40}$$

The magnetic field distribution B around the cylinder is determined by

$$\mathbf{B} \xrightarrow{|\mathbf{x}|\to\infty} \mathbf{B_0} \tag{41}$$

and the boundary condition

$$\mathbf{n} \cdot \mathbf{B} = 0 \tag{42}$$

on the cylinder's surface, where $\mathbf{n}$ is the surface normal vector. The position and orientation of the cylinder relative to the field are described by Euler angles in the ZYX convention (the

capital letters denote the intrinsic axes, co-rotating with the cylinder) and a displacement vector. Starting from a position where the cylinder's c.o.m. is coincident with the origin of the coordinate system and the cylinder is coaxial w.r.t. the z-axis, we first rotate the cylinder by an angle α around the Z-axis (which initially coincides with the z-axis) and then by an angle β around the Y-axis. Finally we displace the cylinder's c.o.m. by $\mathbf{x_0}$ (cf. Fig. 31a). The third angle, γ, which corresponds to a rotation around the X-axis, is not needed to describe the position, but will be used further below in the context of the librational modes. The setup of the COMSOL simulations is shown in Fig. 31b. For the simulations we use the intrinsic coordinate system aligned with the cylinder, such that

$$\mathbf{B_0} \to R_Y^{-1}(\beta) R_Z^{-1}(\alpha) \mathbf{B_0} \left(R_Z(\alpha) R_Y(\beta)(\mathbf{x} + \mathbf{x_0})\right)$$

with

$$R_Y(\beta) = \begin{pmatrix} cos(\beta) & 0 & sin(\beta) \\ 0 & 1 & 0 \\ -sin(\beta) & 0 & cos(\beta) \end{pmatrix}$$

and

$$R_Z(\alpha) = \begin{pmatrix} cos(\alpha) & -sin(\alpha) & 0 \\ sin(\alpha) & cos(\alpha) & 0 \\ 0 & 0 & 1 \end{pmatrix}.$$

The cylinder is thus always at the center of the spherical simulation domain and constitutes its inner boundary. This setup allows us to reuse the same mesh for all simulations with the same radius and height, reducing meshing times. In the outermost shell of the simulation domain, the distance between mesh elements is scaled such that the boundary condition is set at a distance much larger than any characteristic scale of the superconductor (effectively at infinity). We then use COMSOL to numerically solve Eq. 40 for the scalar potential in the simulation domain with the boundary conditions (41, 42) on the inner and outer boundary, respectively. Note that the superconducting cylinder is modeled only via the boundary condition Eq. 42, meaning that the volume of the cylinder is not part of the simulation and there is no domain corresponding to it in COMSOL. The size of the simulation domain is somewhat arbitrary: If the outer boundary is too close to the cylinder, this introduces numerical errors (cf. Appendix A), but increasing the size of the domain increases the number of mesh elements (for the same mesh resolution) and thus computation times; the same considerations also apply to the thickness of the outer shell. We used a radius of 1.5 R for the simulation domain and a thickness of 0.15 R for the shell in most simulations.

Since the set of equations (39 - 42) is scale invariant both w.r.t. length and the magnetic gradient b_z, it follows that the solution is (up to rescaling) independent of b_z and depends only on the ratio $\frac{H}{R}$, i.e.

$$\mathbf{B}\left(b_z, R, H, \mathbf{x_0}, \mathbf{x}\right) = b_z R \, \mathbf{B}\left(1, 1, \frac{H}{R}, \frac{\mathbf{x_0}}{R}, \frac{\mathbf{x}}{R}\right). \tag{43}$$

It is thus sufficient to solve for a fixed value of b_z and e.g. R, we subsequently use $b_z = 1\,\mathrm{T/m}$ and $R = 1\,\mathrm{m}$. This corresponds to measuring length in units of R and magnetic field strength in units of $b_z R$.

Having obtained the field distribution, we can calculate the force and torque acting on the cylinder as

$$\mathbf{F} = \frac{1}{\mu_0} \oiint dS \, \left[(\mathbf{nB})\mathbf{B} - \frac{1}{2}\mathbf{nB}^2\right] \tag{44}$$

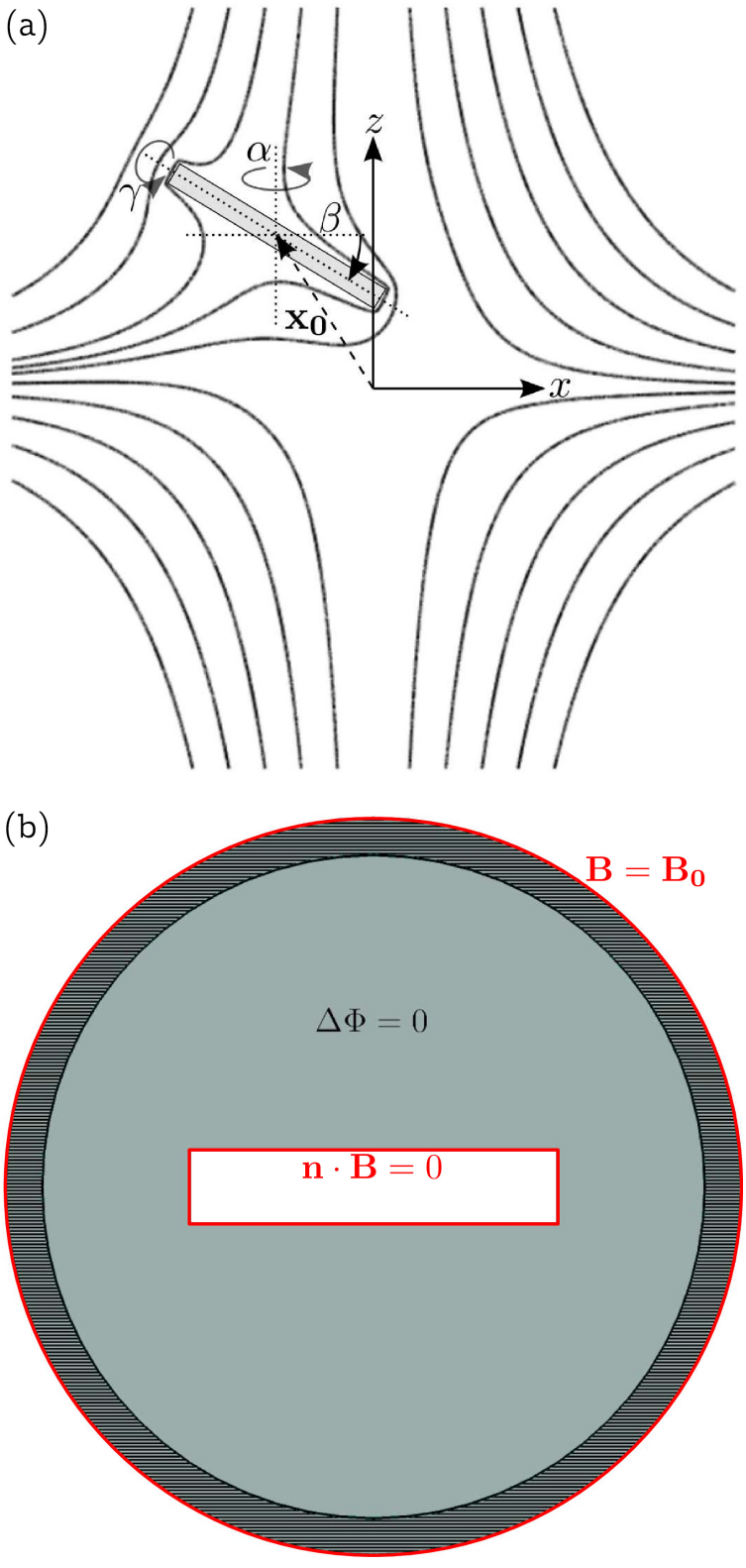


Figure 31: (a)Sketch of the system. The quadrupole field is depicted by its field lines in the xz-plane. (b)Geometrical setup of the COMSOL simulation. In the spherical simulation domain (grey) the equation $\Delta\Phi = 0$ is solved numerically, with the boundary conditions being set on the inner and outer boundaries of the domain (red), as described in the text. In the outer shell of the simulation domain (striped pattern) distances between mesh elements are scaled.

and

$$\mathbf{T} = \frac{1}{\mu_0} \oiint dS \left[\mathbf{x} \times \left((\mathbf{nB})\mathbf{B} - \frac{1}{2}\mathbf{nB}^2 \right) \right], \tag{45}$$

where the integration runs over the surface of the cylinder and $\mathbf{n}$ denotes the surface normal vector. These integrals can be numerically calculated within COMSOL, the force and torque are then directly available for further processing or plotting in MATLAB.

Note that sharp edges as used in this simulation are, in principle, unphysical, as in reality the field can always penetrate any physical superconductor to a length on the order of the penetration depth. Indeed, the maximum surface field on the superconductor diverges when a sharp edge is used (analogous to how the magnetic field strength on the surface of a thin wire tends to infinity when the wire size is decreased). We compare the results to a simulation using rounded edges with a finite radius R_{edge} as well as to a simulation of the full Maxwell-London equations taking into account the penetration depth λ of the superconductor and show that the results for these cases converge to the results obtained using sharp edges for $R_{edge} \to 0$ respectively $\lambda \to 0$ (more details are provided in the appendix). The model with sharp edges is thus suitable to investigate the general behavior, in practice we recommend using an edge radius corresponding to experimental parameters. Note that the simulations of the full Maxwell-London equations are computationally much more expensive and impractical to run on a typical personal computer, which is why we chose the approach using the scalar potential for the majority of the simulations.

6.3 Equilibrium positions

Intuitively, and loosely speaking, we would expect that the equilibrium positions occur when the least amount of applied field is displaced by the superconductor. Since the gradient of the applied field is highest among the z-axis and lowest along the x-axis, this would correspond to an equilibrium position of $\mathbf{x_0} = 0$, with $\beta = 0$ for "flat" (small $\frac{H}{R}$) cylinders and $\alpha = 0, \beta = \frac{\pi}{2}$ for "long" (large $\frac{H}{R}$) cylinders, and our work would be only to find the transition point between "flat" and "long" cylinders as well as to determine the quantitative values for the field distribution (and the quantities derived thereof). Although we will see these positions are indeed global energy minima (and thus stable equilibria), the full picture turns out to be more complex. Not only are there additional equilibrium positions associated with local energy minima, but during the transition from "flat" cylinders to "long" cylinders there occur a range of intermediate positions with (α, β) going from $\left(\frac{\pi}{2}, 0\right)$ to $\left(0, \frac{\pi}{2}\right)$. We will now describe the procedure used to find these equilibria and then provide a quantitative description of the results.

We use a modified gradient descent method to find the equilibrium positions. The main modification to a standard gradient descent is that we obtain the force and torque from a numerical surface integration over the fields (Eqs. 44, 45) rather than numerically calculating the gradient of the magnetic energy (which would require an additional simulation for each degree of freedom to obtain the derivative). For each aspect ratio, we perform the gradient descent for multiple starting points to find the distinct equilibria; an overview of the stable equilibrium positions obtained in this way is shown in Fig. 32. The c.o.m. position is always $\mathbf{x_0} = 0$, so the equilibrium positions differ only in α and β. Due to the mirror symmetry of the applied field (w.r.t. the xy, xz and yz planes) the mirrored configurations also correspond to stable equilibria. Note that for $\epsilon = 0$ the cylinder is not constrained at all w.r.t. rotations around the z-axis (as the field is radially symmetric), i.e. in that case α can take any value and the equilibria are determined only by the value of β.

For simplicity we have chosen not to include the gravitational force into this analysis, which would shift the equilibrium position to $\mathbf{x_0} \neq 0$, where the precise value of the new

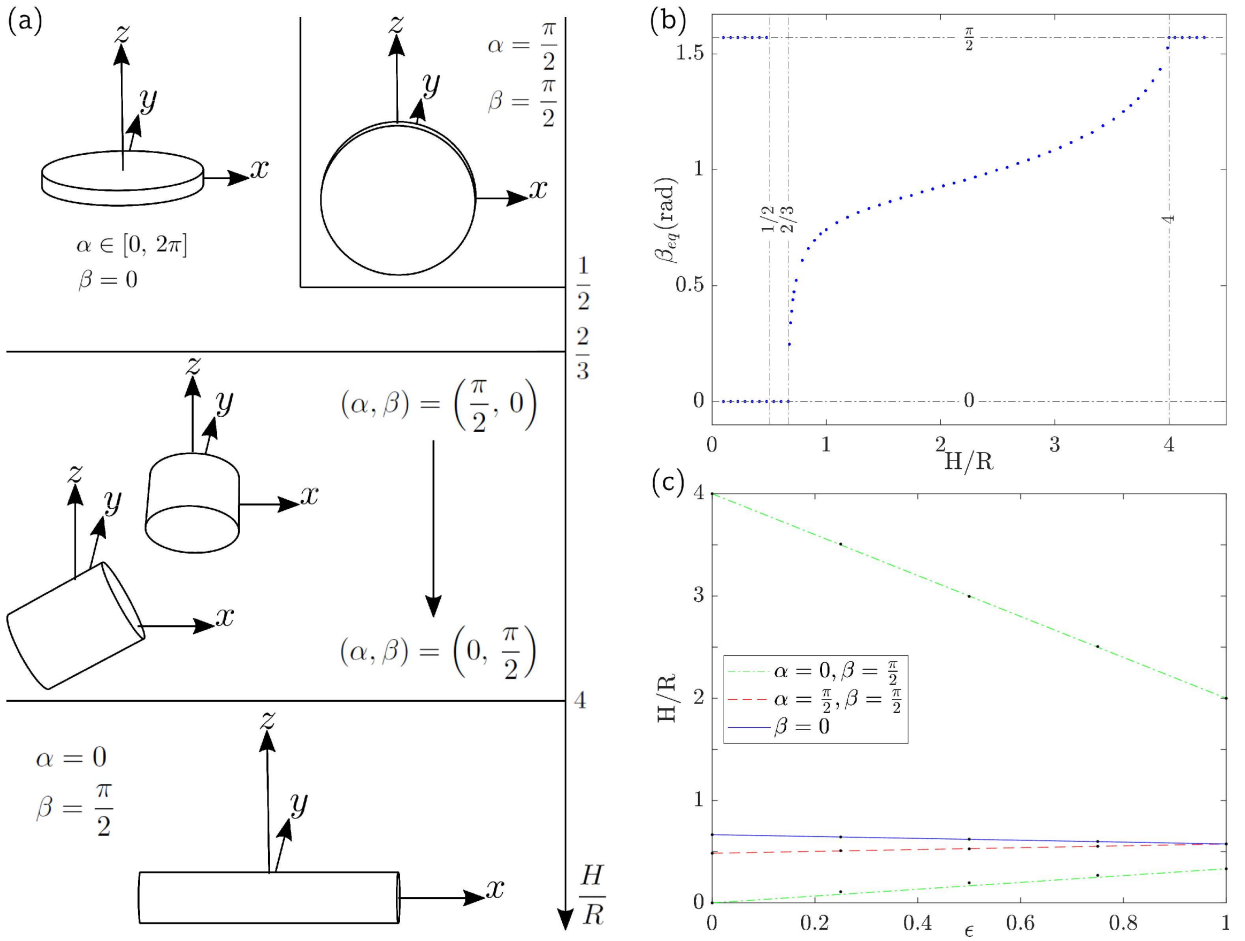


Figure 32: (a)Schematic overview of the different stable trap positions for a superconducting cylinder in a quadrupole trap. For $\epsilon = 0$ the cylinder is free to rotate around the z-axis and the equilibrium positions is determined solely by β. Note that the orientation $\alpha = 0, \beta = \frac{\pi}{2}$ also results in a stable equilibrium for very small $\frac{H}{R}$ (approximately $\frac{H}{R} < \frac{1}{3}\epsilon$), this is not explicitly shown in the figure. The values for the transition between the different stable orientations shown on the right-hand-side are approximate for $\epsilon = 0$. (b)For $\epsilon = 0$ the equilibrium position of the cylinder is determined solely by β. The transition points are marked by the vertical lines. For small $\frac{H}{R}$ two stable equilibria exist. (c)ϵ-dependence of the transition points between the stable equilibria, as described in the text.

equilibrium position depends on the axis of gravity, the gradient of the field and the aspect ratio as well as the density of the cylinder. In general the inclusion of gravity can alter the equilibrium orientation and the corresponding frequencies. Depending on the parameters, these modifications may or may not be negligible. In practice, when planning an experiment or evaluating the results of one, I recommend including gravity in the analysis with the parameters corresponding to the experimental setup. For small $\frac{H}{R}$ a stable orientation is given by $\beta = 0$, while for large $\frac{H}{R}$ the stable orientation is $\alpha = 0, \beta = \frac{\pi}{2}$. In between the orientation changes continuously (cf. Fig. 32b) from $\alpha = \frac{\pi}{2}, \beta = 0$ to $\alpha = 0, \beta = \frac{\pi}{2}$. The exact ratio, at which the transition between the different equilibrium positions occurs, depends on ϵ (Fig. 32c), the values stated on the right-hand-side of Fig. 32 are approximate for $\epsilon = 0$.

Note that for $\frac{H}{R} \lessapprox \frac{1}{2}$ a second equilibrium position exists for $\alpha = \frac{\pi}{2}, \beta = \frac{\pi}{2}$ and for $\frac{H}{R} \lessapprox \frac{1}{3}\epsilon$ there is a third equilibrium at $\alpha = 0, \beta = \frac{\pi}{2}$. This might seem counter-intuitive, since the field gradient is steepest along the z-axis. However, some intuition can be gained from thinking about the way the original field is disturbed by the presence of the superconductor. When the cylinder's flat edges are parallel to the xz- or yz-plane, the field disturbance is comparatively small (cf. Fig. 33a). However, if the cylinder is tilted slightly, the disturbance is much larger (cf. Fig. 33b). It thus makes sense that these orientations result in local energy minima (cf. Fig. 33c), as the energy is proportional to the volume integral over the squared magnetic field norm.

In Fig. 34 we plot the torque on the cylinder as a function of the angle β for various aspect ratios and $\alpha = \frac{\pi}{2}$, $\epsilon = 0$. The linear component of the torque around the rest positions vanishes at the transition points (e.g. $\frac{H}{R} = \frac{2}{3}$), so in this case there is no harmonic trapping potential. In the subsequent sections we will focus on the case $\frac{H}{R} \lessapprox \frac{2}{3}, \beta = 0$: We have found that this is the position that results in the highest trapping frequencies for the center-of-mass motion along the z-axis as well as the highest ratios of coupling strength to mass, which is relevant for feedback cooling [PPB21].

6.4 Trap frequencies

For small displacements around the equilibrium position $\beta = 0$ the motion of the cylinder can be characterized by five normal modes, three for the center of mass motion along the x, y and z axes and two librational modes corresponding to rotations around the axes x and y. For simplicity we restrict ourselves to the case where the cylinder does not rotate around its symmetry axis ($\dot{\alpha} = 0$) and, without loss of generality, set $\alpha = 0$ (i.e. β and γ characterize the librational modes).

The frequencies are then calculated numerically as

$$f_i = \frac{1}{2\pi}\sqrt{\frac{1}{m}\frac{F_i(i_0 = 0.01\,\mathrm{R}) - F_i(i_0 = 0)}{0.01\,\mathrm{R}}}$$

with $i \in \{x, y, z\}$ for the translational modes and

$$f_j = \frac{1}{2\pi}\sqrt{\frac{1}{I}\frac{T_j(j_0 = \frac{\pi}{100}) - T_j(j_0 = 0)}{\frac{\pi}{100}}}$$

with $j \in \{\beta, \gamma\}$ for the librational modes. Here m refers to the mass of the cylinder and $I = \frac{1}{12}m\left(3 + \left(\frac{H}{R}\right)^2\right)$ to the moment of intertia around the x-axis (or the y-axis, as the moment of intertia is the same in both cases). The reason for the choice of displacements is as follows: For the librational modes we found that a rotational displacement of $\frac{\pi}{100}$ is small enough s.t. the torque around the equilibrium position is still linear to an excellent

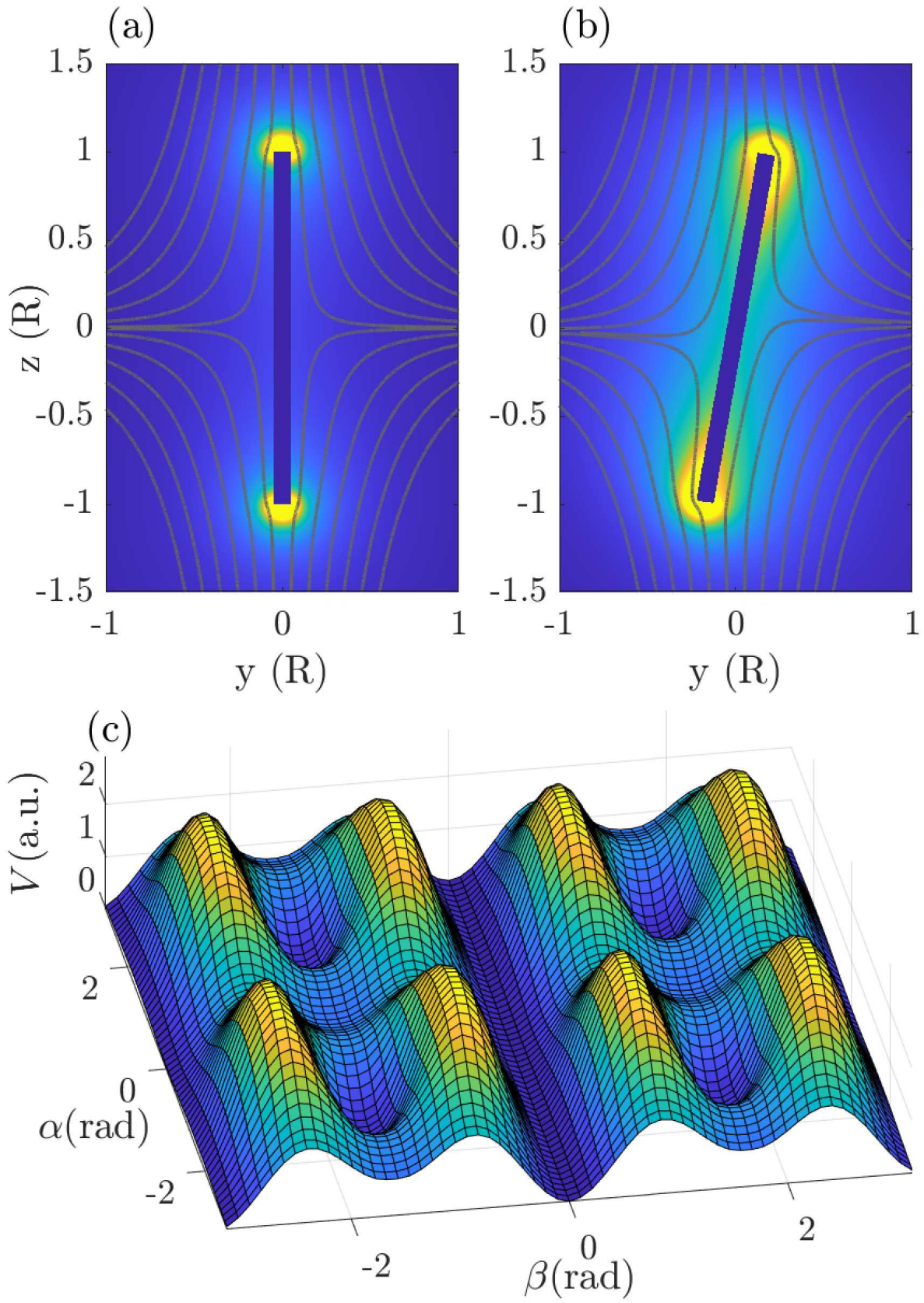


Figure 33: (a,b)Comparison between a cylinder with $H/R = 0.1$ in (a) the equilibrium position $\alpha = \frac{\pi}{2}, \beta = \frac{\pi}{2}$ and (b) slightly tilted away from the equilibrium position. The field lines of $\mathbf{B}$ in the yz-plane as well as the field norm of the induced field $\mathbf{B} - \mathbf{B_0}$ are displayed, brighter colors correspond to higher fields. (c)Magnetic energy w.r.t. α, β for a cylinder with $H/R = 0.1$ and $\epsilon = 0.75$. The stable equilibria correspond to the local minima of the energy.

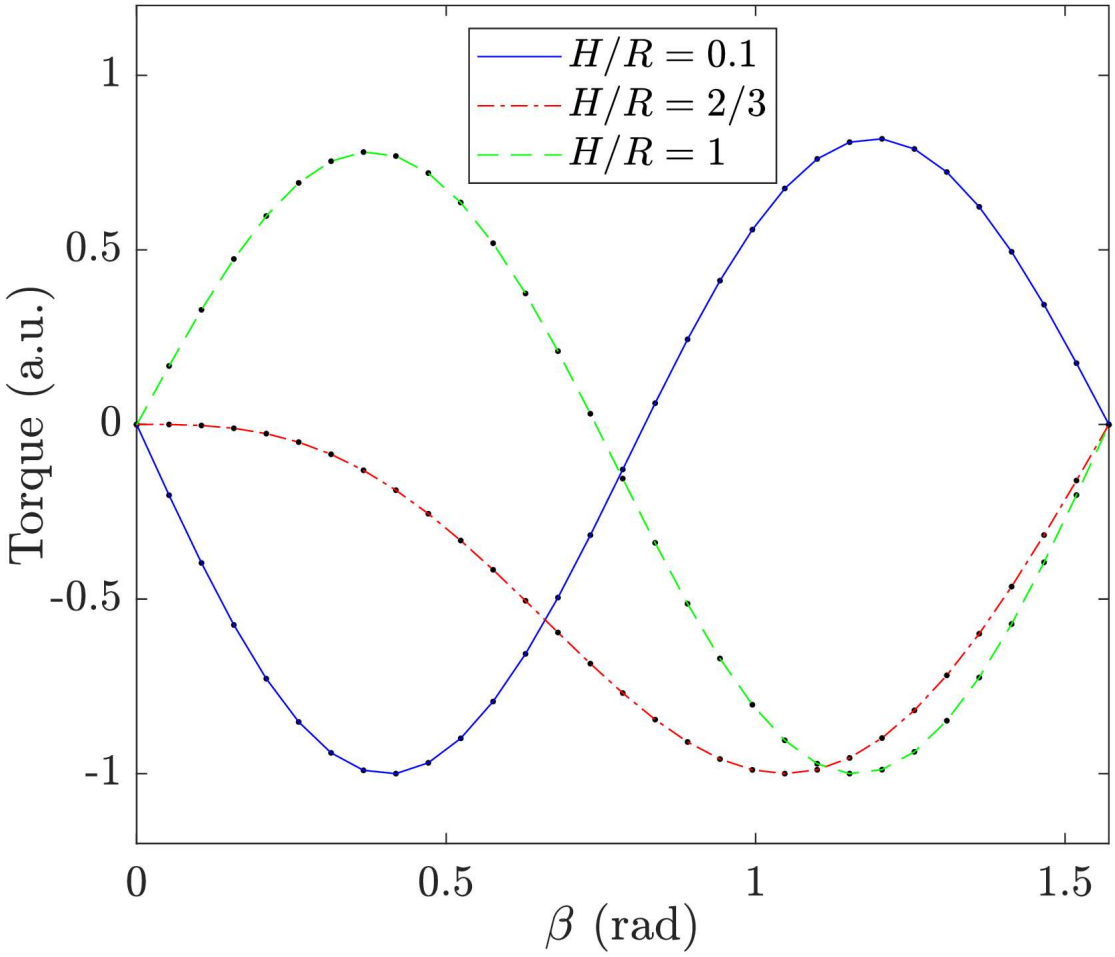


Figure 34: Torque on the cylinder for various aspect ratios and $\alpha = \frac{\pi}{2}$, $\epsilon = 0$. For $\frac{H}{R} = \frac{2}{3}$ the harmonic potential vanishes. Each curve was scaled for visibility.

approximation (cf. Fig. 34), but it is also large enough to ensure that the result is not obscured by numerical errors (cf. Appendix A). For the translational modes, F_i is linear in i for arbitrary large displacements, so the precise value for the displacement used in the calculation of the frequency does not matter.

In Fig. 35 we plot the frequencies f_x, f_z, f_β for $\epsilon = 0$, in which case the x- and y-mode as well as the β- and γ-mode are degenerate. The inset shows the dependence of these modes on epsilon for $\frac{H}{R} = 0.2$. To plot relatable numbers we have assumed a density of $8570\,\mathrm{kg/m^3}$ (corresponding to the density of Niobium) and a field gradient $b_z = 500\,\mathrm{T/m}$. For comparison, the dashed line displays the frequencies $f_{x,S}, f_{z,S}$ for a superconducting sphere [HA19] using the same parameters. Note that the center-of-mass frequency for the

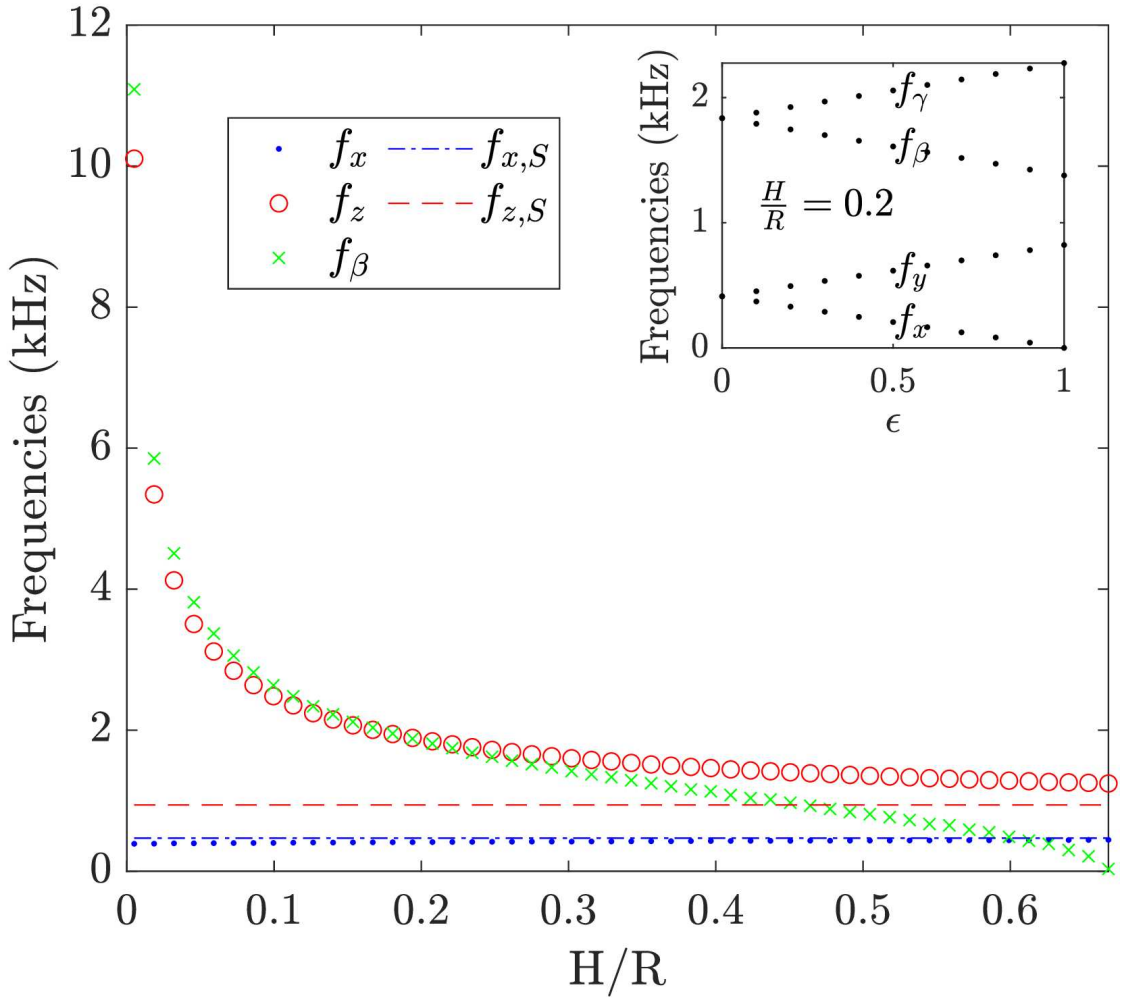


Figure 35: Frequencies for a superconducting niobium cylinder in a quadrupole field with $\epsilon = 0$ and $b_z = 500\,\mathrm{T/m}$, the dashed and dotted lines show the corresponding values for a superconducting sphere. The inset shows the dependence of the frequencies on ϵ, using $\frac{H}{R} = 0.2$.

z-mode is higher than the corresponding frequency for a sphere for all aspect ratios, and can be substantially higher for small aspect ratios. It appears that f_z could in principle be made arbitrarily high for small aspect ratios, so in practice the limit will likely be the rigidity of the material (or, alternatively, when H approaches the London penetration depth).

Note that the lateral frequency f_x decreases slowly with decreasing $\frac{H}{R}$. This was contrary to our initial expectations, as we assumed the behavior would be similar to a sphere - a linear dependence of the spring constant on H and thus f_x independent of the aspect ratio. We do not have an intuitive explanation for this result, but we double-checked that it is

not an artifact of the numerical approach (in particular we ascertained that the values of f_x converge with increasing mesh resolution and that the values are independent of the settings of the iterative solver).

Although we neglected rotations around the cylinder's symmetry axis for this analysis, in an actual experiment the cylinder would likely acquire some amount of angular momentum during lift-off. Presumably, such a rotation would couple the two librational modes and lead to precession around the symmetry axis, similar effects have been observed for optical levitation of aspherical particles [BSJ+20]. In addition, for a superconductor, a rotation around its axis corresponds to an additional magnetic moment (the London moment [BHS33, Lon61]). This effect is typically very small even for high rotation speeds [BHS33, Wan20] and, when it was initially theoretically derived, it was thought to be unmeasurable in experiments [BHS33]. Thus, for reasonable experimental parameters ($b_z \gtrapprox 1\,\mathrm{T/m}$), it should be negligible when evaluating the dynamics of the levitated cylinder.

6.5 Flux and coupling

Since the local magnetic field distribution depends on the position and orientation of the superconductor, changes in orientation and position of the levitated cylinder can be read-out by a measuring the change in magnetic flux ϕ through a suitable area ("pickup loop") close to the levitation point. For simplicity, we restrict ourselves to evaluating the flux through a planar circular pickup loop coaxial with the z-axis. The flux and coupling then depend on only two parameters, the radius of the pickup loop R_P and the height above the trap center Z_P (cf. Fig. 36a). For small oscillations around the equilibrium position and a suitable position of the pickup loop the flux depends linearly on the cylinder's position and can be characterized by a coupling strength $\eta_z = \partial_z \phi(\mathbf{x_0})$. For the numerical evaluation of the coupling we use a displacement of $2.5 \times 10^{-6}\,\mathrm{R}$, i.e.

$$\eta_z = \frac{\phi(z_0 = 2.5 \times 10^{-6}\,\mathrm{m}) - \phi(z_0 = -2.5 \times 10^{-6}\,\mathrm{m})}{5 \times 10^{-6}\,\mathrm{m}}.$$

Note that, for the same reasons discussed further above in the context of the maximum surface field, the coupling diverges when the pickup loop approaches the edges of the cylinder and becomes increasingly non-linear (cf. Fig. 36b). We have thus excluded a small area around $R_P = R, Z_P = \frac{1}{2}H$ from the evaluation, such that the minimal distance between the edge and the pickup loop is approximately $1 \times 10^{-3}\,\mathrm{R}$.

For each Z_P there is a unique pickup loop radius $R_{P,opt}(Z_P)$ that results in a maximum coupling strength $\eta_{opt}(Z_P)$, both of which are plotted in Fig. 37. Overall, as mentioned above, the coupling is highest when the pickup loop is close to the upper (or lower) edge of the cylinder. We can now compare η_{opt} for the cylindrical superconductor to the optimized coupling $\eta_{opt,S}$ for a spherical superconductor [HGH+23], where we choose the radius of the sphere such that it has the same volume as the cylinder (because the ratio $\frac{\eta_z^2}{m}$, where m is the mass of the levitated object, determines the thermal occupation of the z-mode under optimal feedback [HGH+23] and is thus a relevant quantity when comparing different geometries). We find that the optimal coupling is significantly higher for the cylindrical superconductor (cf. Fig. 37b) for all pickup loop positions. Experimentally the coupling strength can be further increased by using a multi-turn pickup loop and matching the inductance of the pickup loop to that of the sensor [HGH+23].

6.6 Maximum field

The maximum field on the surface of the cylinder is an important parameter to consider, as it has to stay below the (lower) critical field of the superconducting material - otherwise the

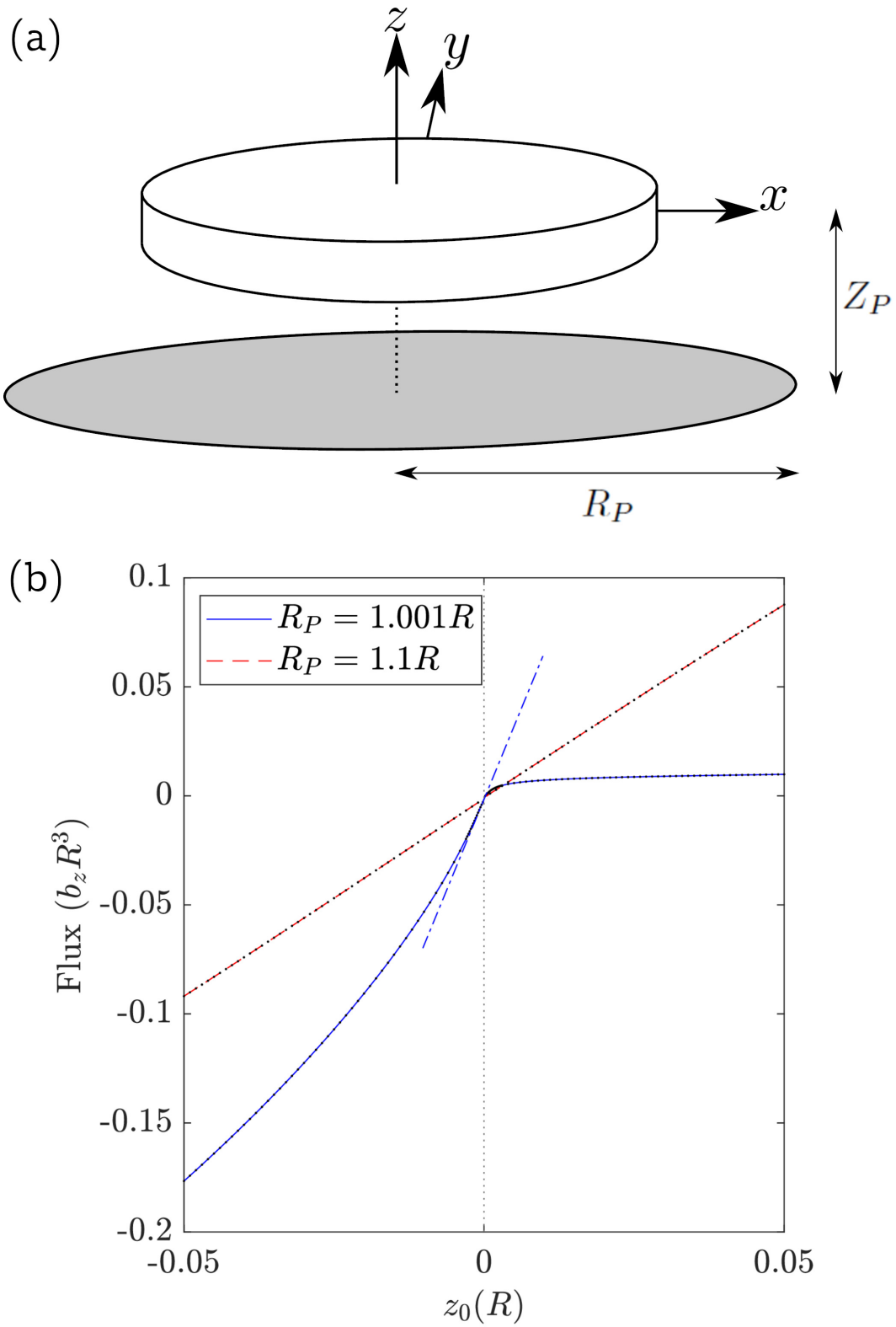


Figure 36: (a)Schematic of the trapped cylinder with a coaxial pickup loop. (b)Flux in a pickup loop with $Z_P = \frac{H}{2}$ as a function of particle displacement z_0. Both curves have been offset s.t. the flux for $z_0 = 0$ is zero. When the pickup loop is further away from the edge of the cylinder (dashed line), the dependence of the flux on the displacement is linear to a good approximation. When R_P is close to R the coupling (corresponding to the slope of the dash-dotted line) increases, but becomes increasingly non-linear.

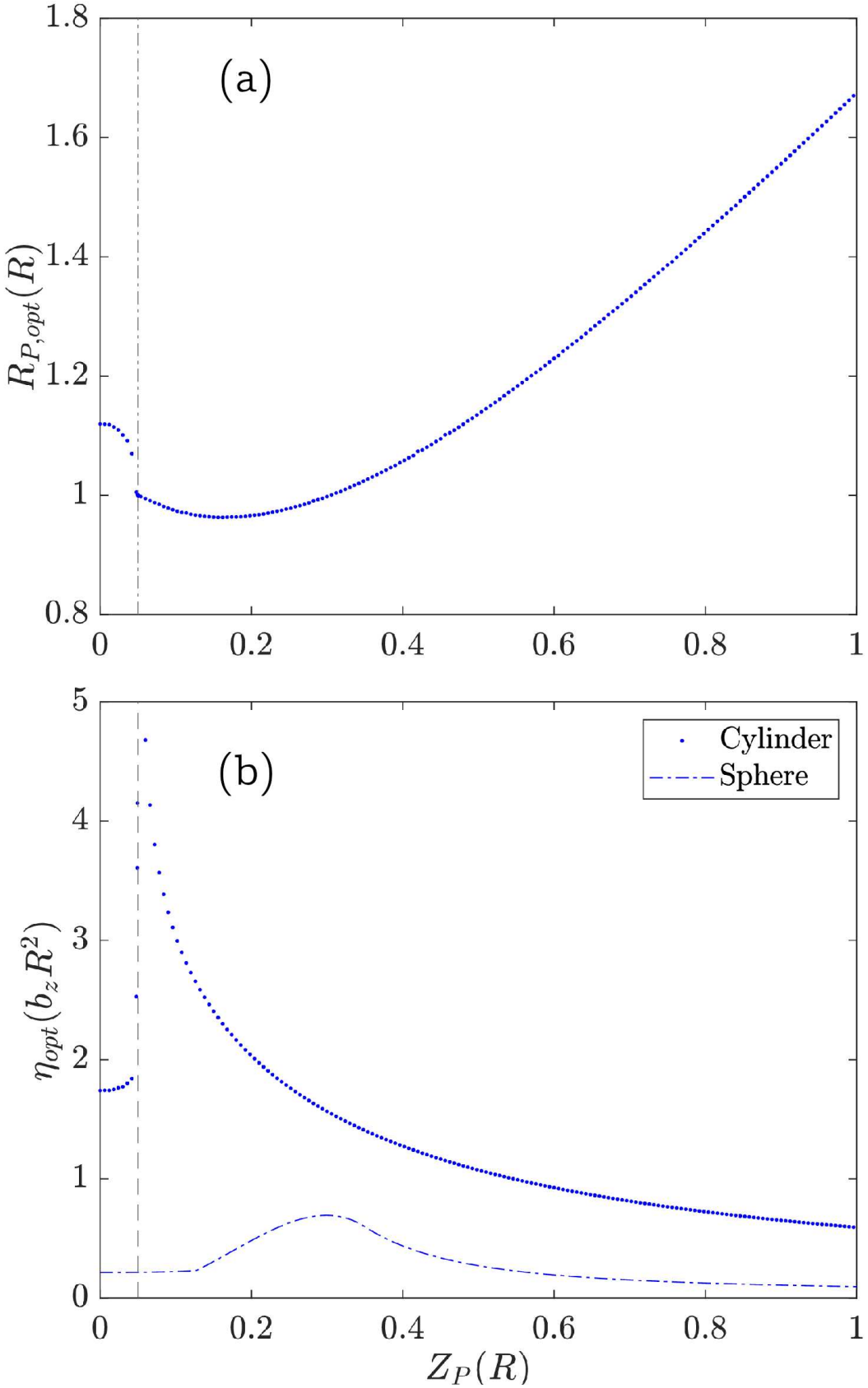


Figure 37: The optimal pickup loop radius (a) and the corresponding coupling (b) as a function of pickup loop position, for $\frac{H}{R} = 0.1$. The vertical dashed line denotes $Z_P = 0.05$, corresponding to the upper edge of the cylinder. The dash-dotted line in (b) shows the optimal coupling to a sphere of the same volume for comparison.

superconductor would enter either the intermediate state (for type-I superconductors) or the mixed state (for type-II superconductors), which can cause damping of the superconductor's motion due to induced eddy currents or hysteresis. We use the notation $B_{max} = max(|\mathbf{B}|)$, where the maximum is evaluated on the cylinder's surface when it sits at the trap center. As we've mentioned in the introduction, when the cylinder is modeled with sharp edges, B_{max} diverges (i.e. the numerically evaluated maximum surface field keeps increasing when the resolution of the mesh at the edge is increased). In order to determine B_{max} it is therefore necessary to introduce a rounded edge with a finite edge radius R_{edge} (cf. Fig. 38). In Fig. 39a we plot B_{max} as a function of R_{edge} for $\frac{H}{R} = 0.1$ and $\epsilon = 0$, whereas in Fig. 39b we show the dependence of B_{max} on the aspect ratio. For comparison we also performed a simulation of the full Maxwell-London equations, where the superconductor has a finite penetration depth λ, and find that the rounded edge approach overestimates the maximum surface field by a factor of approximately 1.6 when using $R_{edge} = \lambda$ (cf. Fig. 39), likely because the penetration depth does not correspond to a hard boundary and the field can penetrate deeper into the material. The maximum surface field is typically on the order of $b_z R$, so for superconductors on the micrometer scale it is well below typical critical fields (e.g. 80 mT for lead or 140 mT for the lower critical field of niobium) even for large gradients.

6.7 Summary and discussion

We have built a numerical model in COMSOL MULTIPHYSICS to calculate the magnetic field distribution around a superconductor inside a magnetic field. Due to choosing an approach based on the scalar potential (reducing the number of differential equations that need to be solved) the numerical model is not resource-intensive and can be solved on a typical personal computer. The trade-off is that it only applies to geometries large compared to the London penetration depth λ (typically on the order of tens of nanometers for type-I superconductors) and that it does not account for flux conservation if the superconductor contains any holes (e.g. in a ring). We note that there is no added difficulty in numerically solving the full Maxwell-London equations for the vector potential apart from being computationally expensive.

We then applied our model to the special case of a superconducting cylinder in a quadrupole field. The results show that, using a cylinder, it is possible to reach higher trap frequencies and coupling strengths compared to a sphere. Currently, thermal noise and vibrational noise at the trapping frequency are both major obstacles on the path towards ground state cooling a magnetically levitated micrometer-sized superconductor [HGH+23]. As vibrations decrease with increasing frequency and the thermal occupation of a feedback cooled harmonic oscillator is proportional to $\frac{m}{\eta^2}$ [HGH+23], using a cylindrical superconductor could significantly relax the requirements for ground state cooling. More generally, these results highlight the importance of the superconductor's geometry in determining the trap parameters and that non-trivial geometries should be investigated, even if an analytical solution is not available.

Going forward, we plan to introduce non-spherical superconductors in our experiments (cf. [HGH+23]) to take advantage of these findings. Also, having found that the shape of the superconductor plays a major role in determining the properties of the trap, we will study more complex geometries to identify the geometry that best suits our application.

The numerical model is available at the Zenodo repository [Hof24]. As it can be easily adapted to different superconducting geometries and trapping fields, we hope that it can serve as a useful tool for other researchers as well to find the optimal experimental arrangement for their purpose without having to rely exclusively on analytically solved models.

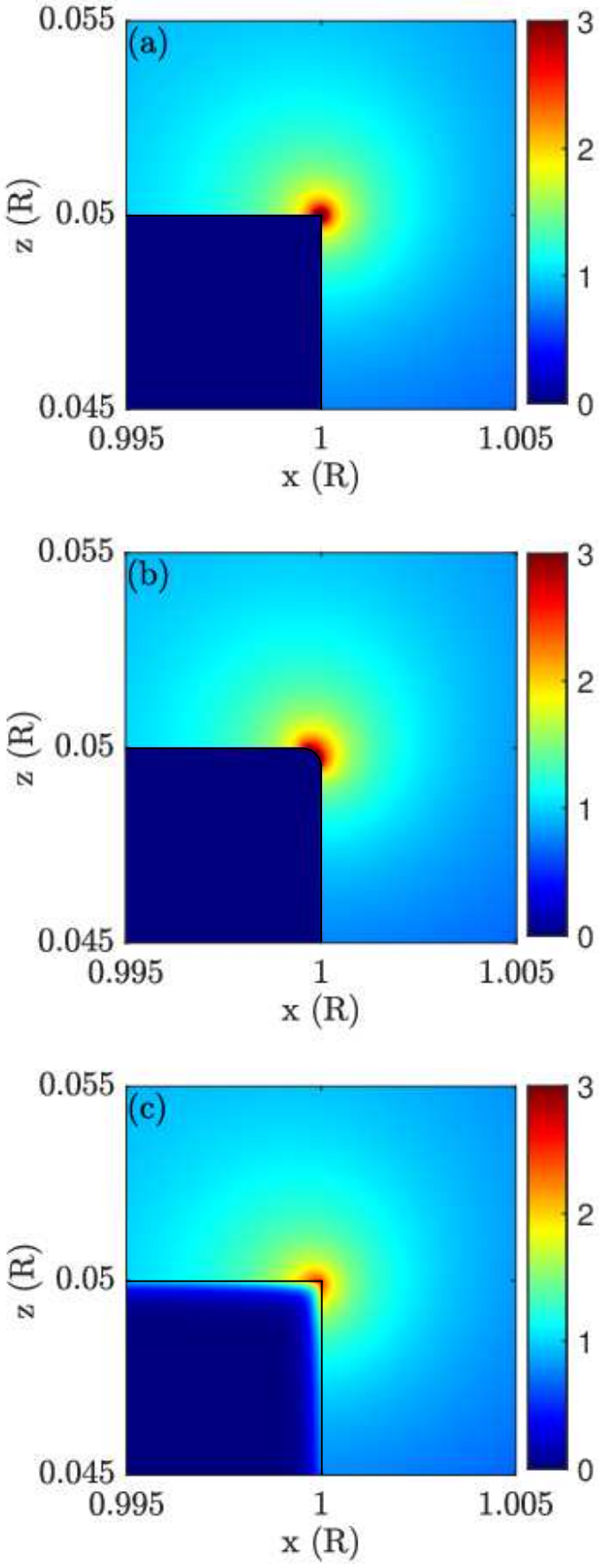


Figure 38: Field norm in the xz-plane around at the edge of a cylindrical superconductor with $\frac{H}{R} = 0.1$ in the $\beta = 0$ equilibrium position for a (a)sharp edge, (b)rounded edge and (c)sharp edge with finite penetration depth. The units on the colorbars are $b_z R$.

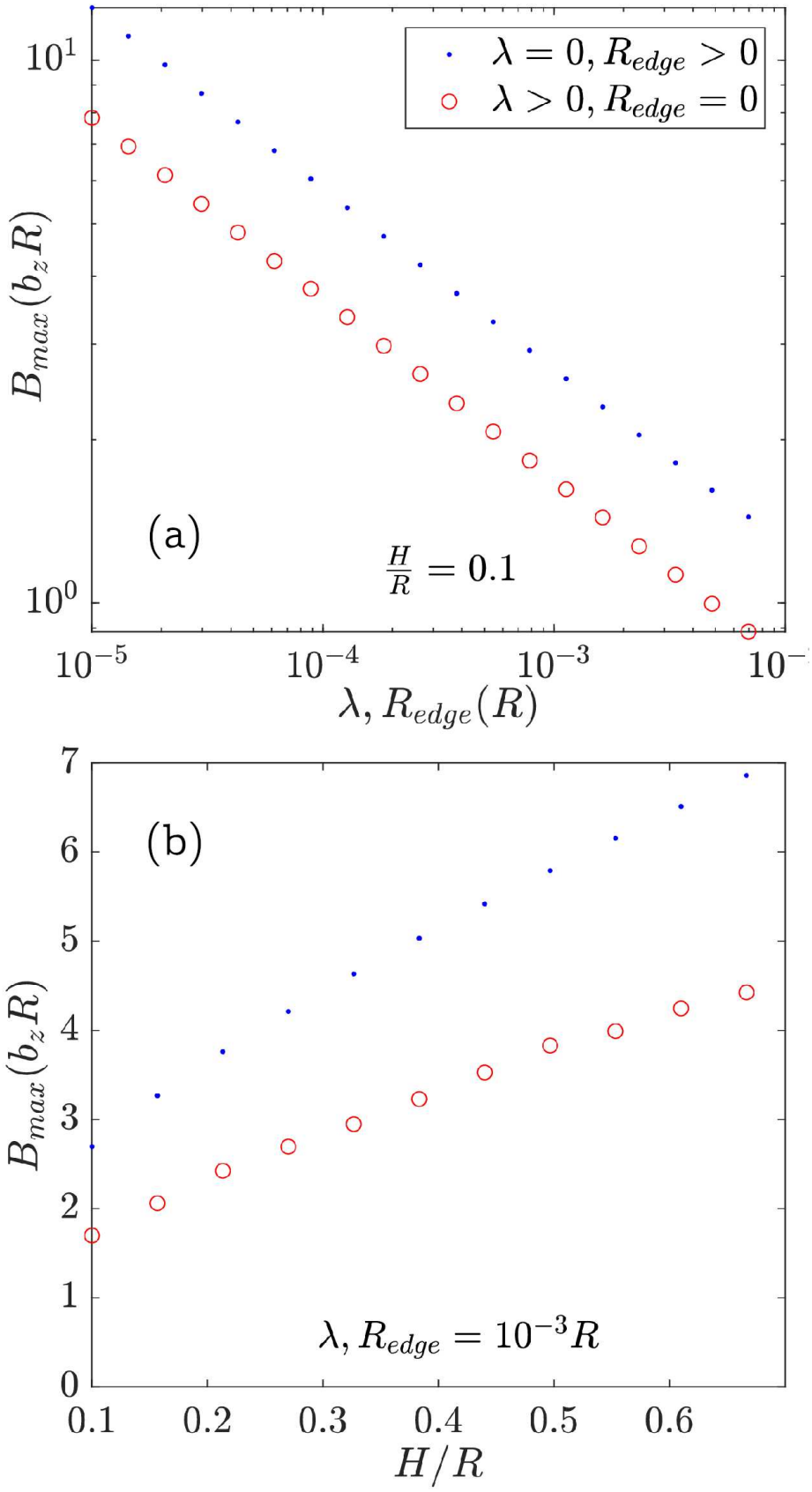


Figure 39: (a)The dependence of the maximum surface field on the edge radius resp. the penetration depth follows a power law with $B_{max} \propto R_{edge}^{-\frac{1}{3}}$ resp. $B_{max} \propto \lambda^{-\frac{1}{3}}$, where the proportionality coefficient is a function of $\frac{H}{R}$, as plotted in (b).

6.8 Acknowledgments

I am grateful for discussions with C. Navau Ros, J. Cunill Subiranas and N. J. Bort Soldevila, as well as discussions with P. Asenbaum, M. Aspelmeyer, R. Claessen, J. Hansen, G. Higgins, P. Schmidt and M. Trupke. This work was supported by the European Union's Horizon 2020 research and innovation programme under grant agreement No 863132 (iQLev), the European Union's Horizon Europe 2021-2027 Framework Programme under grant agreement No 101080143 (SuperMeQ), the European Research Council (ERC CoG QLev4G and ERC Synergy QXtreme), and the Austrian Science Fund (FWF) under project F40 (SFB FOQUS).

6.9 References

These are the references cited in the author's version of the manuscript.

[BHS33] R. Becker, G. Heller, and F. Sauter. Über die stromverteilung in einer supraleitenden kugel. *Zeitschrift für Physik*, 85(11):772–787, Nov 1933.

[BSCSDV+24] Natanael Bort-Soldevila, Jaume Cunill-Subiranas, Nuria Del-Valle, Witlef Wieczorek, Gerard Higgins, Michael Trupke, and Carles Navau. Modelling magnetically-levitated superconducting ellipsoids, cylinders and cuboids for quantum magnetomechanics. *Arxiv*, 2024.

[BSJ+20] Jaehoon Bang, T. Seberson, Peng Ju, Jonghoon Ahn, Zhujing Xu, Xingyu Gao, F. Robicheaux, and Tongcang Li. Five-dimensional cooling and nonlinear dynamics of an optically levitated nanodumbbell. *Phys. Rev. Res.*, 2:043054, Oct 2020.

[Goo99] John M. Goodkind. The superconducting gravimeter. *Review of Scientific Instruments*, 70(11):4131–4152, 1999.

[HA19] J Hofer and M Aspelmeyer. Analytic solutions to the maxwell–london equations and levitation force for a superconducting sphere in a quadrupole field. *Physica Scripta*, 94(12):125508, oct 2019.

[HGH+23] J. Hofer, R. Gross, G. Higgins, H. Huebl, O. F. Kieler, R. Kleiner, D. Koelle, P. Schmidt, J. A. Slater, M. Trupke, K. Uhl, T. Weimann, W. Wieczorek, and M. Aspelmeyer. High-q magnetic levitation and control of superconducting microspheres at millikelvin temperatures. *Phys. Rev. Lett.*, 131:043603, Jul 2023.

[Hof24] Joachim Hofer. Numerical model presented in the article "A numerical approach to levitated superconductors and its application to a superconducting cylinder in a quadrupole field". *Zenodo*, April 2024.

[Lon61] F. London. *Superfluids: Macroscopic theory of superconductivity.* Dover paperbound. Dover Publications, 1961.

[NMTS21] Carles Navau, Stefan Minniberger, Michael Trupke, and Alvaro Sanchez. Levitation of superconducting microrings for quantum magnetomechanics. *Phys. Rev. B*, 103:174436, May 2021.

[PPB21] T. W. Penny, Antonio Pontin, and Peter Barker. Performance and limits of feedback cooling methods for levitated oscillators: A direct comparison. *Physical Review A*, 2021.

[PPCS+18] H Pino, J Prat-Camps, K Sinha, B Prasanna Venkatesh, and O Romero-Isart. On-chip quantum interference of a superconducting microsphere. *Quantum Science and Technology*, 3(2):025001, jan 2018.

[RICN+12] O. Romero-Isart, L. Clemente, C. Navau, A. Sanchez, and J. I. Cirac. Quantum magnetomechanics with levitating superconducting microspheres. *Phys. Rev. Lett.*, 109:147205, 2012.

[SHK21] Benjamin A. Stickler, Klaus Hornberger, and M. S. Kim. Quantum rotations of nanoparticles. *Nature Reviews Physics*, 3(8):589–597, Aug 2021.

[VFG+20] A. Vinante, P. Falferi, G. Gasbarri, A. Setter, C. Timberlake, and H. Ulbricht. Ultralow mechanical damping with Meissner-levitated ferromagnetic microparticles. *Phys. Rev. Appl.*, 13(6), 2020.

[Wan20] Jun-Ping Wang. Altering magnetic response of superconductors by rotation. *Physics Letters A*, 384(36):126939, 2020.

Appendix

6.10 Convergence and comparison to the analytical solution

The accuracy of the numerical solution typically depends on various parameters, sources of errors include a geometrical error due to discretizing the geometry and an algebraic error depending on the termination criteria for the iterative solver. Ideally these errors can be made arbitrarily small by choosing a sufficiently well resolved mesh as well and a suitable termination criteria for the solver. Testing these errors is usually done by changing the parameters (such as mesh size and distribution, size of the simulation domain and relative size of the infinite element domain, solver tolerance and precision) and observing how the solution changes. If the numerical solution is already close to the actual solution, further refinements in these parameters should not result in large changes in the solution, i.e. the solution should converge to a fixed value w.r.t. these parameters.

In our case, we can additionally choose a geometry were the analytical solution is known (spherical superconductors), to verify that the numerical solution converges to the analytical solution for suitable mesh and solver settings. In Fig. 40 we show an example of a convergence plot w.r.t. $|F_x|$ (for a sphere radius $R_S = 1\,\mathrm{m}$, $b_z = 1\,\mathrm{T/m}$, $\epsilon = 0$ and $\mathbf{x_0} = (1, 0, 0)$) and the comparison to the analytical solution of $1.25 \times 10^6\,\mathrm{N}$ [HA19]. The numerical solution converges to the analytical solution with a relative error of less than $0.01\,\%$. The same behavior applies to all other evaluated quantities (force components and quantities derived thereof, field distribution, maximum surface field) and all show excellent agreement with the analytical values.

6.11 Dependence of the solutions on the edge radius or penetration depth

As mentioned in the main text, sharp edges on the cylinder lead to the divergence of the surface field at the edge (and, as a direct consequence, for the coupling strength to a pickup loop aligned with the edge). It is important to check that the results presented above, most of which are derived from the force and torque (and thus from surface integrals involving the magnetic field) are well-behaved. As described in the last section, we first check that the results for force and torque don't depend on the resolution of the mesh for a sufficiently fine resolution, i.e. that the numerical results converges with increasing mesh resolution.

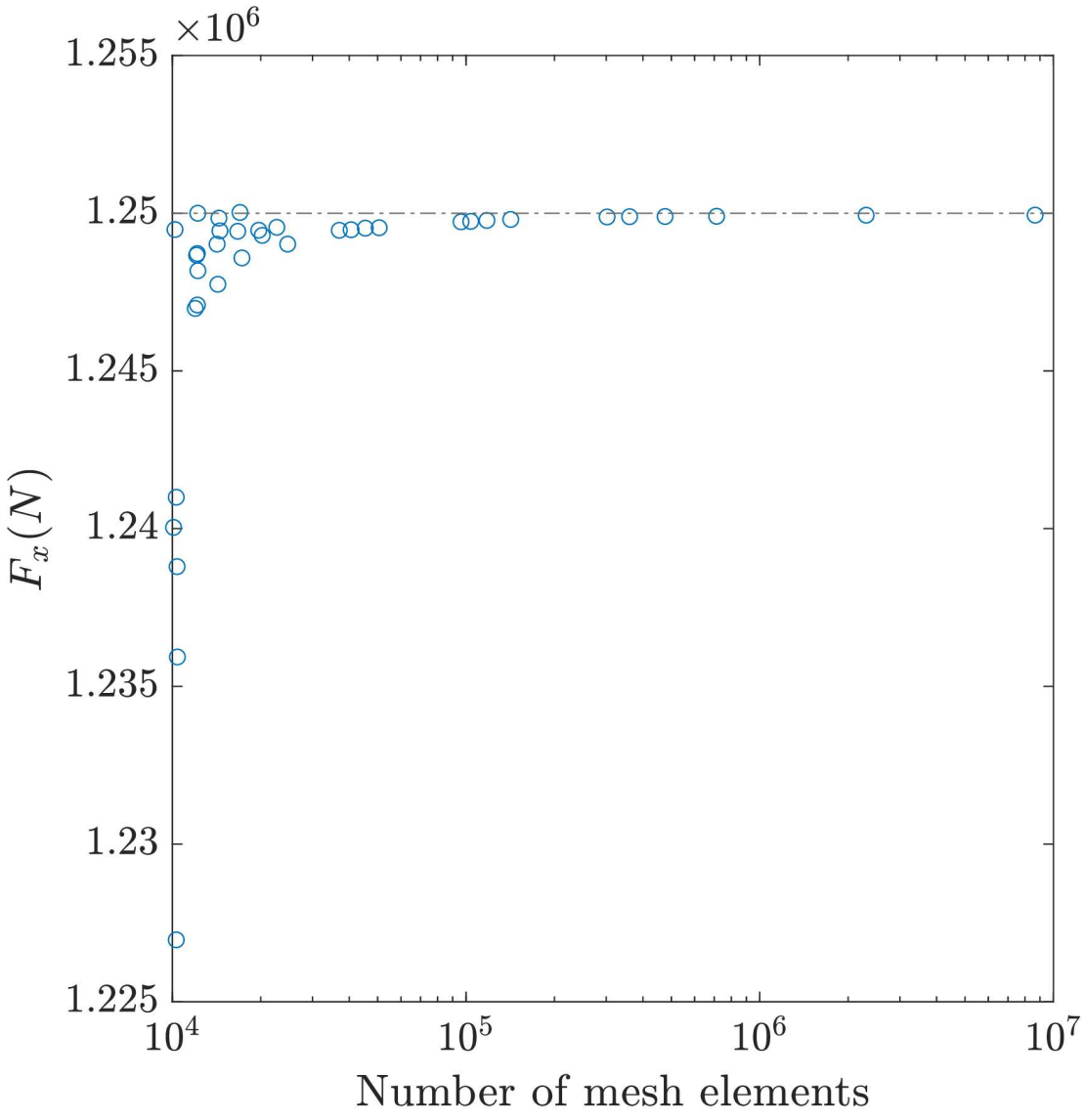


Figure 40: Convergence of $|F_x|$ for a spherical superconductor with increasing mesh resolution. The dash-dotted line corresponds to the analytical solution.

We then performed simulations with a finite edge radius R_{edge} and checked that the results converge for $R_{edge} \to 0$. Finally we did the same test using a model of the full Maxwell-London equations and a finite penetration depth λ. This test was only performed for some results, as solving this model on a personal computer with the required accuracy takes a long time. An example (F_z for $\frac{H}{R} = 0.1$ and $z_0 = R$) is shown in Fig. 41. For the maximum surface field we have already verified that it diverges for $R_{edge} \to 0$ and $\lambda \to 0$, this is described in the main text.

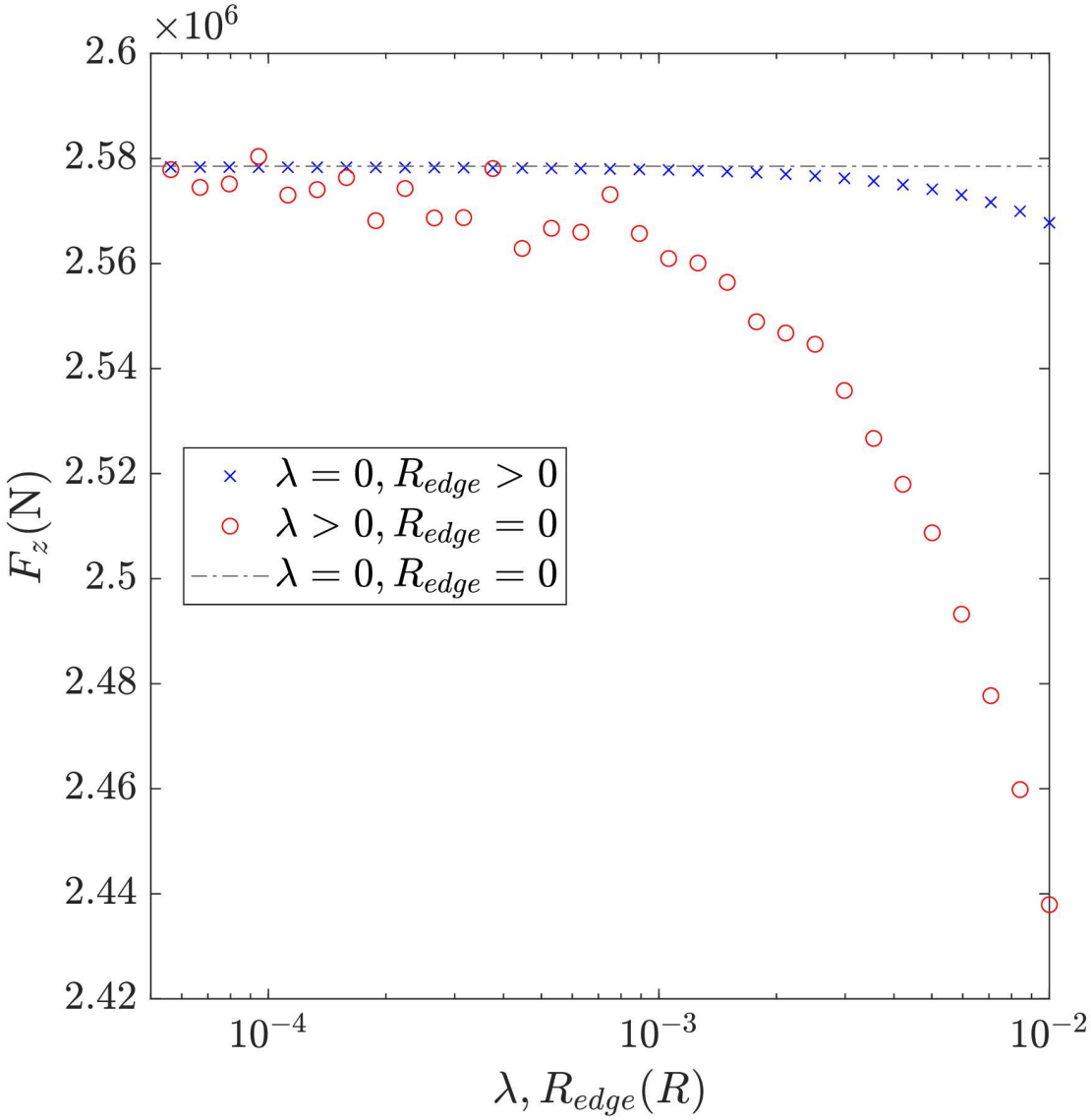


Figure 41: The results of simulations with rounded edges or finite penetration depths converge for $R_{edge} \to 0$ resp. $\lambda \to 0$. The dash-dotted line corresponds to the result obtained when using $R_{edge} = 0$ and $\lambda = 0$.

7 Measuring the gravitational field of small masses using levitated superconductors

In this section I introduce a planned experiment that uses a levitated superconductor as an acceleration sensor (test mass) to measure the gravitational field of another levitated superconductor (source mass). The idea is to levitate the two superconductors in close proximity (less than 1 mm apart), but in separate traps, and drive one of them at the resonance frequency of the other. The excellent force/acceleration sensing capabilities, introduced in the previous chapters, should enable us to measure the gravitational field of very small masses on the order of the Planck mass. The main difficulty one might expect of such a setup is the suppression of non-gravitational coupling mechanisms between the two levitated spheres. In order to achieve a suitable decoupling w.r.t. non-gravitational forces we plan to utilize a rigid superconducting sheet placed between the superconductors that prevents any direct electromagnetic coupling.

The structure of this chapter is as follows: After sharing my motivation for building this setup, I will introduce a magnetic trap that enables us to levitate a superconductor close to a superconducting surface. By mirroring this trap on both sides of a superconducting sheet we can then build a gravity measurement setup as outlined above. In the subsequent section I will calculate the gravitational coupling between the spheres, assuming that we can achieve at least the same parameters as in [HGH+23]. In the final section I will discuss one of the remaining experimental challenges for this type of measurement, namely direct vibrational coupling between the traps and how to prevent it.

7.1 Motivation

The motivation for this setup is to build a setup that brings quantum gravity experiments within reach. There is currently a strong disparity between the mass of objects whose gravitational field can be measured (approx. 100 mg [WHPA21]) and the mass of objects that can be prepared in a c.o.m. quantum state of motion (approx 3 fg, e.g. [MRB+21]). Most of the progress reported in this thesis has focused on increasing the mass of quantum systems by exploring the possibility of preparing a microgram mass (a 100 µm diameter tin-lead sphere) in a quantum state of motion. I will refer to this as the "bottom-up" approach. The setup I will introduce in this chapter, on the other hand, takes a "top-down" approach and aims to measure the gravitational field of much smaller masses than any previous experiment (by approx. five orders of magnitude). Because both the bottom-up and the top-down approach use the same experimental system (levitated microspheres), successful implementation of both would open up the path for the gravitational coupling of two quantum systems.

7.2 A new trap

The basic idea for the trap derives directly from the AHC setup introduced in Chapter 3. We can replace one of the coils by a superconducting sheet in the xy-plane, which will result in the quadrupole field of Eq. 14 in the lower (or upper, depending on which coil was replaced) half-space as depicted in Fig. 42. This result is directly obtained from the image method since $\mathbf{B_0}(\mathbf{x}, \mathbf{y}, 0)\,\mathbf{e_z} = 0$, which is also the boundary condition for the field on a superconducting sheet in the xy-plane. Note that the AHC trap and the coil-sheet (CS) trap are no longer identical in the half space when one considers the presence of a superconducting sphere. For the AHC the field distribution is set only by the boundary conditions on the surface on the sphere (and of course, the AHC current), while for the CS the boundary condition $\mathbf{B}(\mathbf{x}, \mathbf{y}, 0)\,\mathbf{e_z} = 0$ must hold. However, using numerical simulations to calculate the force

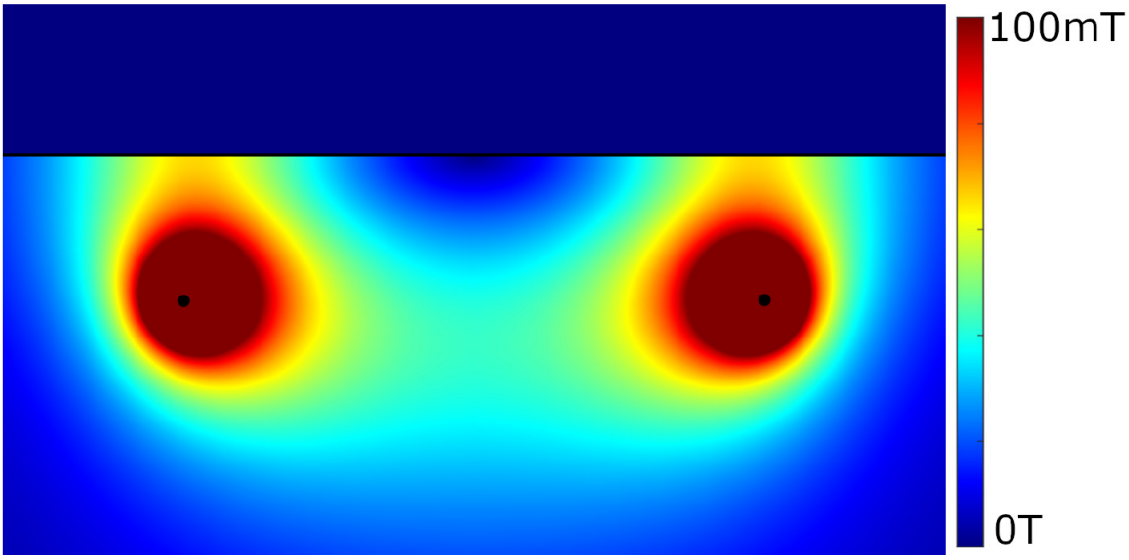


Figure 42: The field of a single coil (cross section, black circles) below a superconducting sheet (black line) is identical (neglecting the penetration depth of the superconductor) to the field of two coils in Anti-Helmholtz configuration (in the lower half-space). Shown is the field strength in the xz-plane.

on a superconducting sphere in the CS case we find that equation Eq. 12 for the force on a superconducting sphere in a quadrupole field is still an excellent approximation even if the sphere is close to the superconducting surface. Note that the force points towards the sheet for all sphere positions, so there is no stable levitation with just the magnetic force, as the sphere would end up pressed against the sheet. However, assuming that Earth's gravity is oriented along the negative z-axis, we see that we can create a magneto-gravitational trap. The total force along the z-axis is then given by

$$F_z \approx -\frac{3V}{2\mu_0} b_z^2 z_0 - mg,$$

with $g \approx 10\frac{m}{s^2}$, which results in a rest position at

$$z_0 = -\frac{2}{3}\mu_0 \rho g b_z^{-2} = -\frac{g}{\omega_0^2},$$

where $\rho = \frac{m}{V}$ is the density of the sphere. As long as $|z_0| > R$ (where R is again the sphere radius) levitation is possible. The maximum frequency (corresponding to $|z_0| = R$) that can be used with this setup is

$$f_z = \frac{1}{2\pi}\sqrt{\frac{g}{R}}.$$

For a 50 µm diameter lead-tin sphere this corresponds to approximately 70 Hz. However, such a magneto-gravitational trap is not sufficient for our purposes as we want to have a trapped particle on both sides of the superconducting sheet. To achieve this we can modify the CS trap by adding a second coil close to the surface of the superconducting sheet. This shifts the minimum from the surface of the field and results in the modified CS (MCS) distribution depicted in Fig. 43. We perform numerical simulations to evaluate the force on the sphere and find that this creates stable traps with both adjustable resonance frequency and adjustable sphere-sheet distance (this assumes that the currents through both coils can be adjusted independently). The limits for the frequency and distance depend on the

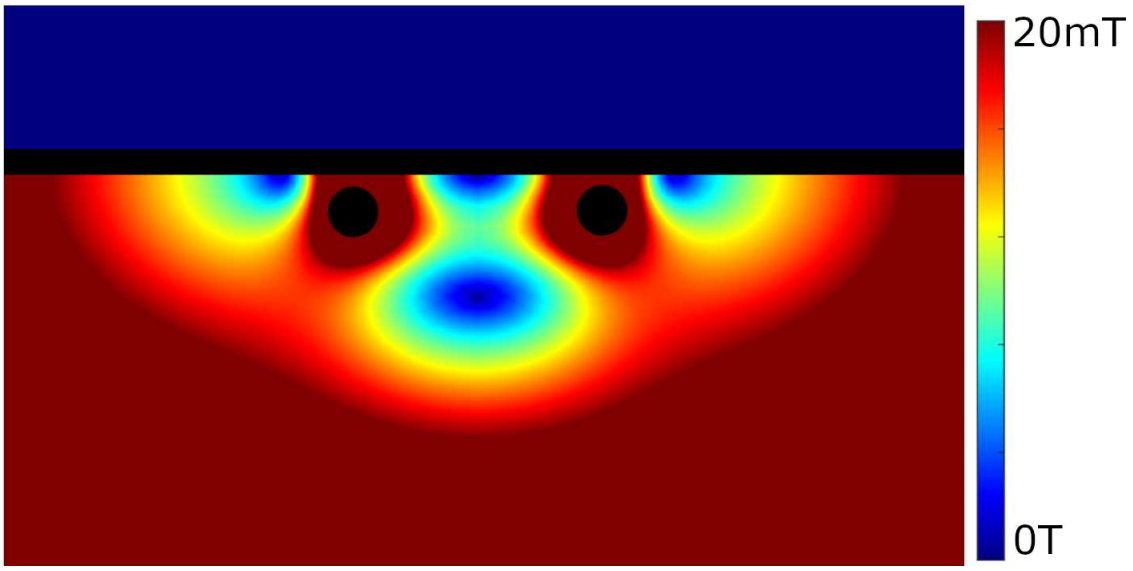


Figure 43: (a)Two coils enable us to create a field minimum separated from the surface and adjust the distance between the minimum and the field. Shown is the field strength close to the superconducting sheet in the xz-plane and the second coil (cross section, black circles), the larger coil is outside the picture.

geometry, the critical current of the coils and the critical field of the superconductors (both sphere and sheet). Using parameters we have already measured in the existing AHC setup and assuming a Niobium sheet with a conservative value of $B_{c1} = 140\,\mathrm{mT}$ for the lower critical field at millikelvin temperatures [FSS66], we should be able to reach sheet-sphere distances on the order of 100 µm, and frequencies of up to 500 Hz, which is enough to not be limited by vibrations and $1/f$-noise from the SQUID (cf. [HGH+23]). We can now assemble a setup for a gravity measurement as described in the introduction to this chapter, with both traps on opposite sides of the superconducting sheet. The upper trap is of the MCS configuration, while the lower trap can use either the CS or MCS configuration. However, we will show further below that it is advantageous to use a slightly different setup to prevent any direct vibrational coupling between the spheres.

7.3 Gravitational coupling

According to Newton's law the static gravitational force between two spheres of masses m_1 and m_2 separated by a c.o.m. distance d is

$$F_g = \frac{G m_1 m_2}{d^2},$$

where $G \approx 6.67 \times 10^{-11}\,\mathrm{Nm^2/kg^2}$ is called the gravitational constant. Allowing for small perturbations of d, s.t. $d \to d + x$ with $x \ll d$, the first order expansion term (i.e. the linear approximation) is given by

$$F_g = \frac{G m_1 m_2}{d^3} x.$$

If we now posit that both spheres are trapped in a harmonic potential as described in the last section, this introduces a gravitation coupling with a coupling strength

$$g_{grav} = G \frac{m_1 m_2}{d^3}.$$

For 100 µm lead-tin spheres separated by 0.5 mm this is approximately 2×10^{-17} N/m. If each oscillator has similar properties as the one described in [HGH+23], this coupling is too weak to detect any direct effect of this coupling on the dynamics of the oscillators such as resolving the normal modes or altered susceptibilities (cf. section 2.4). For all intended purposes the oscillators appear independent.

However, if we can drive one of the oscillators to large amplitudes and thus increase the force acting on the second oscillator, detecting this force would constitute a proof of the gravitational coupling. To see whether we can detect such a force we specifically consider the following scenario: One sphere will be used as a source mass and driven to large amplitudes (e.g. via a separate feedback coil as described in [HGH+23]). The other sphere will be used as a detector (test mass) and its position will be continuously measured. In this scenario the source mass drives the test mass gravitationally and the gravitational force spectral density acting on the test mass is

$$\sqrt{S_{FF,2}^{grav}} = \frac{Gm_1m_2}{d^3}\sqrt{S_{xx,1}}.$$

Since the power spectral density on resonance is $S_{xx,1}(\omega_{0,1}) \approx \frac{1}{b}\langle x_1^2\rangle$, where b denotes the bandwidth of the driven oscillations in Hertz, we can express this as

$$\sqrt{S_{FF,2}^{grav}(\omega_{0,1})} \approx \frac{Gm_1m_2}{d^3}\sqrt{\frac{1}{b}\langle x_1^2\rangle}.$$

Note that the bandwidth b could be set by either by the natural linewidth of the source mass ($b \approx \gamma_1$) or by the drive signal (if the drive bandwidth is narrower than γ_1). We will assume the former from now on, as it is difficult to find function generators with a bandwidth on the order of 1 µHz. The gravitational force PSD due to the oscillations of the source mass needs to be compared to the force sensitivity of the test mass, which in the thermal noise limit is given by

$$\sqrt{S_{FF,2}^{th}} = \sqrt{4k_BTm_2\gamma_2}.$$

The resulting signal to noise ratio (SNR) is thus

$$SNR = \frac{Gm_1}{d^3}\sqrt{\frac{m_2\langle x_1^2\rangle}{4k_BT\gamma_1\gamma_2}}.$$

We plot the signal to noise ratio as a function of the source mass in Fig. 44, assuming a separation $d = 500$ µm, a source mass amplitude $\sqrt{\langle x_1^2\rangle} = 30$ µm and otherwise the same parameters as those of the system characterized in [HGH+23] (see the caption of Fig. 44 for details). Even without further improvements we should be able to measure the gravitational field of a 5 µg source mass with $SNR > 1$, which would improve the current state-of-the-art [WHPA21] by almost 5 orders of magnitude. In [HGH+23] the force sensitivity obtained for a single sphere was around $65 \times 10^{-19}\,\mathrm{N}/\sqrt{\mathrm{Hz}}$, around one order of magnitude above the thermal noise limit, due to fluctuations of the trap current (and thus the trap frequency). This can be mitigated by either increasing the coupling of the levitated particle to the SQUID or stabilizing the trap current (or a combination of both). We have since successfully tested a persistent current switch to stabilize the trap current. In addition, improving the coupling is straightforward and will also be implemented in the planned setup, such that the force sensitivity will be limited by thermal fluctuations. This will enable a measurement of the gravitational field of a 0.2 µg mass (cf. Fig. 44).

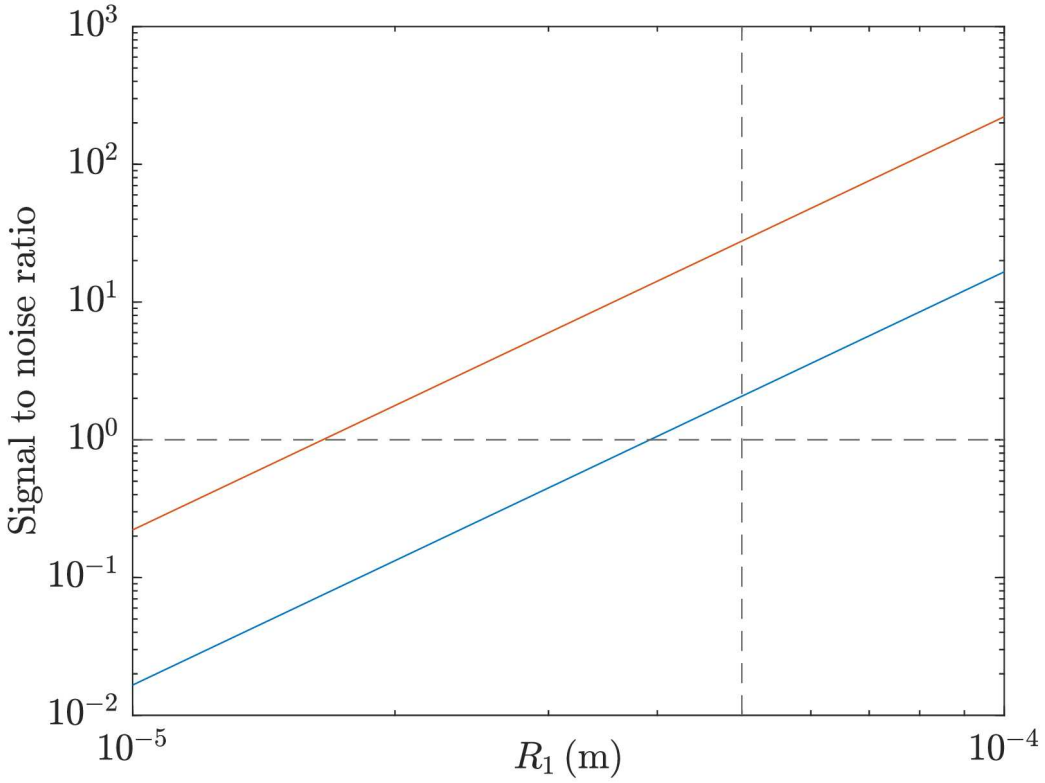


Figure 44: Signal to noise ratio as a function of the source mass radius. With current experimental sensitivities (blue line), the gravitational field of a sphere with a 50 µm radius (corresponding to a mass of approximately 5 µg) could be detected with a SNR above one. With a thermally limited system (orange line), the corresponding SNR is approximately 30. Alternatively, a thermally limited system could detect a 17 µm (0.2 µg) particle with a SNR of one. The dashed lines, corresponding to $SNR = 1$ and $R_1 = 50\,\mu\text{m}$ are guides to the eye. The parameters assumed in these plot are: $d = 500\,\mu\text{m}$, $\sqrt{\langle x_1^2 \rangle} = 30\,\mu\text{m}$, $R_2 = 50\,\mu\text{m}$, $\gamma_1 = \gamma_2 = 50\,\text{s}^{-1}$, $T = 15\,\text{mK}$, $\rho = 10\,900\,\text{kg/m}^3$.

7.4 Vibrational coupling

In order to show gravitational coupling one needs to rule out other coupling mechanism and. In my opinion, the main benefit of this proposed setup is not the great force/acceleration sensitivity of the levitated particles, but the excellent isolation of non-gravitational coupling mechanisms (in particular electromagnetic ones) even at small particle-to-particle distances due to the superconducting shielding. However, one remaining coupling mechanism we need to consider is vibrational coupling.

When we introduced passive vibration isolation in chapter 2, we have made the assumption that the levitated particle is decoupled from the stages of the vibration isolation, i.e. we have treated the vibration isolation and the trapped particle as separate systems. This is a good assumption due to the large disparities in mass, frequency and the small dissipation of the levitated system. However, if two magnetic traps are connected to the same vibration isolation stage, the coupling mediated by the vibration isolation stage is (for realistic parameters) orders of magnitude stronger than the gravitational coupling.

Consider the system shown in Fig. 45: Two harmonic oscillators (indices 1,2) are connected to a single-stage vibration isolation system (3). This system is described by the

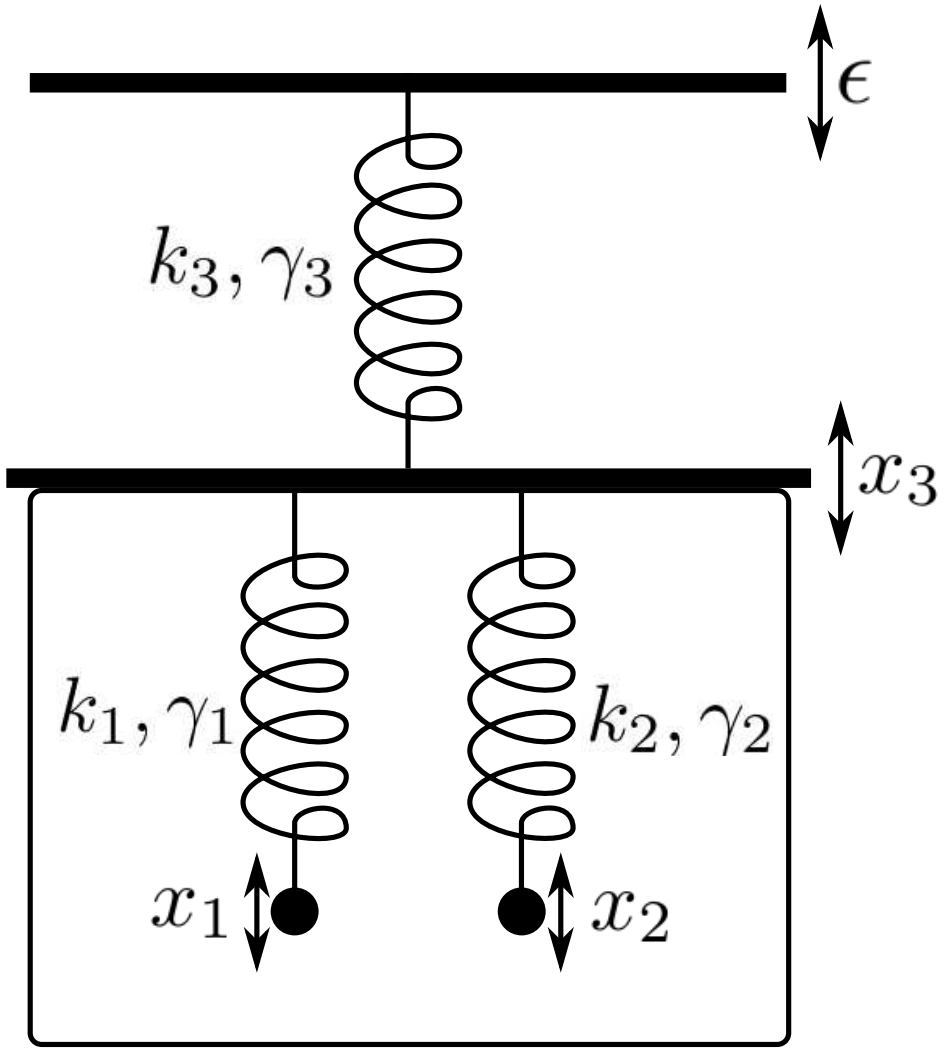


Figure 45: Two harmonic oscillators (1,2) are connected to a vibration isolation stage (3) via their springs. The vibration isolation introduces an effective frequency-dependent coupling between the two oscillators which is proportional to its response function $\chi_3(\omega)$.

equations

$$
\begin{aligned}
m_1\ddot{x}_1 &= -k_1\delta_1 - m_1\gamma_1\dot{\delta}_1 \\
m_2\ddot{x}_2 &= -k_2\delta_2 - m_2\gamma_2\dot{\delta}_2 \\
m_3\ddot{x}_3 &= -k_3\delta_3 - m_3\gamma_3\dot{\delta}_3 + k_1\delta_1 + m_1\gamma_1\dot{\delta}_1 + k_2\delta_2 + m_2\gamma_2\dot{\delta}_2,
\end{aligned}
$$

where x_i denotes the displacement of each oscillator w.r.t. a common inertial reference frame and $\delta_1 = x_1 - x_3$, $\delta_2 = x_2 - x_3$, $\delta_3 = x_3 - \epsilon$, cf. Chapter 2) denotes the displacement of each oscillator from its rest position. Assuming small damping, the main effect of the vibration isolation (apart from reducing vibrations, of course) is to introduce an effective coupling with a coupling strength

$$g_{vib} \approx \chi_3(\omega) k_1 k_2$$

between the two levitated particles. If we drive the source mass (1) at the resonance frequency of the test mass (2), and if ω_1, $\omega_2 \gg \omega_3$, the ratio of the induced coupling to the gravitational coupling becomes approximately

$$\frac{g_{vib}}{g_{grav}} \approx \frac{d^3\,\omega_1^2}{G\,m_3}.$$

For values corresponding to the existing setup ($m_3 \approx 0.3\,\mathrm{kg}$, $\omega_1 \approx 2\pi \cdot 200\,\mathrm{Hz}$) and assuming $d = 0.5\,\mathrm{mm}$, the induced vibrational coupling is higher than the gravitational coupling by a factor of 1×10^7.

In addition, the motion of the particle could also excite vibrational modes of the superconducting sheet (in particular the breathing mode would lead to a direct coupling between the spheres), and simulations show that this could lead to a coupling of similar strength - the coupling strength here is strongly dependent on the dimensions of the sheet (i.e. the effective mass and resonance frequency of the modes), but it would be hard to reduce it to levels below the gravitational coupling strength.

The obvious solution is to not connect the magnetic traps to the same vibration isolation system, but rather to use two separate vibration isolation systems (cf. Fig. 46). Even if the internal modes of the top plate (to which both vibration isolation systems are connected) are taken into account, this reduces the vibrational coupling to levels far below the gravitational coupling. However, one still needs to be careful to avoid any non-mechanical coupling between the vibration isolation stages (e.g. due to charges, or induced magnetic moments, ...). This will likely be the main experimental challenge when building this experiment.

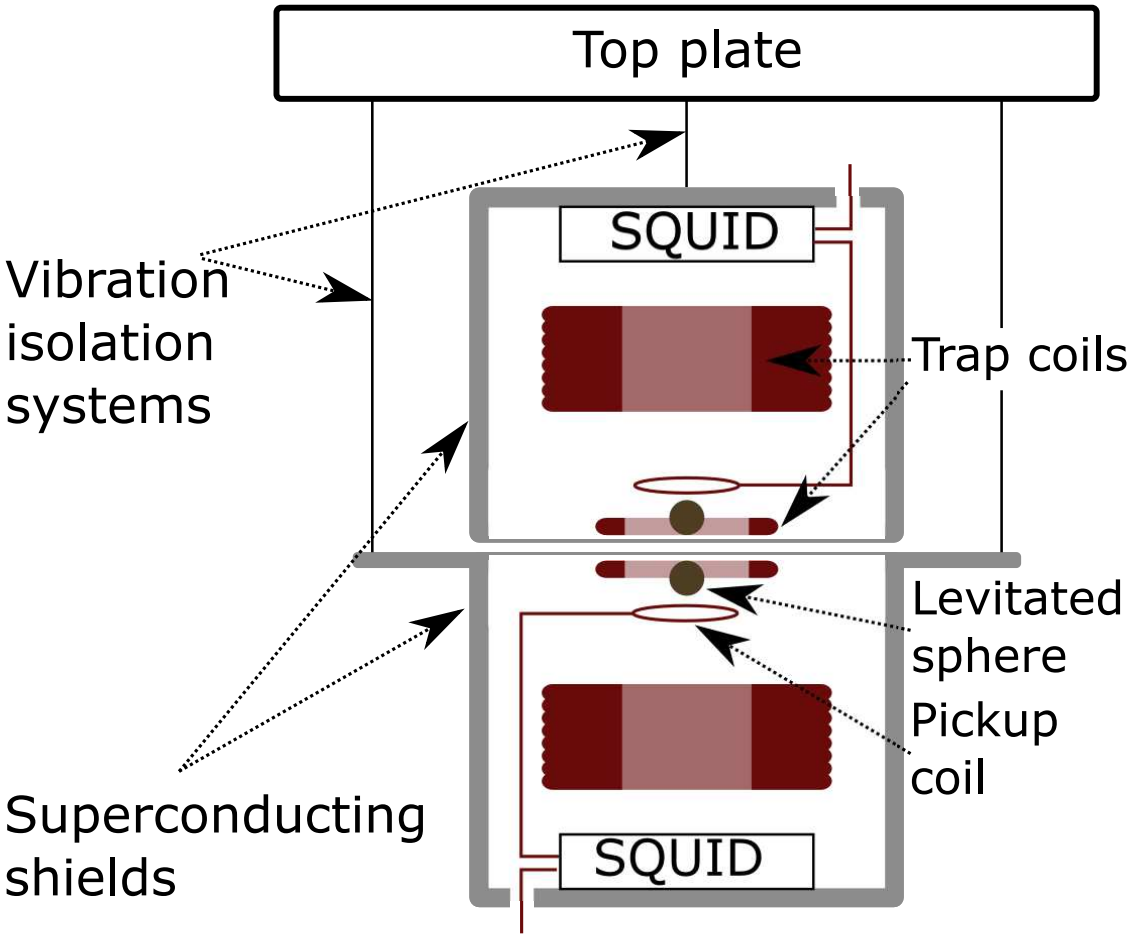


Figure 46: Both traps are housed in separate superconducting shields and connected to separate vibration isolation systems. Since the top plate is typically a massive copper plate, its internal resonances are very high and it appears rigid at the frequencies of the levitated oscillators, leading to an effective mechanical decoupling of the two systems. While the schematic shows only one vibration isolation stage, in the planned setup both traps will be connected to mult-stage vibration isolation systems, each one similar to the one presented in [HGH+23].

8 Conclusion and Outlook

Over the timeframe of this thesis I built a proof-of-concept platform for high-Q-levitation of superconducting particles. I established both an analytical as well as an numerical framework to quantitatively predict and evaluate the behavior of the levitated particles. The results were summarized in three publications [HA19, HGH+23, Hof24], each dealing with one of these aspects.

In [HA19] I found an analytical solution for the field distribution around a superconducting sphere in a magnetic quadrupole field. This field is generated by many common trap configurations such as Anti-Helmholtz traps or a chip-based "double-loop" traps [LHRW20]. From the field distribution one can calculate the trap parameters (frequency, coupling, ...). The same method can be used to calculate the field distribution for different trapping fields as well and can even be generalized to some non-spherical superconductors such as dumbbells.

In [HGH+23] we present a proof-of-concept experiment for the magnetic levitation of superconductors. In this experiment we show a magnetically levitated sphere with low dissipation, magnetomechanical readout of the sphere's position with a SQUID, 3D-feedback control of the c.o.m. position of the sphere as well as a large decoupling from the environment due to a novel cryogenic vibration isolation and careful electrical engineering. We perform a thorough analysis of the results and show that, by improving several aspects of the setup, ground state cooling of the c.o.m. motion of the levitated particle is possible. We show a clear path how each of the necessary improvements can be implemented. The experiment also sets several milestones for magnetic levitation setups in general (i.e. not just limited to the levitation of superconductors), such as (at the current date and to the best of my knowledge) the highest mechanical quality factor, the highest magnetomechanical coupling strength and the lowest steady-state temperature of the particle motion (corresponding to the high degree of decoupling from the environment).

Finally, in [Hof24] I adapt the methods from [HA19] to build a numerical framework for obtaining the field distribution around arbitrarily shaped superconductors in arbitrary trapping fields (while the analytical solution from [HA19] can be generalized to some non-spherical geometries of the superconductor, this is not possible for all geometries). I apply the numerical framework to the specific case of a superconducting cylinder and show that the cylindrical geometry can lead to higher trapping frequencies as well as higher coupling strengths when compered to the spherical case, which in turn reduces the demands for ground state cooling.

In addition to the publications presented here, the methods established therein have been adapted and used for the levitation of a superconductor with a chip-based magnetic trap [LPH+22, GLHP+23] as well as the readout of a magnetically levitated superconductor by coupling it to a microwave cavity [SCH+24]. Several other experiments that rely on the methods developed in this thesis are in preparation, such as using a levitated superconductor as a dark matter detector [HKL24].

In the introductory Chapters 2 and 3 of this thesis I aimed to introduce the relevant theory in such a way that anyone with a physics background can understand the content of the publications without having to consult further material. I also briefly covered some topics that were not presented in the publications.

In Chapter 7 I present a new experiment that I am currently building, which aims to use one levitated superconductors to measure the gravitational field of another. This experiment is designed for the measurement of the gravitational field of a mass on the order of the Planck scale, several orders of magnitude below the current state-of-the art [WHPA21].

Further, magnetic traps for superconductors are very versatile and I think that this thesis, where I have for the most part focused on a single trap architecture, only scratched

the surface of what is possible with quasi-static magnetic traps. For example, I showed briefly (Chapter 3) how a trap with multiple, spatially separated harmonic potentials can be constructed, and how it is possible to switch between different potential types (single harmonic, multi-well, quartic, repulsive). This enables, once such a system approaches the quantum realm, the implementation of experiments with non-harmonic potentials to create spatially separated quantum states on a fast timescale [NCRI+24, RLRCC+24].

Another example is the levitation of multiple levitators within a single trap. I numerically investigated the levitation of two spheres in a quadrupole trap and found that they should experience an effective attraction and behave like a dumbbell. I have later conducted experiments that confirmed this picture (cf. Fig. 47). However, contrary to my expectations, three spheres do not experience an attraction, but form a stable configuration with each sphere levitating at distinct points (imagine a triangle with the spheres at the tips, cf. Fig. 47). While we did not investigate further, the collective modes of such a many-body system (of

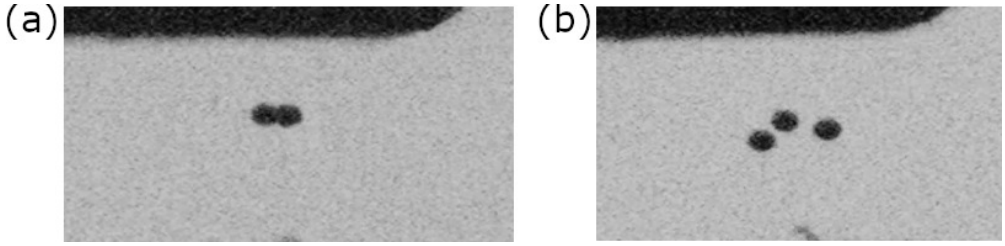


Figure 47: Pictures of multiple levitated superconducting spheres in the magnetic field generated by AHC coils. (a)Two levitated spheres experience an attraction and behave like a rigid dumbbell. (b)Three spheres seem to repulse each other and form a stable triangular configuration around the symmetry axis of the AHC coils.

three or more levitators) might have interesting properties. As a trivial example, some of the modes could be insensitive to common vibrational noise and allow easier preparation of a quantum state or be of use as a differential force sensor.

When I started this thesis, even though magnetic levitation had been very successfully implemented for gravimeters [Goo99], it was still unclear whether it could be used for systems with low dissipation and relatively high frequencies, and whether environmental noise at these frequencies could be suppressed in a cryogenic environment to make the system useful. I believe that this thesis and the corresponding publications answered these questions in the affirmative and resulted in a convincing proof-of-concept of the potential of magnetic levitation of a superconductor.

For sensing, this system shows force (acceleration) sensitivities that are otherwise only reached with much smaller (larger) masses. As briefly mentioned above, magnetically levitated superconductors have now been proposed as a new generation of dark matter sensors [HKL24]. By choosing a suitable trap architecture and levitator, one can be sensitive to different proposed forms of dark matter over a frequency range from millihertz to several hundreds of hertz.

As a final remark, I am happy that different types of magnetic levitation are now being used by many research groups and that new results are published more and more frequently. I hope that the results presented here might convince others to join in as well.

Bibliography

[Ark47] V Arkadiev. A floating magnet. *Nature*, 160(4062):330–330, September 1947.

[AS64] Milton Abramowitz and Irene A. Stegun. *Handbook of Mathematical Functions with Formulas, Graphs, and Mathematical Tables*. Dover, 1964.

[BG97] Michael V. Berry and A. K. Geim. Of flying frogs and levitrons. *Eur. J. Phys.*, 18:307–313, 1997.

[BKT92] Vladimir B. Braginsky, Farid Ya Khalili, and Kip S. Thorne. *Quantum Measurement*. Cambridge University Press, 1992.

[Bra88] Ernst Helmut Brandt. Friction in levitated superconductors. *Applied Physics Letters*, 53:1554–1556, 1988.

[BSCSDV+24] Natanael Bort-Soldevila, Jaume Cunill-Subiranas, Nuria Del-Valle, Witlef Wieczorek, Gerard Higgins, Michael Trupke, and Carles Navau. Modelling magnetically-levitated superconducting ellipsoids, cylinders and cuboids for quantum magnetomechanics. *Arxiv*, 2024.

[Cav82] Carlton M. Caves. Quantum limits on noise in linear amplifiers. *Phys. Rev. D*, 26:1817–1839, Oct 1982.

[CCW70] A.F. Clark, G.E. Childs, and G.H. Wallace. Electrical resistivity of some engineering alloys at low temperatures. *Cryogenics*, 10(4):295–305, 1970.

[CDG+10] A. A. Clerk, M. H. Devoret, S. M. Girvin, Florian Marquardt, and R. J. Schoelkopf. Introduction to quantum noise, measurement, and amplification. *Rev. Mod. Phys.*, 82:1155–1208, Apr 2010.

[CK04] Robin Cantor and Dieter Koelle. *Practical DC SQUIDS: Configuration and Performance*, chapter 5, pages 171–217. John Wiley and Sons, Ltd, 2004.

[CM87] Carlton M. Caves and G. J. Milburn. Quantum-mechanical model for continuous position measurements. *Phys. Rev. A*, 36:5543–5555, Dec 1987.

[Con19] Gerard P. Conangla. Sensing with the harmonic oscillator, 2019.

[CST19] Daniel Carney, Philip C E Stamp, and Jacob M Taylor. Tabletop experiments for quantum gravity: a user's manual. *Classical and Quantum Gravity*, 36(3):034001, Jan 2019.

[DRSPR17] Jordi Díaz, Mario Ruiz, Pilar S. Sánchez-Pastor, and Paula Romero. Urban seismology: on the origin of earth vibrations within a city. *Scientific Reports*, 7(1):15296, Nov 2017.

[Eva17] J. B. Evans. Environmental noise and ground vibration control for precision calibration laboratory. In *24th International Congress on Sound and Vibration*, London, Jul 2017.

[FSS66] D. K. Finnemore, T. F. Stromberg, and C. A. Swenson. Superconducting properties of high-purity niobium. *Phys. Rev.*, 149:231–243, Sep 1966.

[FZ07] József Fortágh and Claus Zimmermann. Magnetic microtraps for ultracold atoms. *Rev. Mod. Phys.*, 79:235–289, Feb 2007.

[GLHP+23] Martí Gutierrez Latorre, Gerard Higgins, Achintya Paradkar, Thilo Bauch, and Witlef Wieczorek. Superconducting microsphere magnetically levitated in an anharmonic potential with integrated magnetic readout. *Phys. Rev. Appl.*, 19:054047, May 2023.

[Goo99] John M. Goodkind. The superconducting gravimeter. *Review of Scientific Instruments*, 70(11):4131–4152, 1999.

[HA19] J Hofer and M Aspelmeyer. Analytic solutions to the Maxwell–London equations and levitation force for a superconducting sphere in a quadrupole field. *Physica Scripta*, 94(12):125508, Oct 2019.

[Hei27] W. Heisenberg. Über den anschaulichen inhalt der quantentheoretischen kinematik und mechanik. *Zeitschrift für Physik*, 43(3):172–198, Mar 1927.

[HGH+23] J. Hofer, R. Gross, G. Higgins, H. Huebl, O. F. Kieler, R. Kleiner, D. Koelle, P. Schmidt, J. A. Slater, M. Trupke, K. Uhl, T. Weimann, W. Wieczorek, and M. Aspelmeyer. High-q magnetic levitation and control of superconducting microspheres at millikelvin temperatures. *Phys. Rev. Lett.*, 131:043603, Jul 2023.

[HKL24] Gerard Higgins, Saarik Kalia, and Zhen Liu. Maglev for dark matter: Dark-photon and axion dark matter sensing with levitated superconductors. *Phys. Rev. D*, 109:055024, Mar 2024.

[Hof24] J Hofer. A numerical approach to levitated superconductors and its application to a superconducting cylinder in a quadrupole field. *Physica Scripta*, 99(9):095526, Aug 2024.

[HVT+17] David Hempston, Jamie Vovrosh, Marko Toroš, George Winstone, Muddassar Rashid, and Hendrik Ulbricht. Force sensing with an optically levitated charged nanoparticle. *Applied Physics Letters*, 111(13):133111, 2017.

[Jac99] John David Jackson. *Classical electrodynamics*. Wiley, 3rd ed. edition, 1999.

[Jef05] Alan Jeffrey. *Complex Analysis and Applications*. Chapman and Hall, New York, 2 edition, 2005.

[LHRW20] Martí Gutierrez Latorre, Joachim Hofer, Matthias Rudolph, and Witlef Wieczorek. Chip-based superconducting traps for levitation of micrometer-sized particles in the Meissner state. *Superconductor Science and Technology*, 33(10):105002, aug 2020.

[LPH+22] Martí Gutierrez Latorre, Achintya Paradkar, David Hambraeus, Gerard Higgins, and Witlef Wieczorek. A chip-based superconducting magnetic trap for levitating superconducting microparticles. *IEEE Transactions on Applied Superconductivity*, 32(4):1–5, 2022.

[MDB+23] M. Mohr, Y. Dong, G. P. Bracker, R. W. Hyers, D. M. Matson, R. Zboray, R. Frison, A. Dommann, A. Neels, X. Xiao, J. Brillo, R. Busch, R. Novakovic, P. Srirangam, and H.-J. Fecht. Electromagnetic levitation containerless processing of metallic materials in microgravity: thermophysical properties. *npj Microgravity*, 9(1):34, May 2023.

[MGFM17] Fernando Monteiro, Sumita Ghosh, Adam Getzels Fine, and David C. Moore. Optical levitation of 10-ng spheres with nano-g acceleration sensitivity. *Phys. Rev. A*, 96:063841, Dec 2017.

[MRB+21] Lorenzo Magrini, Philipp Rosenzweig, Constanze Bach, Andreas Deutschmann-Olek, Sebastian G Hofer, Sungkun Hong, Nikolai Kiesel, Andreas Kugi, and Markus Aspelmeyer. Real-time optimal quantum control of mechanical motion at room temperature. *Nature*, 595(7867):373–377, July 2021.

[MZY22] Zhaozhao Ma, Ruiping Zhou, and Qingchao Yang. Recent advances in quasi-zero stiffness vibration isolation systems: An overview and future possibilities. *Machines*, 10(9), 2022.

[NCRI+24] Lukas Neumeier, Mario A. Ciampini, Oriol Romero-Isart, Markus Aspelmeyer, and Nikolai Kiesel. Fast quantum interference of a nanoparticle via optical potential control. *Proceedings of the National Academy of Sciences*, 121(4):e2306953121, 2024.

[NMTS21] Carles Navau, Stefan Minniberger, Michael Trupke, and Alvaro Sanchez. Levitation of superconducting microrings for quantum magnetomechanics. *Phys. Rev. B*, 103:174436, May 2021.

[PPCS+18] H Pino, J Prat-Camps, K Sinha, B Prasanna Venkatesh, and O Romero-Isart. On-chip quantum interference of a superconducting microsphere. *Quantum Science and Technology*, 3(2):025001, Jan 2018.

[RG15] Nima Riahi and Peter Gerstoft. The seismic traffic footprint: Tracking trains, aircraft, and cars seismically. *Geophysical Research Letters*, 42(8):2674–2681, 2015.

[RICN+12] O. Romero-Isart, L. Clemente, C. Navau, A. Sanchez, and J. I. Cirac. Quantum magnetomechanics with levitating superconducting microspheres. *Phys. Rev. Lett.*, 109:147205, 2012.

[RLRCC+24] M. Roda-Llordes, A. Riera-Campeny, D. Candoli, P. T. Grochowski, and O. Romero-Isart. Macroscopic quantum superpositions via dynamics in a wide double-well potential. *Phys. Rev. Lett.*, 132:023601, Jan 2024.

[RMZ+24] Massimiliano Rossi, Andrei Militaru, Nicola Carlon Zambon, Andreu Riera-Campeny, Oriol Romero-Isart, Martin Frimmer, and Lukas Novotny. Quantum delocalization of a levitated nanoparticle, 2024.

[SCH+24] Philip Schmidt, Remi Claessen, Gerard Higgins, Joachim Hofer, Jannek J. Hansen, Peter Asenbaum, Martin Zemlicka, Kevin Uhl, Reinhold Kleiner, Rudolf Gross, Hans Huebl, Michael Trupke, and Markus Aspelmeyer. Remote sensing of a levitated superconductor with a flux-tunable microwave cavity. *Phys. Rev. Appl.*, 22:014078, Jul 2024.

[SDR92] N J Simon, E S Drexler, and R P Reed. Properties of copper and copper alloys at cryogenic temperatures. final report. Technical report, National Inst. of Standards and Technology (MSEL), Boulder, CO (United States). Materials Reliability Div., 02 1992.

[SHK21] Benjamin A. Stickler, Klaus Hornberger, and M. S. Kim. Quantum rotations of nanoparticles. *Nature Reviews Physics*, 3(8):589–597, Aug 2021.

[TH77] W. Thompson and S. Hanrahan. Characteristics of a cryogenic extreme high-vacuum chamber. *Journal of Vacuum Science and Technology*, 14(1):643–645, 1977.

[Tin96] M. Tinkham. *Introduction to Superconductivity*. Dover Publications, 1996.

[UO30] G. E. Uhlenbeck and L. S. Ornstein. On the theory of the brownian motion. *Phys. Rev.*, 36:823–841, Sep 1930.

[vW16] Bob van Waarde. *The lead zeppelin : a force sensor without a handle*. Ph.D. thesis, Leiden University, 2016.

[Wei15] Steven Weinberg. *Lectures on Quantum Mechanics*. Cambridge University Press, 2 edition, 2015.

[WHPA21] Tobias Westphal, Hans Hepach, Jeremias Pfaff, and Markus Aspelmeyer. Measurement of gravitational coupling between millimetre-sized masses. *Nature*, 591(7849):225–228, March 2021.